THE UNIVERSITY OF CHICAGO

ANALYSIS OF SELF-CLEAVING RIBOZYME TRANSITON STATES

A DISSERTATION SUBMITTED TO

THE FACULTY OF THE DIVISION OF THE PHYSICAL SCIENCES

IN CANDIDACY FOR THE DEGREE OF

DOCTOR OF PHILOSOPHY

DEPARTMENT OF CHEMISTRY

BY

BENJAMIN WEISSMAN

CHICAGO, ILLINOIS

MARCH 2019

"Because it's there…Its existence is a challenge. The answer is instinctive, a part, I suppose, of man's desire to conquer the universe."

– George Mallory responding to the question, "Why do you want to climb Everest?"

Table of Contents

List of Figures v

List of Tables vii

List of Abbreviations viii

Acknowledgements ix

Chapter 1: Introduction 1

Chapter 2: Investigation of the VS Ribozyme Active Site
- 2.1 Introduction 9
- 2.2 Methods 14
- 2.3 Results 20
- 2.4 Discussion 41

Chapter 3: Characterization of the HDV Ribozyme Transition State
- 3.1 Introduction 45
- 3.2 Methods 52
- 3.3 Results 58
- 3.4 Discussion 63

Chapter 4: Conclusions 70

Appendix A: Investigation of Nucleophile Activation in HDV Ribozyme
- A.1 Introduction 75
- A.2 Methods 78
- A.3 Results 84
- A.4 Discussion 96

References 98

List of Figures

Figure 1.1 Simple schematic for 2′O-transphosphorylation 1

Figure 1.2 Logic of mutational analysis 4

Figure 1.3 More O'Ferrall-Jenks diagrams for nucleophile and leaving groups 7

Figure 2.1 Simplified schematic of the VS active site..... 10

Figure 2.2 VS ribozyme active site configures for various crystal structures 13

Figure 2.3 k_{obs} for cleavage of VS substrates by ribozyme variants under various ionic conditions depicted in Table 2.1 21

Figure 2.4 MD simulations of the VS active site with and without Mg^{2+} 26

Figure 2.5 3D-RISM calculations of metal ion binding in VS active site 27

Figure 2.6 MD simulations Mg^{2+} ion binding in the VS active site..... 30

Figure 2.7 pH-rate profiles of VS ribozymes with A756 mutations 35

Figure 2.8 pH-rate profiles of VS ribozymes with G638 mutations 36

Figure 2.9 Brønsted plots for VS ribozymes with A756 and G638 mutations 37

Figure 2.10 Reaction landscape for VS catalysis bases on QM simulations 40

Figure 2.11 Updated schematic of the VS active site..... 43

Figure 3.1 General scheme for 2′O-transphosphorylation..... 45

Figure 3.2 Schematic for the HDV active site 46

Figure 3.3 Reaction coordinate diagram for P–O bond cleavage..... 48

Figure 3.4 More O'Ferrall Jencks plot for 2′O-transphosphorylation 51

Figure 3.5 Kinetic isotope effects for hydroxide, RNase A and HDV measured by mass spectroscopy and remote label 60

Figure 3.6 pH-rate profile of hydroxide catalyzed cleavage 62

Figure 3.7 Pulse-Chase experiments for wild type and SII HDV substrates 62

Figure 3.8 Comparison of 2′O-transphosphorylation transition states 68

Figure A.1 Synthesis of propanediol phosphoramidites from corresponding diols. 84

Figure A.2 pH-rate profile for base-catalyzed solution cleavage of DNA propanediol substrates 87

Figure A.3 Proposed mechanism of cleavage by monoflouromethylpropanediol tethered DNA oligonucleotide under alkaline conditions 89

Figure A.4 pH-rate profile for base-catalyzed solution cleavage of DNA substrates 91

Figure A.5 K_m for ribozyme-substrate complex formation 91

Figure A.6 pH-rate profile for ribozyme catalyzed cleavage of tethered substrates 93

List of Tables

Table 1.1 Catalytic strategies for self-cleaving ribozymes 6

Table 2.1 k_{obs} for cleavage of VS substrates by ribozyme variants under various ionic conditions 23

Table 2.2 Fitted parameters of from pH-rate profiles in Figures 2.7 and 2.8 37

Table 3.1 Parameters for calculation of isotope effects through remote label 60

Table A.1 Mass of propanediol substrates by mass spectroscopy 85

Table A.2 Rates for uncatalyzed tether release under basic conditions 87

Table A.3 Fitted parameters of from pH-rate profiles in Figure A.6 93

Table A.4 Comparison cleavage rates for modified DNA/RNA ribonucleotide and tethered substrates in the presence of ribozyme or absence of ribozyme 95

List of Abbreviations

3cA	3-deazaadenine
3cP	3-deazapurine
3D-RISM	three-dimensional reference interaction site model
6sG	6-thio-guanine
7cA	7-deazaadeine
7cG	7-deazaguanine
8n7cA	8-aza-7-deazaadenine
8nA	8-azaadenine
8nG	8-azaguanine
ATP	adenosine triphosphate
C_f	forward commitment factor
DAP	diaminopurine
DMF	dimethylformamide
DNA	deoxyribonucleic acid
dPAGE	denaturing polyacrylamide gel electrophoresis
DTT	Dithiothreitol
EDTA	Ethylenediaminetetraacetic acid
GlmS	glucosamine-6-phosphate synthase
HDV	Hepatitis Delta Virus
HEPES	4-(2-hydroxyethyl)-1-piperazineethanesulfonic acid
HPLC	high-performance liquid chromatography
HpNPP	hydroxyl p-nitrophenyl phosphate
KIE	kinetic isotope effect
LFER	linear free energy relationship
LG	leaving group
MD	molecular dynamics
MES	2-(N-morpholino)ethanesulfonic acid
NBO	non-bridging oxygen
NMR	nuclear magnetic resonance
Nuc	Nucleophile
P*	5-aza-7-deazaguanine
ppm	parts per million
QM/MM	quantum mechanics
RNA	ribonucelic acid
SD	standard deviation
SEM	standard error of the mean
S_N2	bimolecualr nucleophilic substitution
TAPS	[tris(hydroxymethyl)methylamino]propanesulfonic acid
TDF	temperature independent factor
TEAA	triethylamine acetate
TIF	temperature dependent factor
VS	Varkud Satellite
WT	wild type

Acknowledgments

First, I'd like to thank my advisor Joe Piccirilli, for his guidance over the past several years. Obviously, Joe taught me quite a bit about self-cleaving RNA motifs, but far more importantly he taught be how to think about complex problems, the logic of scientific experimentation, and the nature of proof. He showed me a way to look at the world critically that I'll take with me into my life outside of science. Additionally, I'd like to thank my committee members, Phoebe Rice and Yamuna Krishnan for their thoughtful comments on my research and careful eyes in reviewing this document.

Other members of the Piccirilli lab played key roles in my development as a scientist. In particular, Saurja DasGupta, who also worked on VS ribozyme, shared his exhaustive knowledge of ribozyme literature and provided valuable feedback on my research. Deepak Koirala and Sandip Shelke offered great advice for navigating the ups and downs of graduate school always with a healthy dose of optimism. Nan-Sheng Li synthesized nearly all the molecules employed in my research, without him none of this work could have been completed. Last, but not least, my work built on the contributions of previous member of the Piccirilli group; in particular, the work of Subha Das and Selene Koo whose prior work on HDV ribozyme served as the intellectual basis for the work described here.

The work outlined here was done in close collaboration with researchers outside of University of Chicago. In particular, Abir Ganguly in the York laboratory and Rutgers has served as a great collaborator on the VS project and a wonderful colleague. Hsuan-Chun Lin measured KIEs for HDV ribozyme via mass spectroscopy in the Harris laboratory at university of Florida in support of the HDV project. Those measurements help bolster our confidence the remote label measurements obtained here and provided valuable momentum to that project.

Chapter 1: Introduction

The identification of RNA sequences capable of site-specific endonucleolytic cleavage (Prody et al. 1986) more than thirty years ago sparked intense investigation into the mechanism and evolutionary origins of these fascinating molecules. The discovery of the so-called hammerhead and hairpin ribozymes was closely followed by descriptions of other self-cleaving sequences including the Hepatitis Delta Virus (HDV) (Sharmeen et al. 1988), Varkud satellite(Saville and Collins 1990) and glucosamine-6-phosphate synthase (GlmS) (Winkler et al. 2004) ribozymes. After a significant lull, novel bioinformatic approaches revealed four new ribozyme classes in the past five years: Twister(Roth et al. 2014), Pistol, Hatchet, and Twister Sister (Weinberg et al. 2015). All of these molecules facilitate an internal transesterification reaction in which a 2′-hydroxyl acts as a nucleophile, attacking the adjacent 3′-phosphate and displacing the downstream 5′-hydroxyl leaving group to form a 2′-3′-cyclic phosphate (Figure 1.1). Each of the nine classes of ribozyme is defined by a distinct global fold and significant diversity exists between the classes.

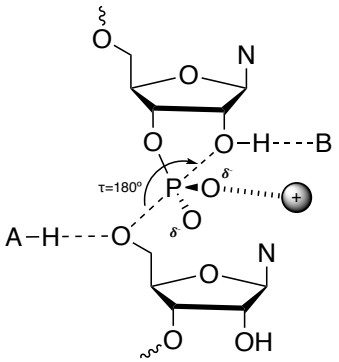

Figure 1.1 Simple schematic for 2′-transphosphorylation with depictions each of the four catalytic strategies. The reaction proceeds by nucleophilic attack of the 2′-hydroxyl on the adjacent downstream phosphate. Activation of the nucleophile by either proton transfer or Lewis base catalysis (shown here as "B") increases nucleophilicity. The negative charge on the O5′ leaving group is stabilized by proton transfer from A and and interactions with the non-bridging oxygens stabilizes the developing negative charge. Optimal geometry for the reaction occurs when tau approaches 180º.

Endonucleolytic ribozymes perform a number of biological functions including metabolite sensing and processing multimeric genome processing and and phosphoryl transfer chemistry is essential to genetic inheritance, metabolic pathways and cellular signaling (Knowles 1980, Westheimer 1987). Therefore, a deep understanding of the mechanism by which RNA and protein enzymes accelerate RNA cleavage is of critical importance. In order to understand the catalytic strategies employed by endonucleolytic ribozymes to facilitate transphosphorylation, I borrow a framework developed by Cochrane and Strobel (Cochrane et al. 2009) that expounds four main mechanistic strategies:

1. *Nucleophile activation*: 2′-hydroxyl groups are very bad nucleophiles. Thus, facilitation of the transphosphorylation requires transformation of 2′-hydroxyl groups in better nucleophiles, usually through proton transfer. This is often broadly referred to as "general base catalysis", but general base catalysis technically refers to a special case where proton transfer from the nucleophile occurs in the rate-limiting step of the reaction. Pre-equilibrium proton transfer (specific base catalysis) or Lewis base catalysis could also serve this purpose.
2. *Leaving group protonation*: In the uncatalyzed reaction, O5′ atom departs the scissile phosphate as a negatively charged alkoxide. However, general acid catalysis stabilizes the negative charge on the leaving group and enhances the rate of the reaction.
3. *Electrostatic stabilization*: Nucleophilic attack causes the scissile phosphate to take on phosphorane character which means that the bonds between the phosphorus and the non-bridging oxygens loses some double-bond character and the partial negative charge on the non-bridging oxygens increases. Electrostatic stabilization of that negative charge through interactions with metal ions or nucleobases can enhance reactivity.

4. *Active site organization*: Since transphosphorylation is an S_N2 reaction, it requires alignment of the 2′-hydroxyl, scissile phosphate and the 5′-hydroxyl leaving group. Ideally, the angle formed by these three atoms (τ) should approach 180º for optimal reactivity. Interactions that position the nucleobases on either side of the scissile phosphate, therefore, increase the occupancy of orientations with proper τ alignment and enhance reactivity.

In ribozymes, these four catalytic strategies are mediated predominantly by interactions involving metal ions and ribonucleotides. Thus, compared to protein enzymes, which are composed of 20 chemically distinct amino acids, ribozymes make do with comparatively little chemical diversity. A quick thought experiment reveals that limitations on the "catalytic space" for ribozyme catalysis: Assuming all self-cleaving ribozymes employ each of the first three catalytic strategies[1] outlined above, and that all are mediated by interactions involving one of the four nucleobases, a 2′-hydroxyl group, or a divalent metal ion, ribozyme active sites consist of three critical interactions each from a menu of six possibilities. Therefore, in a very crude sense, 729 (3^6) possible endonucleolytic active sites exist. Of course, this analysis ignores more subtle differences in nucleobase interactions. For instance, adenine can mediate general acid catalysis (strategy 2) either through N1 or N3 resulting in different pK_a for proton transfer and likely different transition states. Moreover, an active site in which a single guanine facilitates nucleophile activation and electrostatic stabilization (strategies 1 and 3) likely takes on different character than an active site where two guanine residues mediate these strategies independently. Clearly, the simplicity of this analysis ignores a great deal about the similarities and differences

[1]Active site organization requires multiple interactions working in concert to generate an orientation with τ~180º, so strategy is not amenable to this type of analysis.

between ribozyme active sites, but if reveals that the "catalytic space" available to endonucleolytic ribozymes is large but tractable[2].

The most straightforward experiment in enzymology is mutational analysis: mutate a single residue (or alter the ionic environment) and observe a change in catalysis (Figure 1.2 A). If the mutated residue is important for the function of the catalyst, then a change in reactivity is expected. These types of experiments, however, provide no information on the role of the residue under investigation – only on the importance of the residue. In order to infer function, one must make two perturbations to generate a mutational cycle (Figure 1.2 B). When mutations are functionally linked, their effect on catalysis will be different in the presence or absence of the other. Thus, mutational cycle analysis can reveal function (or at least functional linkage) in addition to importance.

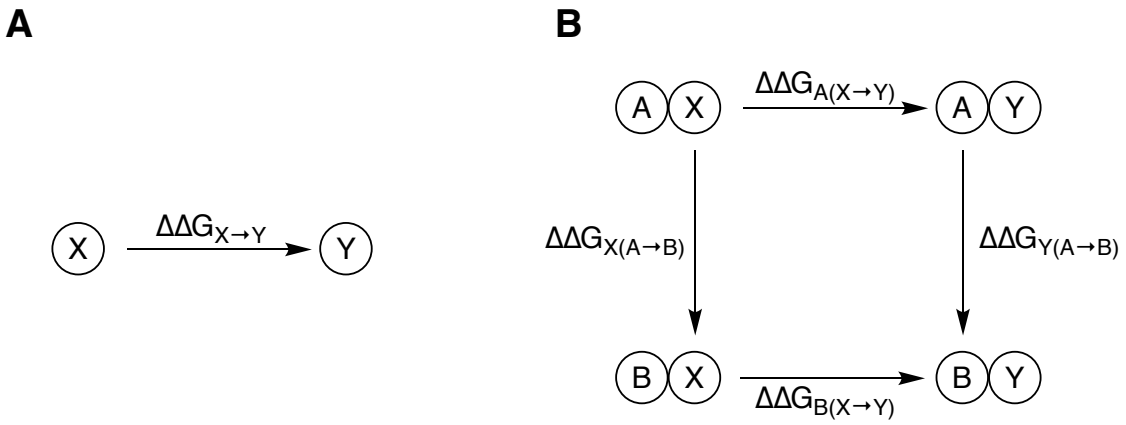

Figure 1.2 Logic of mutational analysis. For a single mutation (A) $\Delta\Delta G \neq 0$ reveals the importance of X for reactivity, but provides no information regarding function. For a double mutation cycle (B) $\Delta\Delta G_{A(X\rightarrow Y)} \neq \Delta\Delta G_{B(X\rightarrow Y)}$ and $\Delta\Delta G_{X(A\rightarrow B)} \neq \Delta\Delta G_{Y(A\rightarrow B)}$ reveals a functional linkage between A and X.

[2] Compare the less than 10^3 possible ribozyme actives sites with the more than 10^{10} active sites available to protein enzymes based on the same exercise.

In ribozymology, two classical problems illustrate the importance of mutational cycles to infer functional linkage. Phosphorothioate mutation (replacement of one or both non-bridging oxygens on a phosphate with sulfur) is a classic preliminary test for the importance of linking phosphates. Observation of a thio effect is taken as evidence for an interaction involving the substituted oxygen; however, this type of experiment provides no information on what the oxygen is doing. To infer a functional linkage between a non-bridging oxygen and another chemical group, one can observe the thio effect for sulfur substitution in the presence and absence of a mutation (or change in ionic conditions) that perturbs the suspected interaction partner. If the thio effect changes, the straightforward interpretation is that the alteration of the other group is responsible. In another example, generation of a pH-rate profile for a ribozyme reaction can provides on the sensitivity of the information to pH, but on its own, all this data demonstrates is that pH is important for catalysis. These data provide no information on the nature of that importance. However, observation that a particular mutation affects the dependence of rate on pH s provides suggestive evidence that catalysis depends on the protonation state of the mutated group.

The mechanistic enzymology of endonucleolytic ribozymes has been focused on identifying the mechanisms by which ribozymes engage the aforementioned catalytic strategies. Nearly three decades of functional data combined with high-resolution crystal structures (for seven of the nine ribozyme classes) have helped to identify these interactions and provide a basis for comparison between ribozyme active sites. Table 1.1 shows the chemical moieties involved in 2′-hydroxyl activation and 5′-hydroxyl stabilization in the ribozyme classes with published crystal structures. Strikingly, four ribozyme classes (VS, Hairpin, Pistol and Twister) use a guanine residue for nucleophile activation and adenine for leaving group protonation. The

remaining three classes (HDV, Hammerhead, and GlmS) use a hodgepodge of alternate chemical moieties for catalysis. The observation that many, but not all, ribozymes employ a similar set of residues for catalysis raises a question: what is special about guanine/adenine tandem and why do four of the ribozymes employ it for catalysis? An answer to these questions requires an understanding, not only of the catalytic interactions involved in ribozyme catalysis, but of the catalytic transition states for these reactions.

Ribozyme	**2′-hydroxyl activation**	**5′-hydroxyl stabilization**	**Reference(s)**
Hairpin	G8(N1)	A38(N1)	(Kath-Schorr et al. 2012)
VS	G638(N1)	A756(N1)	(Wilson et al. 2010, Wilson, McLeod, and Lilley 2007, Jaikaran et al. 2008)
Twister	G33(N1)	A1(N3)	(Wilson et al. 2016)
Pistol	G40(N1)	A32(N3)	(Ren et al. 2016, Neuner et al. 2017)
HDV	Mg^{2+}–OH	C76(N1)	(Das and Piccirilli 2005, Thaplyal et al. 2013)
Hammerhead	G8(O2')	G12(N1)	(Thomas and Perrin 2009, 2008)
GlmS	G40(N1)	GlcN6P	(Viladoms and Fedor 2012)

Table 1.1 Catalytic strategies for characterized self-cleaving ribozymes.

Since 2′-transphosphorylation reactions involve the alteration of four chemical bonds, the transition states for these reactions can be thought of as existing in a four-dimensional space with each bond as an axis. The space mapped by the axes for formation of the (O2′)–P and (O5′)–(H5′) bonds as well was the cleavage of (O5′)–P and (O2′)–(H2′) bonds, therefore, contains all the possible endonucleolytic ribozyme transition states. Visualization of this four-dimensional space is problematic, but the space can be divided into two More O'Ferrall–Jencks diagrams (Figure 1.3) – one for bonds to the leaving group and another for the nucleophile. Together, these plots map out the reaction landscape for 2′-transphosphorylation.

With this framework in mind, one might ask: Can ribozyme active sites shift the position of a transition state (and, by extension, the reaction pathway) from the uncatalyzed reaction? At a fundamental level, enzymes enhance the rate of chemical reactions by selectively stabilizing

chemical transition states, but it remains an open question (at least for endonucleolytic ribozymes) whether active sites evolve to stabilize particular transition states or if enzyme active sites are capable altering reaction pathways to create new transition states. The answer depends largely on the character of the energy landscape for the reaction. For reactions that have "coarse" energy landscapes with large differences in potential energy between relatively close – with respect to chemical structure – states, enzymes are unlikely to meaningfully alter reaction pathways and would be expected to evolutionarily converge toward active sites that support the transition states corresponding to energy minima. However, for reactions with "flat" energy landscapes characterized by relatively small potential energy differences between neighboring chemical states, enzyme catalysis can create new reaction pathways by stabilizing alternate chemical states. Of course, full characterization of an energy landscape for a chemical reaction is impossible (except *in silico*), but reaction landscapes can be probed through careful characterization of transition states under slightly altered conditions.

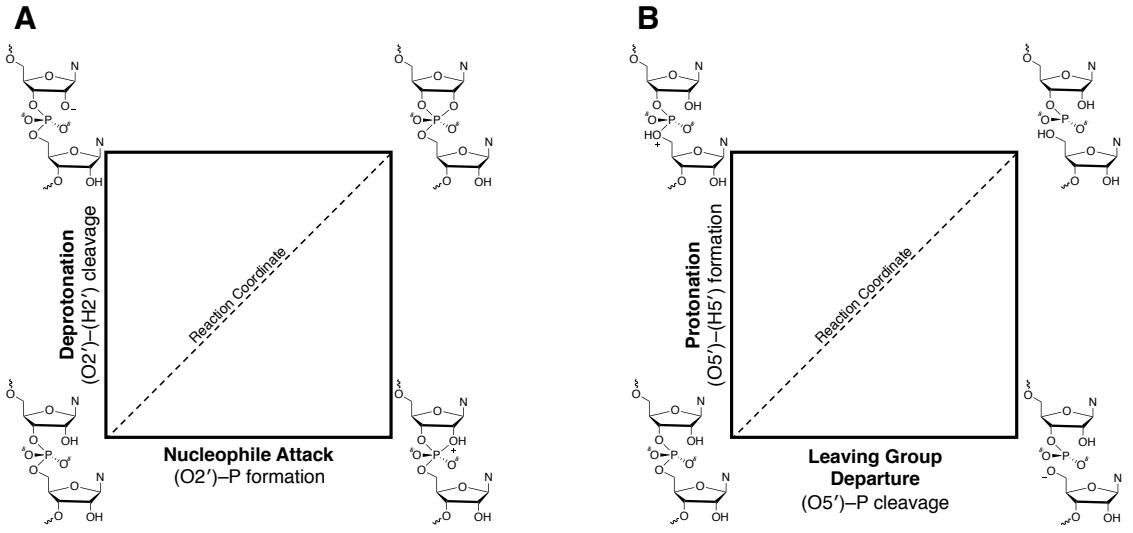

Figure 1.3 More O'Ferrall–Jencks diagrams from (A) nucleophile activation and attack and (B) leaving group protonation and departure. All 2′-transphosphorylation transition states can be characterized by their position on these two coordinates.

Either scenario entails interesting implications for comparative ribozymology. For instance, the observation that four out of the seven well-characterized ribozyme active sites contain a guanine/adenine tandem of catalytic nucleobases hints at evolutionary convergence toward an optimal active site consistent with a coarse energy landscape for ribonucleolytic cleavage. If true, however, that conclusion would raise questions about the ribozyme active sites that adopt alternate strategies (HDV, Hammerhead, and GlmS). Are these ribozymes capable following the same reaction pathway and stabilizing a structurally similar transition state? If not, what penalty do they incur for adopting alternate catalytic strategies? Alternately, ribonucleolytic cleavage could be characterized by a relatively flat energy landscape, which would help explain the diversity of active sites observed among the ribozyme classes, but would invite scrutiny into why several of the classes adopt superficially similar active sites. Understanding these problems would substantially advance the field of comparative ribozymology, but getting at the answers requires complex biophysical analysis.

In an effort to better understand relationships between endonucleolytic ribozymes, more broadly between RNA nucleases and protein nucleases, and even more broadly between catalyzed and uncatalyzed ribonucleolytic cleavage, my research over the past five years has focused on analysis of self-cleaving ribozyme transition states. In Chapter 2, I focus on catalysis by VS ribozyme with particular attention paid to the functional linkages that organize the active site and contribute to catalysis. In Chapter 3 and Appendix 1 of this thesis, I focus on catalysis by HDV ribozyme. Studies that employ kinetic isotope effects or subtly perturb the nucleophilicity of the 2′-hydroxyl provide insight into structure of the transition state and the relationship between HDV and alkaline catalysis. Last, I contrast the implied transition states in HDV and VS and offer perspectives on the future directions for the field.

Chapter 2: Investigation of the VS Ribozyme Active Site

2.1 Introduction

The Varkud satellite (VS) ribozyme, the largest of the nine (and counting) classes of endonucleolytic ribozymes (Cochrane and Strobel 2008, Jimenez, Polanco, and Luptak 2015, Lilley 2004), is found in the mitochondria of *Neurospora* where it facilitates processing of the linear multimers into circular monomers during rolling circle replication of the VS plasmid (Kennell et al. 1995, Saville and Collins 1990). The full-length, wild-type ribozyme consists of seven helical segments (helices I – VII) organized by three three-way junctions. The substrate helix (helix I), which can be separated from the rest of the ribozyme to form a *trans* construct, docks into the catalytic domain (helices II – VI) through a number of tertiary interactions that include a critical kissing-loop interaction (Rastogi et al. 1996, Zamel and Collins 2002).

Like all endonucleolytic ribozymes, VS catalyzes site-specific self-scission via nucleophilic attack of a 2'-hydroxyl on the adjacent phosphate to form a 2',3'-cyclic phosphate and a 5'-hydroxyl terminus (Seith et al. 2018) (Figure 1.1). A significant body of functional (Lafontaine et al. 2001, Lafontaine et al. 2002, Wilson, McLeod, and Lilley 2007, Jaikaran et al. 2008, Wilson et al. 2010, Smith and Collins 2007) and crystallographic (Suslov et al. 2015, DasGupta, Suslov, and Piccirilli 2017) data suggests that two critical nucleobases, A756 and G638, participate in catalysis, putatively acting as general acid and general base catalysts, respectively. VS ribozyme displays a bell-shaped rate dependence on pH consistent with two functional titrations with pK_a values of about 5.8 and 8.3 (Smith and Collins 2007). The pK_a rate-inhibiting titration exhibits sensitivity toward G638 mutations (Wilson, McLeod, and Lilley 2007, Jaikaran et al. 2008) consistent with proton transfer; however, these data cannot distinguish between general acid or general base catalysis due to kinetic equivalence (Bevilacqua

2003). Strong evidence for A756 as a putative general acid comes from investigations of substrates with 5'-bridging phosphorothioate modifications (Wilson et al. 2010). In the 5'-phosphorothioate background, the hyper-labile leaving group mitigates the need for activation of the leaving group, thus these substrates provide a basis for chemical rescue of inactive A756 mutants. In VS, the 5'-phosphorothioate mutation rescued an inactive A756G mutant ribozyme consistent with general acid catalysis. Although phosphorothioate rescue experiments have generally been viewed as the "gold standard" for evidence of general acid catalysis, it should be noted that they report only on the functional linkage between the mutated nucleoside and the O5' atom under investigation. These experiments do not provide evidence for proton transfer (a requirement of general acid catalysis), nor do they provide atomic resolution for catalytic interactions (i.e. they cannot distinguish whether the interaction between A756 and the 5'O leaving group is mediated by N1 or N6).

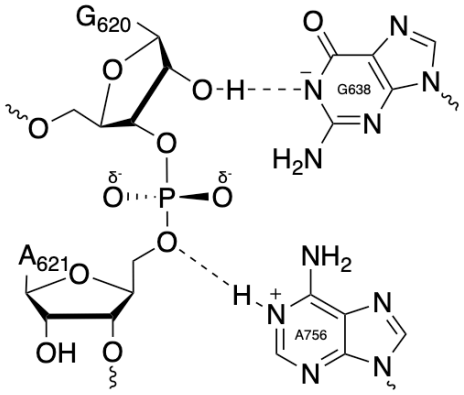

Figure 2.1 Simplified schematic of the VS active site. The putative general acid, A756, stabilizes the 5'O-leaving group during the reaction while the putative general base, G638, activates the nucleophile. The view of the VS active site is only inclusive of functional data collected before the publication of crystallographic data.

A variety of spectroscopic data (Campbell and Legault 2005, Campbell et al. 2006, Bonneau and Legault 2014b, a, Dagenais et al. 2017) strongly suggests that VS activity depends on multiple localized divalent ions. VS cleavage typically requires Mg^{2+} ions for activity, except in very high concentrations of monovalent ions (Murray et al. 1998). The ribozyme is not active in cobalt hexammine alone, but in sub-millimolar concentrations of Mg^{2+}, cobalt hexammine accelerates catalysis (Maguire and Collins 2001). The Mg^{2+} ion dependence on ribozyme folding, inferred from protection of reaction with hydroxy radicals, was estimated to be an order of magnitude lower concentration than that required for catalysis (Tzokov, Murray, and Grasby 2002). Additionally, a number of phosphates in the substrate helix (helix I) are sensitive to phosphorothioate mutation including the scissile phosphate, G620[3], and the phosphodiester immediately downstream of A621 (N_{+1} phosphate)(Sood, Beattie, and Collins 1998, Kovacheva et al. 2004), The A621 phosphodiester was found to partially rescue in the presence manganese; however the scissile phosphate did not rescue. Additionally, a A621 R_p thio substrate was found to attenuate the reverse reaction (ligation). This result combined with the metal rescue data, hints at the presence of a metal ion near the active site coordinated through the A621 *pro*R_p non-bridging oxygen (Zamel and Collins 2002). Taken together these studies indicate that Mg^{2+} ions provide structural stability, and may also contribute towards catalysis.

Until recently, no high-resolution structural data existed to guide mechanistic investigations into VS ribozyme catalysis. However, our laboratory reported the first pre-catalytic crystal structures of the VS ribozyme. These first structures contained a G638A mutation (PDB ID 4R4V) and an A756G (PDB ID 4R4P) mutation, to prevent self-cleavage during crystallization. A C634G mutation was also introduced for the activation and binding of

[3] In this text, phosphates are referred to by the base directly *upstream*. Thus, the G620 phosphate refers to the phosphate between G620 and A621 attached to the 3'O of the G620.

the substrate helix to the catalytic domain (Suslov et al. 2015). A follow-up study revealed the structure of the ribozyme with a substrate with the G638A mutation (PDB ID 5V3I) but without the C634G mutation, demonstrating that the substrate helix can remodel itself naturally during the course of binding (DasGupta, Suslov, and Piccirilli 2017). The crystal structures confirmed the approximate secondary structure of the ribozyme, revealing seven helical segments organized by three critical three-way junctions. The structures further revealed a 'domain-swapped dimer' organization, where the substrate helix of one protomer docks into the catalytic domain of another. This mode of association is consistent with biochemical results by the Collins and Lilley labs (Collins, DeAbreu, and Beattie 1997, Beattie and Collins 1997, Jones, Ryder, and Strobel 2001, Ouellet, Byrne, and Lilley 2009). Although the crystallographic data was in broad agreement with prior structural investigations, it is worth noting that these structures were obtained in the presence of 2M ammonium ion, which could preclude the binding of divalent metal ions or alter subtly alter the conformation of the active site.

Unfortunately, the active sites as revealed by these structures are not fully poised for catalysis, possibly resulting from mutations to the catalytic nucleobases. For example, although the crystal structures reveal that the G638 and A756 nucleobases are positioned in the active site in accordance to their putative roles of general base and acid, they reside just beyond hydrogen bonding distance to the nucleophile, G620(O2'), and the leaving group, A621(O5'), respectively. Additionally, the dihedral angle (τ) formed between the O2' oxygen, phosphorus atom of the scissile phosphate, and O5' oxygen in the structures ranges from 97-129°, which falls short of the ideal in-line geometry ($\tau = 180°$) required for S_N2 attack of the nucleophile. Prior functional work provided circumstantial evidence for the importance of the exocyclic amino groups on the catalytic nucleobases (Wilson, McLeod, and Lilley 2007, Jaikaran et al. 2008); however,

crystallographic data does not help to clarify their role in catalysis. In the 4R4P structure, the G638 exocyclic amine is within interacting distance to both non-bridging oxygen atoms of the scissile phosphate, while in the 4R4V and 5V3I structures, it is positioned to interact with the *proR*$_p$ non-bridging oxygen alone. A756 exocyclic amine is positioned to interact with the *proR*$_p$ non-bridging oxygen in 4R4P structure, but that interaction is absent in the other two structures. Thus, the precise roles of the exocyclic amines of the catalytic nucleobases (if they exist) remain unclear.

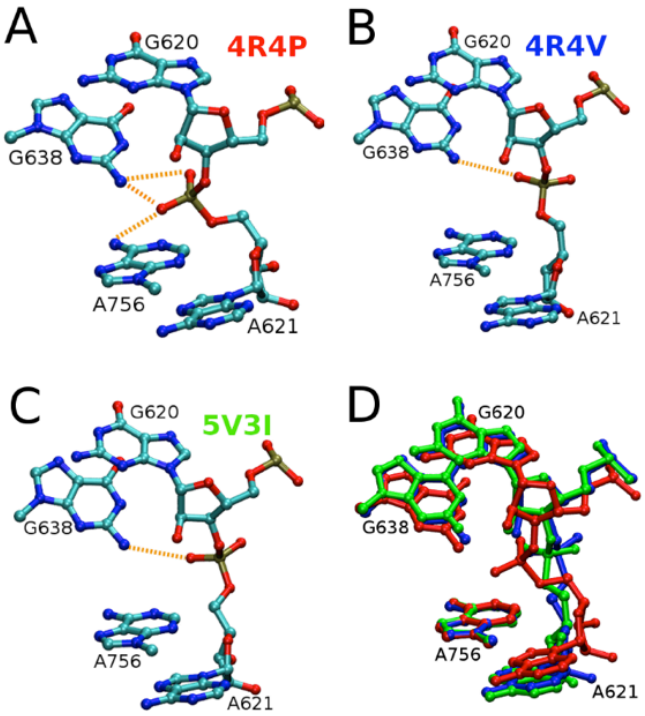

Figure 2.2 VS ribozyme active site configurations in the (A) 4R4P, (B) 4R4V, and (C) 5V3I crystal structures with (D) a superposition of the three different structures (4R4P – red, 4R4V – green, 5V3I – blue). Potential interactions between catalytic nucleobases and the scissile phosphate, nucleophile or leaving group are depicted with dotted lines. All structures have the mutated both catalytic nucleobases back to wild type *in silico*.

The work presented here, executed in close collaboration with the York group, focuses on identifying the catalytic interactions that organize the VS active site with special attention paid to interactions that organize the catalytic nucleobases, G638 and A756, and position the scissile and downstream phosphates. Additionally, we employed Brønsted analysis to investigate the role and extent of proton transfer, to and from the catalytic nucleobases during catalysis. Computational work from the York group helped to model actives sites informed by experimental to provide new, testable in support of these experiments helped to the mechanistic models inferred from the functional data.

2.2 Methods

RNA oligonucleotides and constructs

The VS enzyme strand was prepared by ligation of two RNA oligomers: one generated from solid-phase synthesis and the other by T7 transcription. The 115-nt 5' fragment (sequence: 5'- GGC GGU AGU AAG CAG GGA ACU CAC CUC CAA UUU CAG UAC UGA AAU UGU CGU AGC AGU UGA CUA CUG UUA UGU GAU UGG UAG AGG CUA AGU GAC GGU AUU GGC GUA AGU CAG UAU U) was generated by T7 transcription under standard conditions from a double-stranded DNA template, which was prepared as follows. A pUC19 plasmid containing 3' ligation fragment, was transformed into competent DH5α *Escherichia coli* cells and amplified, and the sequence was confirmed by sequencing, (The University of Chicago Core Facility). The plasmid was digested by EarI (New England Biolabs) to generate a double stranded DNA template that contains the T7 promotor sequence and a blunt end at the 3'-end of the ribozyme sequence. Following transcription, transcripts were purified first by phenol-chloroform-isoamyl alcohol extraction then by 6% denaturing polyacrylamide gel

electrophoresis (dPAGE). The transcripts were visualized under UV light, excised from the gel and eluted overnight in TEN buffer (10mM Tris pH = 8, 1mM EDTA, 300mM NaCl), then concentrated on centrifugal filter units for use. The 30-nt 3' ligation fragments (5'- GCA GAC CAG CAC AAG CCC GCU UGC GAG AAU – where the underlined A corresponds to A756) were synthesized in-house by solid-phase synthesis on a 1-μmol scale using an Expedite Nucleic Acid Synthesis System (8900) by following standard RNA synthesis protocols. The oligonucleotides were released from solid support with 3:1 NH_4OH/EtOH at 55 °C for 8 h, desilylated with 300 μL 6:3:4 N-methylpyrrolidinone/triethylamine/triethylamine-3HF at 65 °C for 2 h and precipitated by n-BuOH. The oligomers were further purified by dPAGE, collected in pure water and stored at −80 °C until further use.

The 3' ligation fragment was 5′-end phosphorylated with T4 polynucleotide kinase (New England Biolabs, NEB) in the presence of excess ATP at 37 °C for about 1 h followed by heat inactivation of the enzyme at 60 °C for 20 min. For the ligation reaction, 3' and 5' ligation fragments (1.5:1 molar ratio) were incubated in the presence of annealing buffer (20mM Tris pH = 7.5, 200nM NaCl, 0.2mM EDTA) at 90ºC for 2 minutes and slowly cooled to 10º over 1.5 hours. After annealing, T4 RNA ligase buffer (50 mM Tris pH 7.5, 2 mM $MgCl_2$, 1 mM DTT, 400 μM ATP) and T4 RNA ligase 2 (NEB) were added, and the resulting reaction mixture was incubated at 16ºC for 18 to 24 hours. Ligation reaction mixtures were purified by 10% dPAGE as described above and concentrations for pure oligos were determined using Nanodrop (Thermo Scientific).

The 24-nt VS substrates (5'- GCG CG*A AGG GCG UCG UCG GCC CGA, where the underlined G denotes G623 and the asterisk denotes the scissile phosphate, G620) strands were synthesized by solid- phase synthesis following the same procedures for described above.

Substrates containing phosphorothioate mutations were further separated by 4.6 x 250mm C18 reversed-phase high-performance liquid chromatography (HPLC) through an AcclaimTM 120 4.6 x 250mm C18 column (Dionex) with a 2795 Separations module (Waters). After a 10 minutes column equilibration step, a linear gradient from 9 to 10.6% acetonitrile over 35 minutes in a constant background of 0.1 M TEAA. Typically, this procedure resulted in clean separation of diastereomers with elution times around 15 and 19 minutes after the initiation of the gradient. The identities of the stereoisomers were identified by digestion with snake venom phosphodiesterase and nuclease P1 revealing that the first peak corresponded to S_p thio isomer while the second peak corresponded to the R_p thio isomer. Following HPLC purification, separated diastereomers were dried overnight under vacuum, resuspended in 300uL ddH_2O, ethanol precipitated, collected in pure water and stored at -80 °C until further use. Substrate strands were all 5′-end radiolabeled with T4 polynucleotide kinase (New England BioLabs) with [γ-^{32}P]ATP (PerkinElmer) prior to their use is kinetic reactions.

Ribozyme kinetic assays and data analysis

"Standard" conditions for ribozyme kinetic reactions are as follows: ribozyme RNA was incubated in water at 70º for 2 minutes to denature and allowed to renature at room temperature for 10 minutes in the presence of reaction buffer (25mM TAPS, 25mM HEPES, 10mM $MgCl_2$, 25mM KCl, 2mM spermidine, pH = 8). The reaction was then initiated by the addition of a trace amount of radiolabeled substrate RNA to a final concentration of 500nM ribozyme RNA (control reactions with four-fold higher ribozyme concentrations show a concentration of 500nM ribozyme to be near saturating) in a volume of 10μL. For pH dependence, appropriately pH-adjusted buffers containing either MES and HEPES (pH 5.5-8) or TAPS and HEPES (pH 7.5-

9.5) were used. Aliquots of the reaction mixture were taken at appropriate time points and quenched in stop solution (97% formamide, 15mM EDTA, 0.1% w/v bromophenol blue and xylene cyanol) and rapidly chilled on dry ice. Cleavage products were separated from uncleaved substrate on a denaturing 20% polyacrylamide/7M urea gel and quantified using a Typhoon PhosphorImager with ImageQuant software (Molecular Dynamics).

Data for cleavage reactions were fit in KaleidaGraph (Synergy Software) to equation 1 where *f* is the fraction cleaved, A is the amplitude or endpoint of the reaction (typically ~70% for HDV cleavage reactions), k_{obs} is the observed rate constant and *t* is the time.

$$f = A(1 - e^{-k_{obs}t}) \quad (1)$$

pH rate profiles were fit to a model for double ionization (equation 2) assuming a requirement for one protonated and one deprotonated group, where pK_{a1} corresponds to the rate stimulating titration, pK_{a2} corresponding to the rate-inhibiting titration and k_{cat} is the intrinsic rate constant or the reaction. Both pK_as and k_{cat} were fitted for pH rate profiles of the wild type ribozyme and ribozymes with A756 analogs, but pK_{a1} was fixed at 5.8 for fitting of G analog pH rate profiles.

$$k_{obs} = \frac{k_{cat}}{1 + 10^{pH - pK_{a1}} + 10^{pK_{a2} - pH} + 10^{pK_{a2} - pK_{a1}}} \quad (2)$$

The pH dependence for cleavage of the G638P* substrate was fit to the model for a single ionization in equation 3.

$$k_{obs} = \frac{k_{cat}}{10^{pH - pK_{a1}}} \quad (3)$$

Assuming that VS ribozyme reacts through a one-channel mechanism that depended on protonated A756 and deprotonated G638 residues, the intrinsic rate constant for cleavage can be

modeled by equation 4 where α and beta are the Brønsted coefficients for A756 and G638, respectively, and C is a constant for the reaction.

$$k_{cat} = \beta(pK_{a,G638}) - \alpha(pK_{a,A756}) + C \quad (4)$$

The Brønsted coefficients describe the extent of proton transfer in the transition state with possible values between 0 and 1. At one extreme, a value of zero for either coefficient would signify no proton transfer from the corresponding nucleobase and alteration of that nucleobase should have no impact on k_{cat}. At the other extreme, a value of one would signify complete proton transfer in the transition state. To determine the Brønsted coefficients for G638 and A756 in VS catalysis, we plotted the k_{cat} and pK_a inferred from the pH-rate dependence profiles described above and fit the resulting data linearly in KaleidaGraph (Synergy Software)

Thio effects and mutational and metal-ion rescue

The effect of substituting a sulfur at a non-bridging position of a phosphate is referred to as a thio effect (equation 5) where k_O is the rate constant for cleavage of the unsubstituted substrate and k_S is the rate constant for cleavage of the thio substrate.

$$\text{Thio effect} = \frac{k_O}{k_S} \quad (5)$$

When thio substitution reduces the observed rate constant for cleavage, the thio effect is larger than one and referred normal. For reactions where thio substation increases the observed rate constant, the thio effect will be less than one and referred as inverse.

To test whether thio effects arise from a loss of interaction with a specific chemical group, we observed thio effects in the presence and absence of that group. For instance, to test whether any of the observed thio effects arise from a loss of interaction with G638(N2), we test thio effects in the context of wild type and G638I substrates that lacked G638(N2). The

mutational rescue can be quantified in equation 6 where numerator is the thio effect in the wild type background and the denominator is the thio effect in the mutated background.

$$\text{Mutational Rescue} = \frac{\left(\frac{k_O}{k_s}\right)^{WT}}{\left(\frac{k_O}{k_s}\right)^{Mut}} \quad (6)$$

A mutational rescue of one indicates that the mutation has no impact on the thio effect, but when the a thio effect is reduced in the mutant background the mutational rescue will be larger than one indicative of a functional linkage between the mutation and the thio substitution.

If thio effects arise due to a loss of an interaction with a divalent metal ion, then addition of a thiophilic metal ion should "rescue" the lost interaction and ameliorate the thio effect (cite). Thus, we observed thio effect under standard conditions (10mM $MgCl_2$) and in the presence of a thiophilic metal ion (10mM $MgCl_2$ and 20μM $CdCl_2$). Metal ion rescue effect can be quantified following equation 7 where the numerator if the thio effect under standard conditions and the denominator is the thio effect in the presence of thiophilic ions.

$$\text{Metal ion Rescue} = \frac{\left(\frac{k_O}{k_s}\right)^{Mg^{2+}}}{\left(\frac{k_O}{k_s}\right)^{Cd^{2+}}} \quad (7)$$

A value greater one will be observed when the thio effect is reduced (or inverted) in the presence of thiophilic metal ions, thereby suggesting an interaction between the thio-substituted atom and the thiophilic ion. We conducted metal ion rescue under the (10mM $MgCl_2$ and 20uM $CdCl_2$) at

that concentration of $CdCl_2$ has essentially no impact on the rate of unsubstituted substrates, but fully stimulates thio substituted substrates.

2.3 Results

In an effort to better understand the catalytic interactions that organize the VS active site, we tested the effect of sulfur substitution at the non-bridging positions of the scissile phosphate. Earlier data demonstrated the deleterious effect of phosphorothioate substitution at the scissile phosphate; however, interpretation of these data are complicated by the fact that one study employed a mixture of diastereomers (Kovacheva et al. 2004) and another observed the effect of thio substitution on the reverse reaction (Zamel and Collins 2002). In this study, the R_p and S_p thio diastereomers were synthesized as a diastereomeric mixture, separated by HPLC and identified by selective endonuclease digestion (see methods). The results from the phosphorothioate experiments are summarized in Table 2.1 and Figure 2.3. Under standard conditions (25mM TAPS, 25mM HEPES, 10mM $MgCl_2$, 25mM KCl, 2mM spermidine, pH = 8), the wild type ribozyme cleaved the unmodified substrate with $k_{obs} = 0.32\ min^{-1}$. In contrast, the G620 R_p and S_p thio substrates cleaved with rates below the limit of detection, which correspond to thio effects of at least 3000-fold and suggest critical catalytic interactions involving both non-bridging oxygens.

Inspection of the crystal structures shows that the exocyclic amines of G638 and A756 reside spatially close to the non-bridging oxygens of the scissile phosphate (Suslov et al. 2015, DasGupta, Suslov, and Piccirilli 2017), and mutational studies of these nucleobases have hinted at the importance of their exocyclic amines(Wilson, McLeod, and Lilley 2007, Jaikaran et al. 2008). However, the conclusions drawn in these studies were complicated by the fact that the

mutations made to remove the exocyclic amines at the 638 and 756 positions, alter the pK_as of these residues, which consequently could affect their role in proton transfer during the cleavage reaction. To identify potential interactions of the G638 and A756 exocyclic amines to the non-bridging positions, we observed cleavage for ribozymes with the G638 mutated to inosine (G638I), A756 mutated to 3-deazapurine (A756(3cP)), or both (referred to here as "double mutant") in oxo (wild-type) and phosphorothioate backgrounds (Table 2.1 and Figure 2.3A).

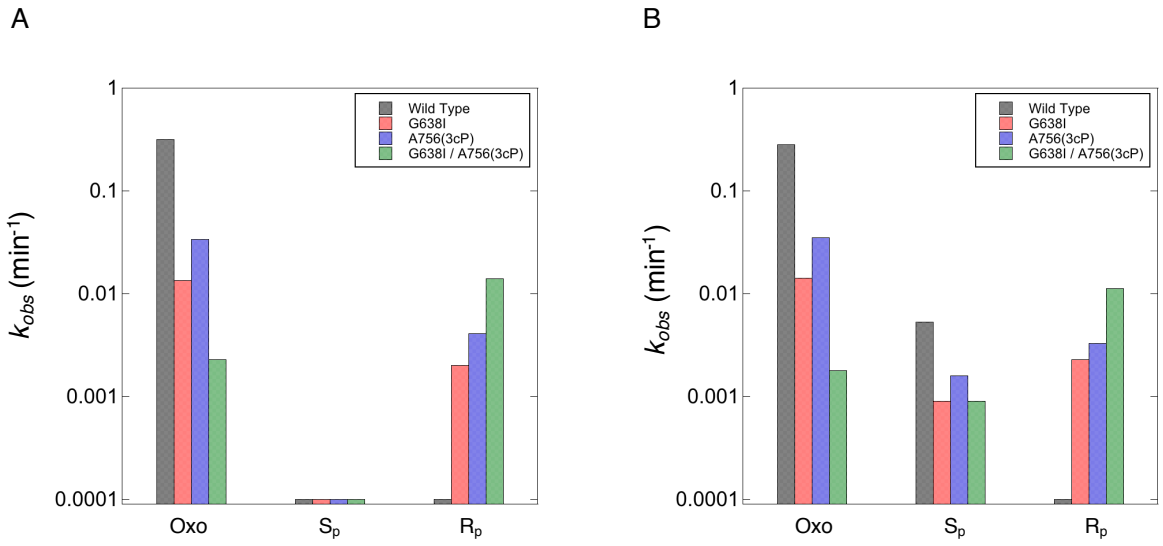

Figure 2.3 k_{obs} for cleavage of VS substrates by ribozyme variants under various ionic conditions depicted in Table 2.1. Panel (A) shows cleavage rates in 10mM $MgCl_2$ and (B) shows cleavage in 10mM $MgCl_2$ and 20μM $CdCl_2$. The wild type ribozyme is represented by grey bars, the G638I is red, A756(3cP) is blue and G638I/A756(3cP) (double mutant) is green.

In an oxo background, the G638I ribozyme variant cleaves with a rate of 0.014 min^{-1} corresponding to 23-fold rate reduction compared to WT consistent with previous data. Like the WT ribozyme, the G638I mutant cleaves the S_P thio substrate with rates that are lower than the limit of detection. However, the G638I ribozyme cleaves the R_P thio substrate with a rate of 0.0020 min^{-1} corresponding to at least a 20-fold rate enhancement compared to the cleavage of the same substrate by the wild type ribozyme indicative of a mutational rescue of about 450. The

A756(3cP) ribozyme cleaves the unmodified substrate with a rate of 0.034 min^{-1} corresponding to a 9.4-fold rate reduction compared to WT. Again, like the WT ribozyme, the A756(3cP) variant cleaves the S_P thio substrate slower than the limit of detection, but cleaves the R_P thio substrate with a rate of 0.0041 min^{-1} corresponding to a 41-fold rate enhancement over WT and a mutational rescue of about 380. The double mutant ribozyme with both the G638I and A756(3cP) mutations cleaves a phosphate substrate with a rate of 0.0023 min^{-1} corresponding to a 140-fold reduction suggesting that the effects from the G638I and A756(3cP) mutations are approximately additive (a 215-fold rate reduction would be expected for independent effects). Interestingly, the double mutant cleaves the R_P thio substrate with a rate of 0.014 min^{-1} corresponding to an inverse thio effect of 6 and a mutational rescue of nearly 20,000 (Table 2.1 and Figure 2.3A).

The inverse thio effect is unexpected but not without precedent. A similar effect was observed in the GlmS apo-ribozyme where, in the absence of cofactor, the N_{-1} 2'-hydroxyl engaged in an unproductive interaction with *proR*$_p$ non-bridging oxygen, which was eliminated in the R_P thio background (Bingaman et al. 2017). A similar mechanism could explain inverse thio effect observed here; in the absence G638(N2) and A756(N6) the *proR*$_p$ non-bridging oxygen engages the 2'-hydroxyl in an unproductive interaction that prevents the reaction center from achieving an in-line conformation. This unproductive interaction is disrupted in the R_P thio substrate resulting a modest (6-fold) rate enhancement. Therefore, these data strongly suggest that the active site is organized by interactions between G638(N2), A756(N6) and the *proR*$_p$ non-bridging oxygen and the disruption of either or both of these interactions substantially reduces the rate of cleavage

variant	ionic conditions	substrate	k_{obs} (min^{-1})	k_o/k_s	metal ion rescue	mutational rescue
Wild Type	10mM Mg^{2+}	oxo	0.32 ± 0.01			
		G620 S_p	0.0001 ± n.a.	3,153 ± n.a.		
		G620 R_p	0.0001 ± n.a.	3,153 ± n.a.		
		A621 S_p	0.0294 ± 0.0008	11 ± n.a.		
		A621 R_p	0.0001 ± n.a.	3,153 ± n.a.		
	10mM Mg^{2+} and 20μM Cd^{2+}	oxo	0.283 ± 0.005			
		G620 S_p	0.0053 ± 0.0001	54 ± 1	59 ± n.a.	
		G620 R_p	0.0001 ± 0.00002	2,111 ± 300	1.5 ± n.a.	
		A621 S_p	0.0328 ± 0.003	8.6 ± 0.9	1.2 ± n.a.	
		A621 R_p	0.0190 ± 0.007	15 ± 5	212 ± n.a.	
G638I	10mM Mg^{2+}	oxo	0.0135 ± 0.0006			
		G620 S_p	0.0001 ± n.a.	135 ± 8		23 ± n.a.
		G620 R_p	0.0020 ± 0.0001	7 ± n.a.		456 ± n.a.
	10mM Mg^{2+} and 20μM Cd^{2+}	oxo	0.0141 ± 0.0005			
		G620 S_p	0.0009 ± 0.0001	15 ± 2	9.1 ± 1.3	3.6 ± 0.5
		G620 R_p	0.0023 ± 0.0001	6 ± 0.4	1.1 ± n.a.	348 ± 55
A756(3cP)	10mM Mg^{2+}	oxo	0.0336 ± 0.0002			
		G620 S_p	0.0001 ± n.a.	336 ± 20		9.4 ± n.a.
		G620 R_p	0.0041 ± 0.0001	8 ± n.a.		385 ± n.a.
	10mM Mg^{2+} and 20μM Cd^{2+}	oxo	0.035 ± 0.002			
		G620 S_p	0.0016 ± 0.0001	22 ± 2	15 ± 1	2.4 ± 0.2
		G620 R_p	0.0033 ± 0.0001	11 ± 1	0.77 ± n.a.	200 ± 31
G638I and A756(3cP)	10mM Mg^{2+}	oxo	0.0023 ± 0.0004			
		G620 S_p	0.0001 ± n.a.	23 ± 2		138 ± n.a.
		G620 R_p	0.0140 ± 0.0006	0.16 ± n.a.		19,366 ± n.a.
	10mM Mg^{2+} and 20μM Cd^{2+}	oxo	0.0018 ± 0.0001			
		G620 S_p	0.0009 ± 0.0005	2.0 ± 1.1	12 ± 7	27 ± 15
		G620 R_p	0.011 ± 0.003	0.16 ± 0.04	1.0 ± n.a.	13,170 ± 3,639

Table 2.1 k_{obs} for cleavage of VS substrates by ribozyme variants under various ionic conditions. The error of k_{obs} measurements is the standard deviation of three or more independent measurements and errors for thio effect, metal ion rescue, and mutational rescue are the propagated errors of relative errors. Reactions that proceed with slower than the limit of detection (<5% cleavage after 24 hours) have been assigned a rate of 10^{-4} min^{-1} and cannot be assigned an error ("n.a."). Propagated errors based on these measurements are also "n.a."

.

In an effort to unify the VS ribozyme crystal structures with the existing body of solution data, the York laboratory launched molecular dynamic (MD) simulations to see if molecular motions from the active site configurations observed in the crystal structures could plausibly generate active sites consistent with a consensus picture of VS catalysis. We arbitrarily defined "active states" as conformations in which G638 is positioned for 2'O-nucleophile activation, A756 is positioned for 5'O-leaving group stabilization, and the τ angle approaches 180º consistent with S_N2 attack. This definition makes assumptions about the roles of the catalytic

nucleobases, but is consistent with the consensus view of the VS mechanism as well as subsequent experimental and computational data (see below). To that end, they observed MD simulations of the WT ribozyme, using the different crystal structures as departure points (Suslov et al. 2015, DasGupta, Suslov, and Piccirilli 2017) (Figure 2.4). Results from these simulations are summarized in Figure 2.4A-C. Figure 2.4A depicts the important active site interactions along the various MD trajectories in the form of interaction maps. These interaction maps are meant to provide qualitative insight into the active site conformation during the simulations. Details on how these maps are generated are provided in the figure caption; briefly, given a threshold criterion, a vertical bar at a given time frame in these maps indicates the presence of an interaction, while the intensity of the color on the bar reflects the strength of the interaction, that is, the magnitude of the interaction with respect to the chosen threshold value. According to Figure 2.4A, the simulations based on the different crystal structures paint a similar picture of the ribozyme active site dynamics – one that does not exhibit the essential catalytic strategies. During these simulations, the phosphate reaction center is seldom in in-line conformation (blue), suggesting inadequate alignment for attack. Among interactions that could potentially stabilize the developing negative charge on the non-bridging oxygens (green), the A756 exocyclic amine engages in a steady interaction with the *pro*R_p non-bridging oxygen, while G638 is mobile, its exocyclic amine forming transient interactions to both non-bridging oxygens, and a Na^+ ion coordinates to the *pro*S_p non-bridging oxygen. G638(N1) rarely interacts with the 2'O-nucleophile group (red), and thus is rarely in a position to partake in general base catalysis. A756(N1) interacts with the 5'O-leaving group (purple), albeit not consistently, consistent with its participation in general acid catalysis. The low color intensity in all these maps, reflects conformations with corresponding interactions sporadically populated.

Since A756 remains properly positioned for 5'O-leaving group stabilization throughout the trajectories, we evaluated conformations of the phosphate reaction center with respect in-line alignment (τ near 180º) and 2'O-nucleophile activation (G638(N1) positioned near the 2'O-nucleophile). The results of this analysis are presented in Figure 2.4C, wherein data from all simulations are combined and projected in the 2D space of the distance between O2' and the phosphorus atom (x-axis) and τ angle (y-axis). Configurations are classified based on whether they exhibit a τ greater than 140º and G638(N1)–O2' distance less than 3.5Å. As evident from Figure 2.4C, most simulations (40%) sample conformations where neither condition is met. Of the remaining simulations, a majority of the configurations (53%) meet one but not both of the conditions for catalysis. Only a small fraction of all configurations (7%) exhibit both in-line alignment and nucleophilic activation (Figure 2.4B). Thus, the active site ensemble that emerges from these simulations does not appear to reflect the active state of the ribozyme.

No divalent metal ions were observed in the crystal structures of VS ribozyme crystal structures, possibly because the structures were obtained in the presence of 2M ammonium ion. Moreover, 3.1Å diffraction data can provide ambiguous atomic resolution, making identification of a bound Mg^{2+} ion difficult. However, as mentioned previously, a number of prior studies strongly suggest that VS activity depends on multiple localized divalent ions. Careful analysis of the MD trajectories revealed two sites in the active site where Na^{+} ions tend to bind (Figure 2.5A). Site A is at the *pro*S_p non-bridging oxygen of the scissile phosphate, and site B is between the 2'O nucleophile and the *pro*R_p non-bridging oxygen of the scissile phosphate. To identify probable Mg^{2+} binding sites, we carried out 3D-RISM calculations on the different crystal structures as well as configurations obtained from simulations. Results from the 3D-RISM calculations suggest high probability of a Mg^{2+} ion binding at site A in the active site (Figure

2.5B). Mg^{2+} ion at this position is consistent with the large thio effect observed at the S_p non-bridging position described above.

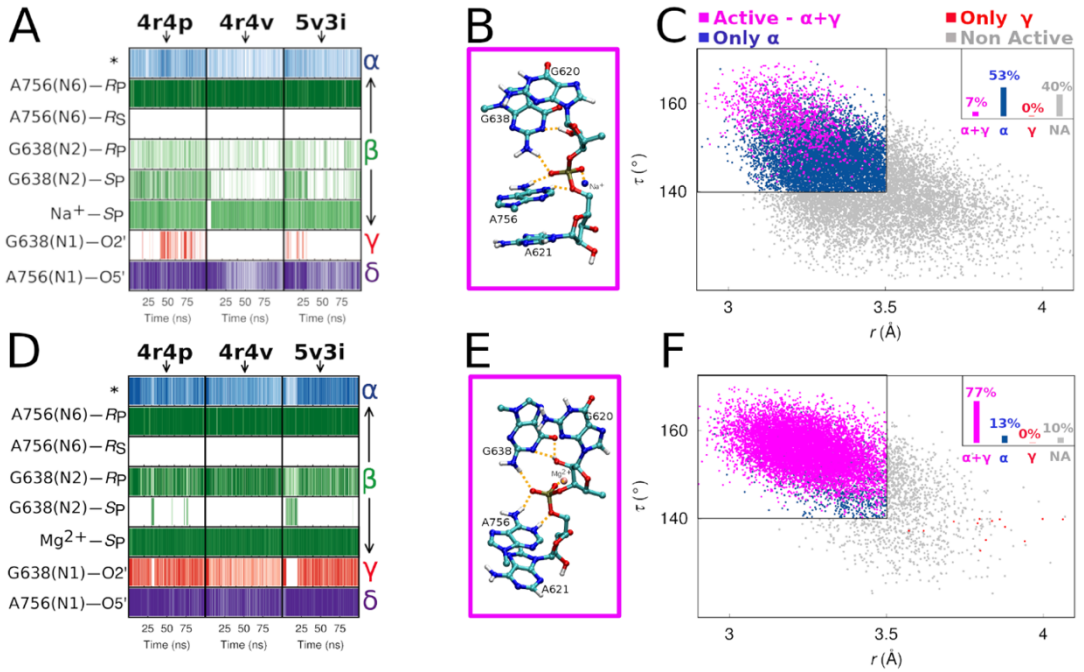

Figure 2.4 Active site of the VS ribozyme from MD simulations. Panels (A), (B), and (C) summarizes results from MD simulations based on the existing crystal structures, while panels (D), (E), and (F) summarizes results from simulations based on the existing crystal structures, with a Mg2+ ion bound at the *pro*S_p non-bridging oxygen of the scissile phosphate. The notation for modes of catalytic follow the framework outlined by Breaker where α is in-line aligment of the nucleophile, scissile phosphate and leaving group, β is electrostatic stabilization of the non-bridging oxygens δ is activation of the nucleophile and ɣ is stabilization of the leaving group. Panels (A) and (D) depict the occupancy the active site interactions during the various MD simulations. The columns correspond to simulations departing from the three crystal structures, while the rows correspond to the different active site hydrogen bonding interactions as indicated in the figure legends. The first row, indicated by an "*" symbol refers to inline fitness, which is dictated by the τ (O2'-P-O5') angle and the (O2')–P distance defined arbitrarily as $\tau \geq 140°$ for angle (O2')–P ≤ 3.5 Å. For the various hydrogen bonding interactions and metal-ion interaction, interactions were defined ≤ 2 Å for heavy atom-hydrogen distance, and ≤ 2.5 Å for heavy atom-metal ion distance, respectively. Panels (B) and (E) illustrate representative snapshots of the catalytically active state of the ribozyme observed in the simulations. Panels (C) and (F) are scatter plots depicting the active site conformation of the ribozyme in the MD simulations. The plots are constructed in the 2D space of the angle (y-axis) and the (O2pime)-G638(N1) distance (x-axis) and include data from simulations departing from all three crystal structures. The configurations are classified into 4 categories – configurations that exhibit both α and γ catalysis (magenta), only α catalysis (blue), only γ catalysis (red), and configurations that do not exhibit either α or γ catalysis (non-active, gray). The black rectangle outlines the region that exhibits α catalysis.

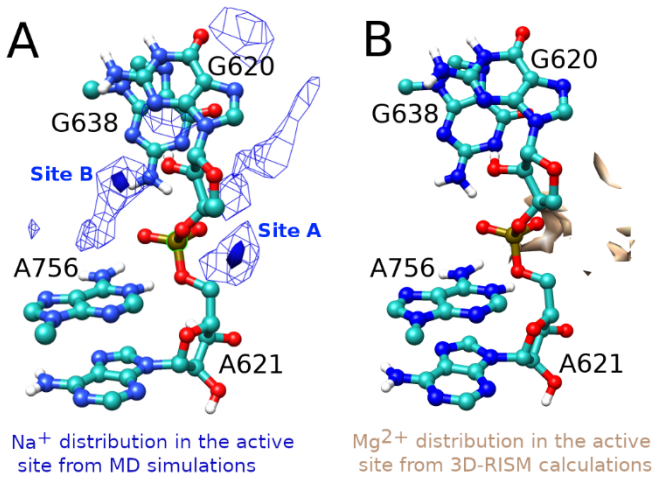

Figure 2.5 Investigation of metal ion binding sites in the ribozyme active site. (A) Na^+ ion occupancy plots in the active site region, calculated from MD simulations. The blue solid surface represents regions of top 30% of occupancy, and the blue mesh represents regions of top 70% of occupancy. (B) Mg^{2+} ion binding sites in the active site obtained from 3D-RISM calculations. The pale pink surface represents the top 10% of Mg^{2+} ion isodensity. As illustrated in panel (A), during the MD simulations, cationic charge density is largely localized in two regions of the active sites; site A, which is close to the *pro*S_p non-bridging oxygen of the scissile phosphate, and site B, which a bridging position between the 2'O-nucleophile and the *pro*R_p non-bridging oxygen of the scissile phosphate. The 3D-RISM calculations (B) suggest an Mg^{2+} occupies site A with much higher probability than site B.

Given the large thio effects observed and the computational insight that a divalent metal ion likely occupies a position near the active site, we tested rate of cleavage of G620 R_p and S_p thio substrates in the presence of a thiophilic metal ion. Two prior studies had investigated metal ion rescue for the scissile phosphate and did not observe any rescue. However, as mentioned previously, those studies were complicated by the use of a mixture of diastereomeric substrates (Kovacheva et al. 2004) or observation of the reverse reaction rather than cleavage (Zamel and Collins 2002). Furthermore, both studies tested for rescue in the presence of Mn^{2+} rather than the more thiophilic Cd^{2+}. Mn^{2+} ions are known to enhance the rate of phosphate as well as phosphorothioate substrates (Pecoraro, Hermes, and Cleland 1984). We investigated metal ion rescue with Cd^{2+} in a background of 10 mM Mg^{2+} in an effort to identify the putative metal ion

binding site. The results are summarized in Table 2.1 and Figure 2.3. In the oxo background, Cd^{2+} has a minimal impact on the rate of cleavage at low concentrations, but inhibits cleavage when the concentration of Cd^{2+} approaches that of Mg^{2+}. The presence of 20 μM Cd^{2+} stimulated the rate of cleavage for the S_P thio substrate to 0.0053 min^{-1}, corresponding to at least a 53-fold enhancement over rate of cleavage in the absence of Cd^{2+} and a metal ion rescue of at least 59. Note, the actual metal ion rescue is somewhat higher, but since the rate in absence of Cd^{2+} is less than the limit of detection, we assume a rate of 10^{-4} min^{-1}. In contrast to the S_P thio substrate, the R_P thio substrate exhibits no enhanced cleavage in the presence of Cd^{2+} corresponding to a metal ion rescue of one (no rescue) indicating that the stimulatory effect of the thiophilic metal is site specific. Additionally, we tested the effect of metal ion rescue in the G638I, A756(3cP) and double mutant ribozyme backgrounds and observed metal ion rescues of 9, 15 and 12, respectively, for the S_P thio substrate, and metal ion rescues of about one for the R_P thio substrate for each variant. These data provide support for a mechanism wherein a divalent metal ion specifically coordinates to the *pro*S_P non-bridging oxygen in all ribozyme variants.

Motivated by the results from the metal ion rescue experiments, we sought to investigate the ramifications of a Mg^{2+} ion in ribozyme active site dynamics. The York laboratory re-propagated MD trajectories, departing from the different crystal structures, with a Mg^{2+} ion bound at the G620 S_P non-bridging oxygen (site A in the active site). The results of these simulations are analyzed following the same criteria as the simulations without Mg^{2+} and are presented in Figure 2.4D-F. Interestingly, as illustrated by the interaction maps (Figure 2.4D), these independent trajectories converge to an active site ensemble that meets all the criteria for an activated ribozyme: G638 positioned for 2'O-nucleophile activation, A756 positioned for 5'O-leaving group stabilization, and a τ angle approaching 180º. Since A756 remains stably

positioned for leaving group stabilization throughout these trajectories, we again evaluated conformations of the phosphate reaction center with respect in-line alignment (τ near 180º) and 2'O-nucleophile activation (G638(N1) positioned near the 2'O-nucleophile). The distribution of phosphate reaction center conformations in these simulations (Figure 2.4F) reveals only a small fraction of the observed configurations meet one or neither of these conditions (13% and 10%, respectively) The majority of the configurations (77%) are conducive to catalysis both with respect to in-line alignment and nucleophilic activation. Additionally, stable interactions are observed between the exocyclic amines of G638 and A756 and the *proR*$_p$ oxygen, and between the Mg^{2+} ion and the *proS*$_p$ oxygen (Figure 2.4D). The high color intensity of these interaction maps reflects that conformations with the corresponding interactions are consistently populated. Comparison of these simulations to those conducted in the absence of the active site Mg^{2+} ion, thus suggests that the divalent metal ion enhances catalysis in part by helping to organize the active site.

The Mg^{2+} binding site during these MD simulations is described in Figure 2.6. The Mg^{2+} ion remains mostly localized in the simulations and, apart from the G620(*proS*$_p$) non-bridging oxygen, maintains an inner sphere contact with the N7 of G623. In two of the three simulations, the metal ion maintains an inner sphere contact with the A621(*proR*$_p$) non-bridging oxygen and interacts with G638(O6) via a water molecule, while in one simulation, the metal ion moves up in the active site to form an inner sphere contact with the G638(O6) and interact with the A621(*proR*$_p$) non-bridging oxygen via a water molecule. In each of the simulations, two other water molecules complete the hexacoordination of the ion.

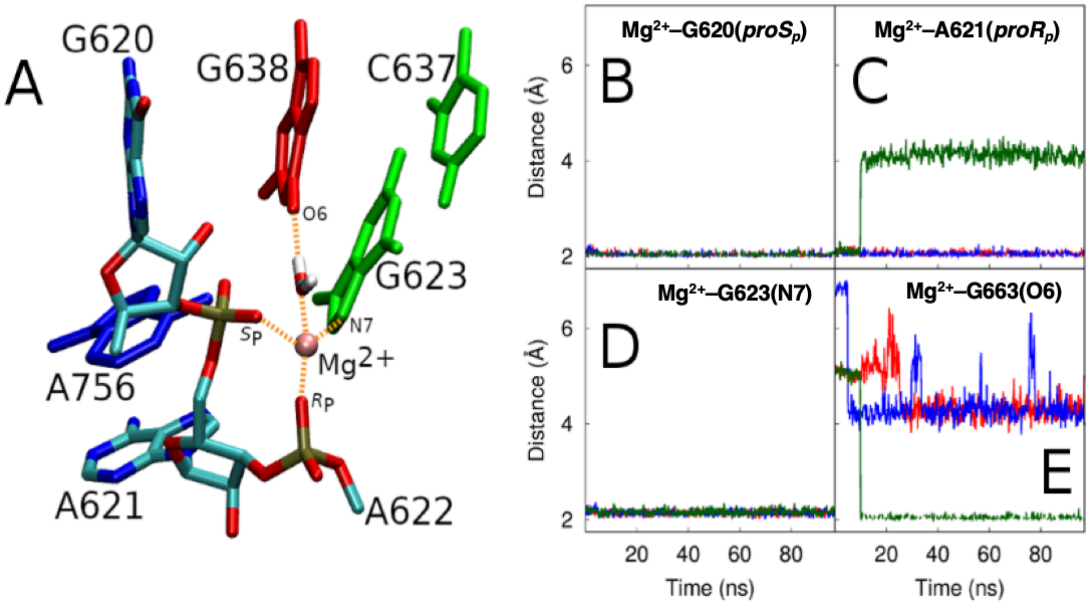

Figure 2.6 The proposed VS active site Mg^{2+} ion binding. (A) Cartoon depiction of the Mg^{2+} ion binding site. (B)–(E) illustrate the various Mg^{2+} coordination distances during the MD simulations: The Mg^{2+} ion stably interacts with *pro*S_p(G620) and G623(N7) throughout the duration of all trajectories (B and D) and *pro*R_p(A621) throughout two out of three trajectories (C). Interaction between G638(O6) and the catalytic Mg^{2+} ion is speculative, but the interaction exists throughout one trajectory (although at the exclusion of the *pro*R_p(A621) interaction).

We sought to validate the Mg^{2+}-bound model by first testing for metal ion rescue at the downstream phosphate, A621. Previous studies showed a substantial thio effect at the phosphorothioate downstream of the scissile phosphate rescuable with Mn^{2+} (Sood, Beattie, and Collins 1998, Kovacheva et al. 2004) but lacked clarity on the stereochemistry of the putative metal ion–phosphate interaction. In presence of 10 mM Mg^{2+}, the A621-S_P thio substrate cleaves with a rate of 0.029 min^{-1} corresponding to a modest thio effect of about 11. The A621-R_P thio substrate, on the other hand, cleaves with a rate below the limit of detection, corresponding to a thio effect of at least 3000. In the presence of 20 µM Cd^{2+}, cleavage of the A621-S_P thio substrate remained similar (0.033 min^{-1}) corresponding to a metal ion rescue of about 1.2, but that of the A621-R_P thio substrate accelerated at least 190-fold to a rate of 0.019 min^{-1},

corresponding to metal rescue of 212. These data strongly suggest that the *proS$_p$* non-bridging oxygen of the phosphate downstream of the cleavage center coordinates a divalent metal ion. Additionally, we tested cleavage with a G623(7cG) ribozyme variant, which eliminates the putative G623(N7)–Mg^{2+} interaction. This ribozyme failed to cleave the phosphate substrate with a rate the detectible range implying that G623(N7) plays an important role in catalysis. These data provide crucial evidence in support of our proposed metal binding site.

The consensus view of VS catalysis holds that G638 and A756 function as general base and general acid, respectively (Lilley 2004, Jimenez, Polanco, and Luptak 2015). Although significant circumstantial evidence exists to support this hypothesis (Lafontaine et al. 2001, Lafontaine et al. 2002, Wilson, McLeod, and Lilley 2007, Jaikaran et al. 2008, Wilson et al. 2010, Smith and Collins 2007), blind spots in our understanding remain. For instance, phosphorothioate rescue experiments (Wilson et al. 2010) demonstrate the functional linkage between A756 and 5′O-leaving group, but those data leave open the possibility of catalysis through a mechanism other than proton transfer. Also, no data to-date provide a functional linkage between G638 and the 2′O-nucleophile. Moreover, if general acid and general base catalysis do govern the VS catalytic mechanism, no information is available regarding the nature of the transition state in terms of extent of proton transfer neither from the putative general acid nor to the general base. To shed light on precise roles of A756 and G638 in VS catalysis, we observed the dependence of rate on pH for a series of A and G analogs with different electronic properties.

In general acid-base catalysis, the intrinsic rate constant should depend log-linearly on the pK_a of the general acid and base. Plotting log(k_{cat}) against pK_a gives a so-called Brønsted plot, the slope of which corresponds to a Brønsted coefficient (α or β), which is a measurement

of the sensitivity of the reaction to acid or base strength and reflects the extent of proton transfer (Anslyn and Dougherty 2006). In practice, measurement of Brønsted coefficients in ribozyme (or enzyme) catalysis is complicated by the fact that alterations to nucleobases that affect pK_a often also impact other aspects of catalysis. For instance, mutation of guanine to inosine results in an omission of an exocyclic amine which interacts with the p*ro*R_p non-bridging oxygen of the scissile phosphate, thus such a mutation is unsuitable for Brønsted analysis. To avoid this problem, we employed a series of purine analogs with endocyclic nitrogen perturbations that exhibit a broad range of microscopic pK_as, but differ structurally only in respect to the insertion and/or deletion of endocyclic nitrogens. These "isofunctional" purine analogs thereby leave the Watson-Crick face and exocyclic substituents of the nucleobase intact, but provide a range of nucleobase pK_as. If the charge on the nucleobase under investigation changed between the ground state and transition state of the reaction consistent with proton transfer, then k_{cat} for the analogs should vary log-linearly with pK_a a slope equal to the change in charge. Alternatively, if the charge on the nucleobase under investigation does not change over the course of the reaction, or if the endocyclic nitrogens perturbations affect catalysis through some other mechanism other than pK_a pertubation, then the k_{cat} will remain constant, or its relationship with pK_a will diverge from log-linearity.

To test the extent of proton transfer between the general acid, A756, and the 5′O-leaving group, we observed the rate of cleavage over a range of pH values for ribozymes with adenosine (WT), 3-deazaadenosine (3cA), 7-deazaadenosine (7cA), 8-azaadenosine (8nA), 8-aza-7-deazaadenosine (8n7cA), and 3-deazapurine (3cP) at the 756 position. The resulting pH-profiles (Figure 2.7 and Table 2.2) were fitted to a double-ionization model giving two apparent pK_as and an intrinsic rate constant, k_{cat}. All ribozymes revealed pH-profiles with two observable titrations:

one around pH 8.5 corresponding to the ionization of putative general base, G638, and the other ranging from 5-8 corresponding to the ionization of the purine at position 756. The pK_as and k_{cat} values obtained from the pH values were used to construct a Brønsted plot for the A analogs, which (excluding 3cP) revealed an α value of 0.23 (Figure 2.9A). The observed linear relationship strongly suggests that A756 is involved in proton transfer and the deviation from linearity observed for the A756(3cP) ribozyme results from the deletion of A756(N6), which coordinates the $proR_p$ oxygen of the scissile phosphate. The small Brønsted coefficient observed ($\alpha = 0.23$) indicates a) that proton transfer from A756 occurs in the rate-limiting step and not in a pre-equilibrium step and b) that the extent of proton transfer is only partial in the transition state. Both must be true since pre-equilibrium proton transfer or a transition state with complete proton transfer should result in Brønsted coefficients of 0 and 1, respectively. Thus, an observed α value between 0 and 1 suggests partial proton transfer in the rate-limiting step

We repeated the same procedure to investigate proton transfer to the putative general base, G638, with a series of substrates containing guanosine (WT), 7-deazaguanosine (7cG), 8-azaguanosine (8nG), 6-thio-guanosine, or 7-deaza-5-azaguanosine (also known as "P" nucleoside (Kim et al. 1978, Krauch et al. 1988, Georgiadis et al. 2015) here called P*) at the 638 position (Figure 2.8 and Table 2.2). All substrates revealed bell-shaped pH-profiles with a rate-stimulating titration between pH values of 5.2-5.8 with the notable exception of the G638P* substrate which showed only a single titration at 6.1, presumably because the pK_a of P* is too low to be observed over the pH range tested. The Brønsted plot constructed from the pK_a and k_{cat} values extracted from the pH-profiles reveal a linear dependence on pK_a of the G analogs with a slope near 1 ($\beta = 0.79$) (Figure 2.9B). These data strongly suggest that G638 participates in proton transfer during VS catalysis. We caution that the trendline should be interpreted only

qualitatively, therefore, although the observed slope is technically less than 1, these data cannot meaningfully distinguish between a β value less than or equal to 1.

Of particular interest is the coherence of the G638(6sG) substrate with linearity; if mutation of G638(O6) to sulfur meaningfully altered the VS active site, the G638(6sG) substrate would be expected to deviate from linearity under Brønsted analysis. The absence of such a defect suggests that the mutation of G638(O6) leaves the VS active site unaltered. Prior data, reproduced in our lab, showed that mutation of G638 to 2-aminopurine (2AP) results in a significant rate defect (>5000-fold) (Wilson, McLeod, and Lilley 2007, Jaikaran et al. 2008); however, in the absence of Brønsted analysis, it was impossible to decouple the effects of the pK_a shift and the loss of the G638(O6) atom. Comparison of the reactivity of the P* to 2AP nucleotides is informative since both have approximately the same microscopic pK_a(Krishnamurthy 2012), but P* reacts with a maximal rate only about 20-fold slower than wild type. Coupled with the observation that the G638(6sG) mutation adheres to linearity under Brønsted analysis, these data suggest that G638(O6) plays a role in catalysis that a sulfur atom at the same position can also support. Although the exact role for G638(O6) remains unclear, it may contribute to catalysis by positioning the active site metal ion through a water-mediated interaction. Alternatively, the volume occupancy of G638(O6) within the active site could help position G638 for nucleophilic activation.

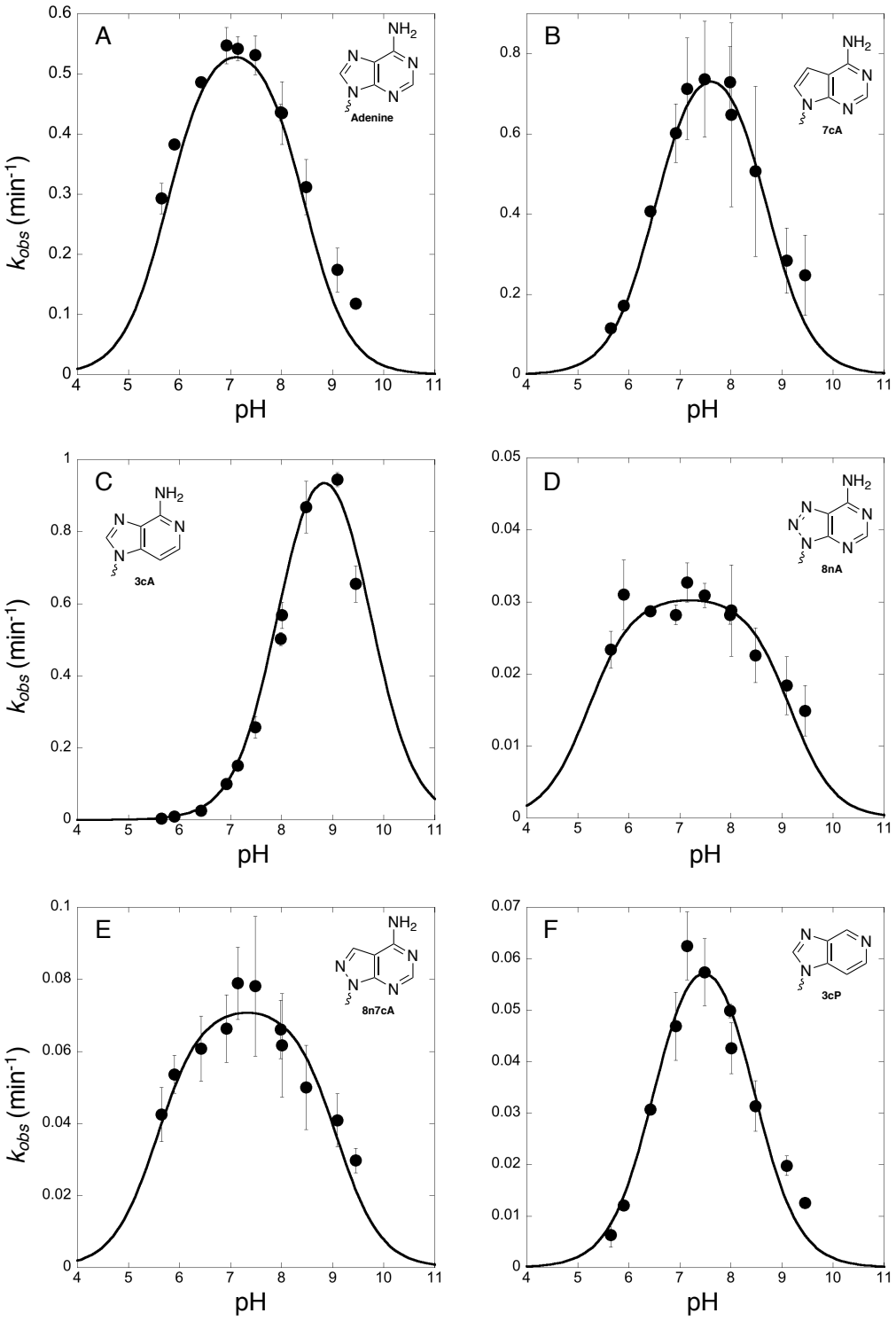

Figure 2.7 pH rate profiles for VS ribozymes with A756 mutations. (A) Wild type/Adenine, (B) 7-deazaadenine (7cA), (C) 3-deazaadenine (3cA), D) 8-azaadenine (8nA), E) 8-aza-7-deazaadenine (8n7cA) and F) 3-deazapurine (3cP). All pH-profiles were fit to a model for double ionization the results of which are summarized in Table 2.2.

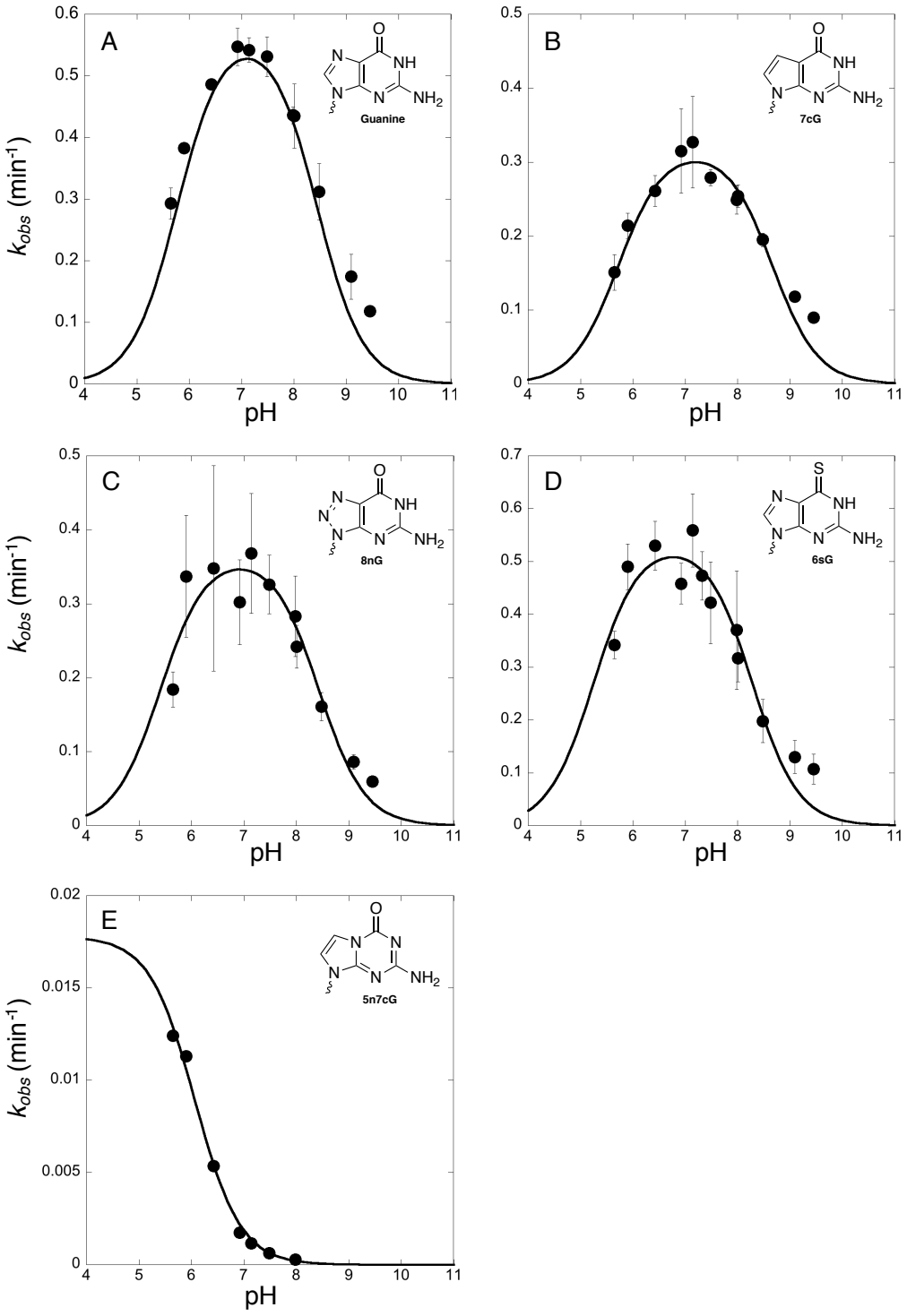

Figure 2.8 pH rate profiles for VS substrates with G638 mutations. (A) Wild type/Guanine, (B) 7-deazaguanine (7cG), (C) 8-azaguanine (8nG), (D) 6-thioguinine (6sG), and (E) 5-aza-7-deazaguanine (5n7cG or P*). All pH-profiles were fit to a model for double ionization with the exception of 5n7cG/P*, which was fit to a model for a single ionization. The results of a fits are summarized in supplemental Table 2.2.

Ribzoyme	Substrate	k_{cat} (min^{-1})	$pK_{a,1}$	$pK_{a,2}$
Wild Type	Wild Type	270 ± 120	5.8 ± 0.1	8.4 ± 0.1
A756(7cA)	Wild Type	120 ± 50	6.5 ± 0.1	8.7 ± 0.1
A756(3cA)	Wild Type	70 ± 40	8.0 ± 0.1	9.7 ± 0.2
A756(8nA)	Wild Type	260 ± 160	5.2 ± 0.2	9.1 ± 0.1
A756(8n7aA)	Wild Type	230 ± 110	5.6 ± 0.1	9.1 ± 0.1
A756(3cP)	Wild Type	6 ± 3	6.5 ± 0.1	8.4 ± 0.1
Wild Type	G638(8nG)	120 ± 40	*5.8 ± n.a*	8.3 ± 0.1
Wild Type	G638(7cG)	270 ± 60	*5.8 ± n.a*	8.7 ± 0.1
Wild Type	G638(6sG)	100 ± 30	*5.8 ± n.a*	8.0 ± 0.2
Wild Type	G638(P*)	0.018 ± 0.001	6.1 ± 0.1	

Table 2.2 Fitted parameters of from pH rate profiles in figures 2.7 and 2.8. All profiles were fit to a model for double ionization with the exception of the G638(P*) mutant substrate, which was fit to a model for a single ionization. Italicized pK_a values were fixed in data fitting and thus have no associated error.

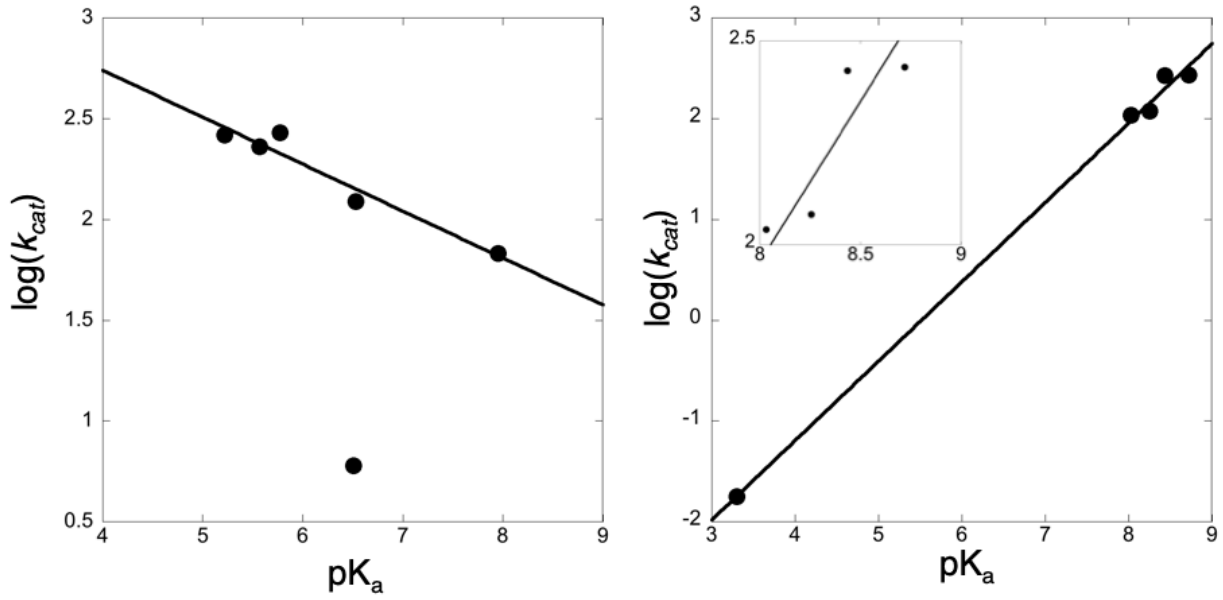

Figure 2.9 Brønsted plots for VS ribozymes. Panel (A) shows the Brønsted plot for A analogs fitted for WT, 7cA, 3cA, 8nA, and 8n7cA. 3cP was omitted from the fitting because it lacks an exocyclic amine. Panel (B) shows the Brønsted plot for B analogs fitted for WT, 7cG, 8nG, 6sG, and P*. The macroscopic pK_a of P* was estimated from its solution titration in solution. Fitting of A analogs reveals $\alpha = 0.23 \pm 0.03$ while fitting of the G analogs reveals $\beta = 0.79 \pm 0.03$.

Taken together, these data strongly implicate the catalytic nucleobases, A756 and G638, in general acid-base catalysis. Proton transfer between A756 and the 5′O-leaving group occurs in the rate-limiting step and the extent of transfer is partial in the transition state. Brønsted analysis implicates G638 in proton transfer; the data suggest that proton transfer has advanced significantly in the transition state but lack the resolution to distinguish between pre-equilibrium or concerted proton transfer for the general base.

To investigate the catalytic reaction pathway computationally, the York laboratory performed multi-dimensional QM/MM simulations using the finite temperature string (FTS) method employing the semi-empirical Hamiltonian AM1d/pho-T (Nam et al. 2007). The FTS method has been shown to be a powerful tool in determining favorable reaction pathways in multidimensional phase-space (Rosta et al. 2011, Ganguly et al. 2014). Herein, three reaction coordinates were considered, namely the general base proton transfer coordinate represented by the difference between the G638(N1)-G638(H1) and O2'-G638(H1) distances, the phosphorus bond breaking/forming coordinate represented by the difference between the P-O2' and P-O5' distances, and the general acid proton transfer coordinate represented by the difference between the A756(N1)-A756(H1) and O5'-A756(H1) distances. The FTS simulations suggested a sequential catalytic pathway in which the deprotonation of the 2'O-nucleophile by G638 occurs initially, as a separate step, followed by RNA backbone cleavage and leaving group departure; the associated free energy profile along the pathway suggested the latter to be rate-limiting (Figure 2.10). Given the known limitations of the AM1d/pho-T method, free energies obtained from these simulations are expected to be over-estimated; but their qualitative trend along the pathway is expected to be meaningful.

Brønsted analysis of the G638 analogs and preliminary FTS simulations suggested the possibility that proton transfer from the 2'O-hydroxyl nucleophile occurs in a pre-equilibrium step. Therefore, the chemical step was investigated in more detail starting from a configuration with a deprotonated 2'O-nucleophile. We calculated the free energy surface underlying the reaction using extensive *ab initio* 2D umbrella sampling simulations in the space of the phosphorus bond breaking/forming and the general acid proton transfer coordinates described earlier. The *ab initio* 2D surface is in excellent agreement with the reaction pathway obtained from the FTS simulations (Figure 2.10B), and suggest that the P-O2'/P-O5' bond formation/cleavage and general acid proton transfer occurs in a concerted fashion. In order to obtain better resolution of free energy along the reaction pathway, we performed additional *ab initio* umbrella sampling simulations along the converged pathway obtained from the FTS simulations, the results of which are shown in Figure 2.10[C-D]. These simulations reveal a free energy barrier of ~ 10 kcal/mol which, using the Arrhenius rate equation, corresponds to an intrinsic rate constant of about 10^4 s^{-1} (assuming a prefactor of 1 ps^{-1}). This calculated rate constant is consistent with the intrinsic rates obtained for certain fast-cleaving VS constructs (Zamel et al. 2004, Smith and Collins 2007) ($0.14*10^4$ s^{-1}), but is higher than the rates observed in this work. Presumably, fast dynamical equilibria reduce the observed rate of cleavage, especially in the *trans*-constructs employed in this study that require substrate docking; these processes are not accounted for in the QM/MM calculations. Thus, the estimates of reaction rate constants obtained from the simulations represent an upper limit of plausible intrinsic rate constants. The transition state obtained from these simulations (Figure 2.4D) is a "late" transition state in which the P-O2' bond is fully formed, P-O5' bond is halfway broken, and the proton from A756 partially transferred to the 5'O leaving group, as predicted by the LFERs.

Lastly, to determine if the Mg^{2+} ion was directly involved in the chemical steps of the reaction, we carried out analogous QM/MM simulations, after replacing the Mg^{2+} ion by a Na^{+} ion. The results obtained from these simulations are rather similar to those described above (in presence of the Mg^{2+} ion), suggesting that the Mg^{2+} ion does not directly take part in the reaction and is mostly essential for active site organization.

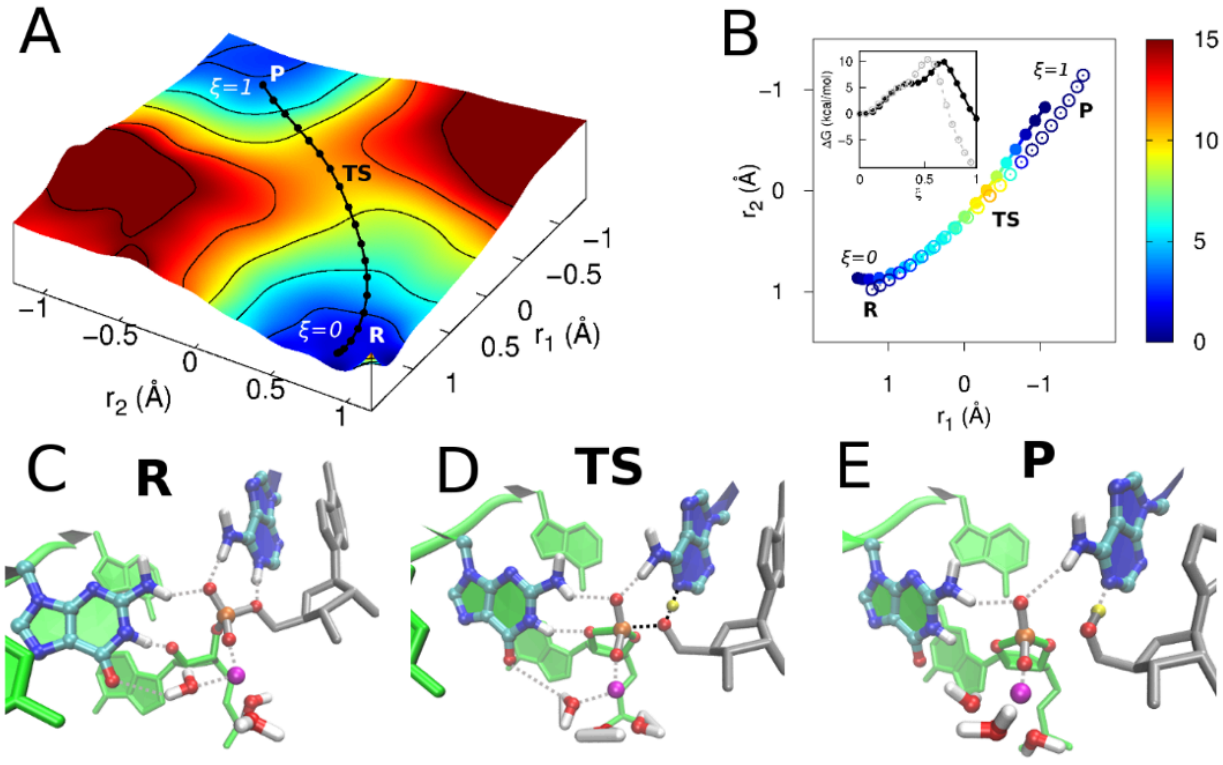

Figure 2.10 Reaction landscape for VS catalysis. (A) The 2D free energy surface underlying the catalytic reaction obtained using ab initio QM/MM umbrella sampling simulations. The solid black line corresponds to the converged pathway obtained FTS simulations at AM1d/pho-T level. (B) Converged pathways obtained from the FTS simulations in presence (solid line) and absence (dotted line) of active site Mg^{2+} ion. In (A) and (B), reaction coordinate r1 corresponds to the phosphorus bond breaking/forming coordinate represented by the difference between the P-(O2') and P-(O5') distances, and r2 corresponds to the general acid proton transfer coordinate represented by the difference between the A756(N1)-A756(H1) and O5'-A756(H1) distances. The color scale denotes relative free energy values in units of kcal/mol. Inset in (B) shows 1D free energy profiles of the pathways obtained in presence (black) and absence of the active site Mg^{2+} ion. (C-E) illustrates cartoons of representative reactant, transition, and product states of the reaction pathway obtained in presence of the active site Mg^{2+} ion.

2.4 Discussion

Ribozymes use two main chemical moieties for catalysis: metal ions and nucleobases. From biophysical studies spanning nearly three decades, the consensus view held that the VS catalytic mechanism depended entirely on nucleobase catalysis and the responsibilities of metal ions were restricted to structural organization. Herein, we presented a combination of computational and experimental data that shed light on the roles of divalent metal ions in VS ribozyme catalysis and helped to clarify the roles of the catalytic nucleobases, A756 and G638. Using stereospecific phosphorothioate substitutions, Cd^{2+} ion rescue experiments and MD simulations, we identified a catalytic metal ion that coordinated through the *pro*S_p oxygen of the scissile phosphate, the *pro*R_p oxygen on the downstream phosphate and G623(N7) that is critical for catalysis an helps organize the active site. Dynamics of the active site in the presence and absence of this metal ion indicates that, in addition to electrostatic stabilization of the negative charge on the non-bridging oxygen, that the ion helps arrange the active site in a configuration with a) the 2'O nucleophile, scissile phosphorus atom and leaving group aligned for efficient S_N2 attack (τ near 180º) , b) the general base G638 well positioned to activate the 2'O nucleophile, and c) stable interactions of the A756 and G638 exocyclic amines to the *pro*R_p oxygen of the scissile phosphate that can stabilize the negative charge developing of the non-bridging oxygen during the catalytic reaction. Dynamic trajectories launched in the absence of a divalent metal ion lack these interactions, however, these data do not necessarily provide a causal link between the presence of the metal ion and the organization of the active site. Instead, dynamical simulations show that an activated catalytic configuration around the scissile phosphate required the presence of many interactions, the presence of which influence one another.

While the importance of the nucleobases A756 and G638 in VS ribozyme catalysis has been well-appreciated, significant ambiguity remained in the details of the mechanism through which each participates in the catalytic reaction. In this work, we resolved this issue by measuring thio effects of the WT ribozyme as well as ribozyme variants that have A756 and/or G638 mutated to analogs that lack the exocyclic amino groups. Large thio effects for R_p G620 thio substrates that were rescued in the context of active sites that lacked G638(N2), A756(N6) or both, provided compelling evidence that catalytic nucleobases provide electrostatic stabilization and help organize the active site through direct interactions with the scissile phosphate via their exocyclic amines. These interactions were supported by MD simulations in presence of the active site Mg^{2+} ion, wherein the G638 and A756 exocyclic amine – $proR_p$ interactions were observed to be stable throughout multiple independent trajectories.

Data that supports a functional linkage between A756 and the 5'O leaving group(Wilson et al. 2010) combined with evidence for proton transfer during the rate-limiting step(Smith and Collins 2007) has traditionally been interpreted evidence for general acid catalysis. However, this interpretation makes a key assumption: the in-flight proton corresponds to one transferred from A756 to the leaving group. We presented Brønsted analysis that provides the first direct evidence for proton transfer from A756 and indicates the proton is only partially transferred to the leaving group in the transition state. No functional linkage between G638 and the 2'O nucleophile has been demonstrated; however, their proximity in the crystal structures (and MD trajectories) combined with the sensitivity of the pH profile to G638 mutation(Wilson, McLeod, and Lilley 2007, Jaikaran et al. 2008) has been taken as evidence for general base catalysis. Here, we showed a Brønsted relationship between G analogs, consistent proton transfer to G638. Although these data cannot resolve between pre-equilibrium proton transfer and general acid

catalysis, QM/MM simulations assuming the former gave rise to models of a transition state consistent with partial proton transfer from A756 – hinting at the possibility that the rate-limiting initiates only after the nucleophile loses its proton.

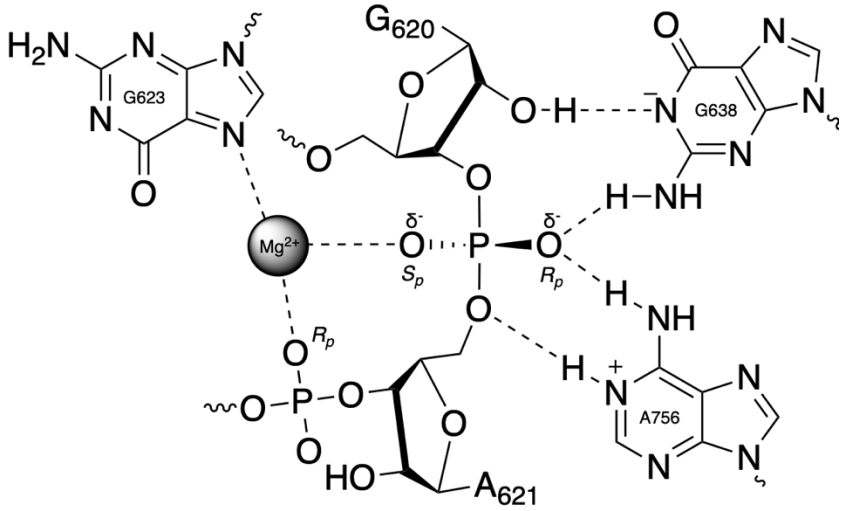

Figure 2.11 Updated schematic of the VS active site. The active site is organized by a catalytic metal ion coordinated through *pro*S_p(G620), *pro*R_p-(A621), and G623(N7). Interactions between A756(N6) and G638(N2) with G620 pro-Sp-O position the catalytic nucleobases. Consistent with classic view of VS catalysis, A756 stabilizes the 5'O-leaving group during the reaction while the G638, activates the nucleophile through proton transfer.

Together, the data presented here constitute a meaningful advance in our conceptualization of the VS ribozyme active site (Figure 2.11); however, significant questions remain. For instance, the experimental data provided here does not provide information regarding transition state structure with respect P-O5' bond fission or P-O2' bond formation. Kinetic isotope effect analysis for the 5'-O leaving group and 2'-O nucleophile would be could potentially provide clarity here. Additionally, these data provide information regarding interactions that organize the active site and contribute to catalysis, but they do inform the extent to which each of these interactions contributes to the observed rate enhancement or by what

mechanism. Mutational rescue experiments for phosphorothiolate substrates, for example, indicate that the exocyclic amines coordinate the *pro*R_p scissile phosphate oxygen, but cannot determine if these interactions contribute to catalysis by positioning the catalytic nucleobases, stabilizing the non-bridging oxygens, or by some other mechanism. Thus, much remains to be learned about the VS ribozyme and 2′-transphosphorylation in general.

Chapter 3: Characterization of the HDV Ribozymes Transition State

3.1 Introduction

The hepatitis delta virus (HDV) ribozyme represents one of the nine (and counting) classes of small endonucleolytic ribozymes that achieve site-specific self-scission by catalyzing the nucleophilic attack of a 2′-hydroxyl on the adjacent phosphate forming a 2′,3′-cyclic phosphate and 5′-hydroxyl termini (Figure 3.1). The RNA genome of the HDV virus encodes two forms of the ribozyme, genomic and antigenomic, which process the multimeric products of rolling circle replication into individual genomes. The HDV ribozyme serves as an outstanding model system for foundational studies of RNA catalysis because of its small size, availability of high-resolution crystal structures, and wealth of biochemical and kinetic data.

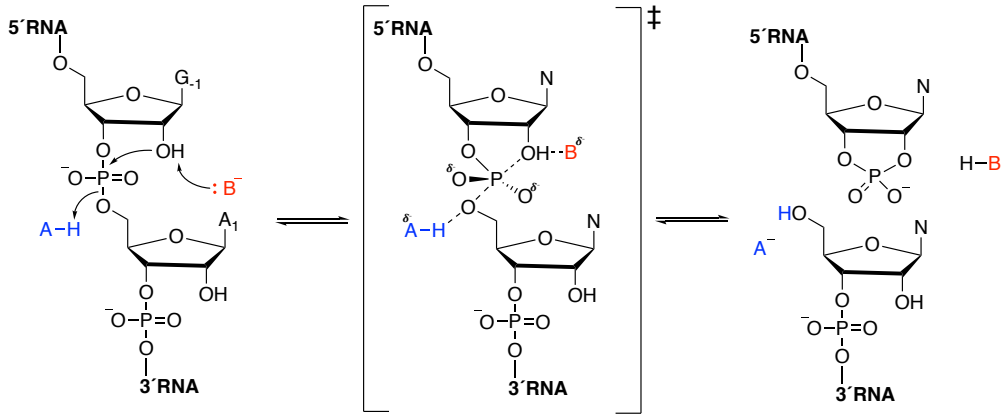

Figure 3.1 General scheme for 2′O-transphosphorylation where B^- and HA correspond to the general acid and base, respectively.

A significant body of functional, spectroscopic and crystallographic data support the role of C76 (antigenomic numbering) as a general acid that stabilizes the leaving group through proton transfer from N3 to the 5′-oxygen leaving group (Figure 3.2). Strong evidence for a functional linkage between C76(N3) and the 5′-oxygen leaving group comes from experiments that observed cleavage of substrates with 5′-bridging phosphorothiolates by ribozymes with perturbations to C76(Das and Piccirilli 2005). The hyper-labile 5′-phosphorothiolate substrates

do not require leaving group activation for cleavage, so the insensitivity to C76 mutations observed for these substrates suggests a role for C76 in leaving group activation. While these experiments provide evidence for a functional linkage between C76(N3) and G1(O5′), they do not necessarily indicate proton transfer. However, spectroscopic data showing that the pK_a of the rate stimulating limb of the pH-profile corresponds to the catalytic cytosine(Gong et al. 2007) and proton inventories that show at least two protons in-flight(Nakano, Chadalavada, and Bevilacqua 2000, Shih and Been 2001a) provide powerful corroborating evidence that C76 indeed functions as a general acid. Additionally, two studies (Perrotta, Wadkins, and Been 2006, Koo et al. 2015) show intermediate Brønsted coefficients for HDV catalysis for a range of imidazole or cytosine analogs suggesting that proton transfer from the C76 occurs in the rate-limiting step (consistent with general acid catalysis) and that the proton is only partially transferred from the general acid to the leaving group in the transition state.

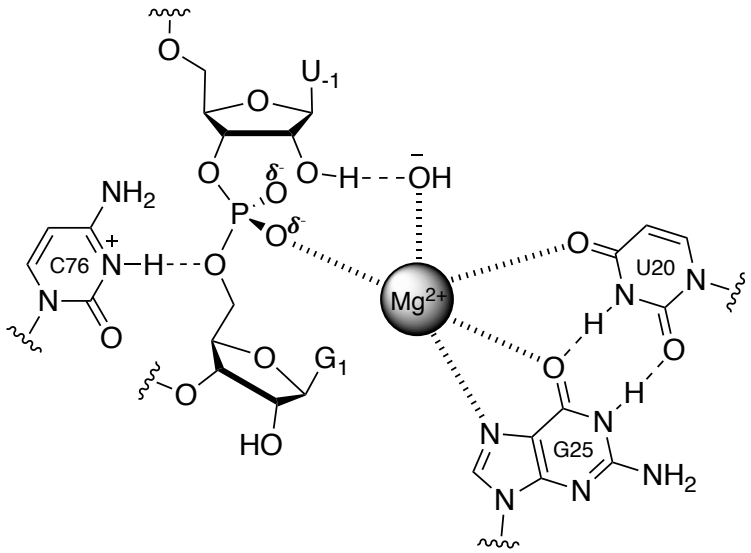

Figure 3.2 Schematic of the HDV active site. A divalent metal ion, position by the G25:U20 wobble pair positions a divalent metal ion coordinated to the *proR*$_p$ oxygen of the scissile phosphate. The general acid, C76, stabilizes the 5′O-leaving group during the reaction while a hydroxide ion coordinated to the catalytic metal ion activates the nucleophile.

In addition to the catalytic nucleobase, a divalent metal ion resides at the active site (Figure 2), positioned by a critical G•U wobble pair(Chen et al. 2013). A large thio effect for the R_p thio substrate and rescue in the presence of a thiophilic metal ion implicate the metal ion in an inner-sphere coordination to the proR_p non-bridging oxygen atom of the scissile phosphate, presumably stabilizing the developing negative charge on the non-bridging oxygen in the transition state (Thaplyal et al. 2013, Thaplyal et al. 2015). Consistent with this catalytic interaction, mutation of the G•U wobble pair eliminates the observed thio effects for the R_p thio substrate.

Regarding the mechanism for nucleophilic activation in HDV catalysis, some ambiguity remains; however, the best evidence suggests that a water molecule (or hydroxide ion) bound to the catalytic divalent metal ion acts as a general base (Figure 3.2). An inversion of the pH-rate profile in the absence of divalent ions(Perrotta and Been 2006) or in the presence of a mutation that perturbs the metal binding site(Chen et al. 2013) suggests that a metal-bound water accounts for one of the observed titrations. Additionally, proton inventory in a monovalent background shows only a single proton in-flight(Cerrone-Szakal, Siegfried, and Bevilacqua 2008) consistent with the loss of general base catalysis. While these data implicate a water-bound Mg^{2+} ion in nucleophilic activation and indicate that proton transfer from the nucleophile occurs during or before the rate-limiting step, they provide no information regarding the extent of proton transfer from the nucleophile in the transition state.

As outlined in the proceeding paragraphs, decades of mechanistic investigation for HDV and other endonucleolytic ribozymes have provided significant insight into the functional interactions that facilitate catalysis. Nevertheless, we know comparatively little about the structure of the transition state. The premise that enzymes facilitate catalysis by stabilizing

chemical transition states relative to ground states is foundational to modern enzymology(Van Holde, Johnson, and Ho 2006); therefore, this lack of knowledge of transition state structure constitutes a major gap in our understanding of ribozyme catalysis. For instance, it remains unclear if RNA and protein enzymes catalyze phosphoryl transfer through similar or disparate transition states. The former would be strongly suggestive of convergent evolution towards optimized active sites, whereas the latter would indicate multiple biologically feasible routes to RNA strand-scission. Here, we report the first ever complete set of heavy atom kinetic isotope effects for an endonucleolytic ribozyme in an effort to shed light on the relationship between transition states in RNA and protein enzymes.

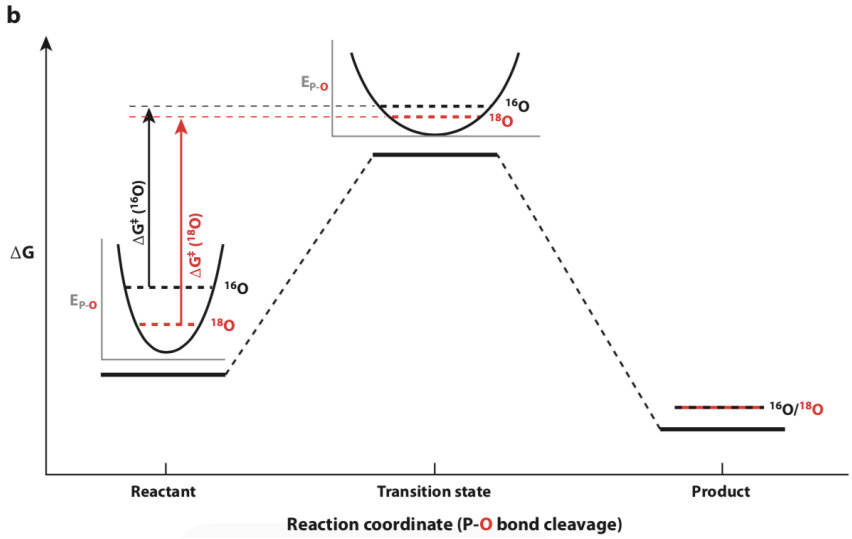

Figure 3.3. Reaction coordinate diagram for reaction involving the cleavage of a P–O bond. The difference in zero-point energies of the heavy and light isotopologues is larger in the reactant state (where O–P bond is intact) than in transition state (where the bond is partially lost). As a consequence, the reaction proceeds with a lower free energy barrier for the lighter isotopologue resulting in a normal isotope effect (k_{light}/k_{heavy} >1). Figure adapted from Lassilla *et al.* (Lassila, Zalatan, and Herschlag 2011)

Substitution of a single atom with a heavy isotope represents the smallest possible perturbation of a chemical system (Anslyn and Dougherty 2006) and the rate effect of isotopic

substitution reports directly on changes to the bonding environment of the substituted atom (Melander and Saunders 1987). The zero-point energy, or minimum vibrational energy state, of a chemical bond depends inversely on the mass of the atoms in the chemical bond, so increasing the mass decreases the zero-point energy (Kohen and Limbach 2006, Lassila, Zalatan, and Herschlag 2011) (Figure 3.3). Thus, for chemical reactions that involve the loss of a chemical bond there is a difference in the zero-point energies of heavy and light isotope containing reactants, but no difference for the products because those vibrational states are lost when the bond is broken. Consequently, there will be a larger energy barrier for the heavy-atom substituted bond, resulting slower rate constant ($k_{light}/k_{heavy} > 1$) giving rise to a so-called "normal" isotope effect. Inverse isotope effects ($k_{light}/k_{heavy} < 1$) can occur when the amount of bonding around the isotopically substituted atom increases. Although observation of kinetic isotope effects (KIEs) provides highly specific data, broad application of this methodology into complex biochemical systems has been limited by a number of factors (Harris et al. 2017). First, KIE studies require synthesis of substrates with atom specific isotopic substitution which have only recently been synthetically accessible(Weissman et al. 2015). Second, the difference in mass between heavy and light isotope of atoms substituted in heavy-atom KIE studies (C, N, O) is minimal, so the KIEs observed are generally on the order of a few percent. Consequently, detection of KIEs requires precise measurement of relative rates. Last, the observed isotope effects are the product of a number of physical factors including changes in the bonding environment around the labeled atom and movement along the reaction coordinate. Decoupling these factors complicates physical interpretation of the observed effects, but advances in computational models have aided in this endeavor.

Phosphoryl transfer reactions have been the subject of intense inquiry through biophysical methods including KIEs (Cleland and Hengge 1995) because their centrality to biological systems (phosphoryl transfer chemistry is essential to genetic inheritance, metabolic pathways and cellular signaling(Knowles 1980, Westheimer 1987)) and accessibility of appropriate substrates. Consequently, a framework for understanding phosphoryl transfer transition states is well-established in the literature (Lassila, Zalatan, and Herschlag 2011). Like all S_N2-type reactions, phosphoryl transfer proceeds via two bond alterations: the loss of the bond between the phosphate and the leaving group and the formation of a new bond between the nucleophile and the phosphate. Transition states can be thought of as existing on a simplified two-dimensional coordinate (Figure 3.4) where one axis represents bond formation and the other represents bond fission. Reactions where bond formation exceeds bond fission can be described as "tight" and have phosphorene-like transition states, whereas reactions where bond fission exceeds bond formation are described as "loose" and have metaphosphate-like transition states. For uncatalyzed (alkaline) reactions, increasing substitution results in tighter transition states such that monoesters generally exhibit looser transition states than di- and triesters(Cleland and Hengge 1995, 2006).

Heavy-atom KIE measurement has been employed to investigate a number ribozymes including the ribosome(Hiller et al. 2011) and a pyrimidine nucleotide synthesizing ribozyme(Unrau and Bartel 2003) and a wide-variety of protein enzymes(Schramm 2003, 2011). Although no KIEs have been obtained for any of the endonucleolytic ribozymes, KIEs have been measured for cleavage of a UpG dinucleotide by RNase A(Sowa, Hengge, and Cleland 1997, Gu et al. 2013a) as well as under acidic and basic conditions(Harris et al. 2010), which provide a useful basis for comparison with future KIE observations. Under basic conditions, UpG shows a

large normal leaving group KIE and a modestly inverse nucleophile KIE ($^{18}k_{lg}$ = 1.034 and $^{18}k_{nuc}$ = 0.984) corresponding to late, synchronous transition state with significant contributions from both bond fission and bond formation. For UpG cleavage catalyzed by RNase A, both KIEs shift towards unity ($^{18}k_{lg}$ = 1.014 and $^{18}k_{nuc}$ = 0.994) suggestive of an earlier transition state. However, interpretation of the leaving group effect is complicated by the fact that the observed effect is the product of offsetting contributions from protonation and O–P bond fission.

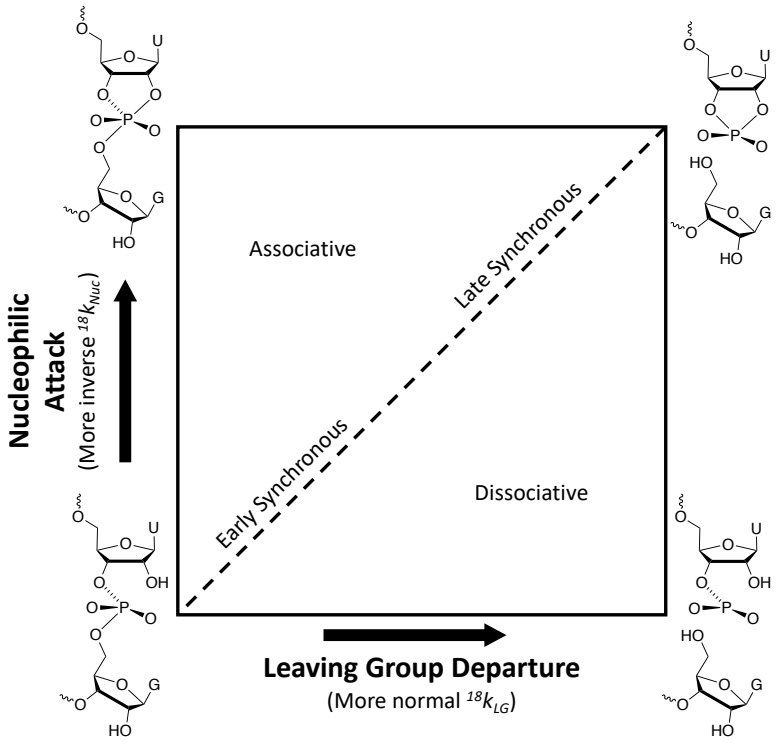

Figure 3.4 A simplified More O'Ferrall Jencks plot for 2′O-transphosphorylation. 2′O-transphosphorylation reactions consist of two components: leaving group departure (breakage of the (O5′)–P bond) and nucleophilic attack (formation of the (O2′)–P bond) represented on the x and y axis, respectively. Transition states with more leaving group departure than nucleophilic attack are characterized as dissociative and exist in the lower-right quadrant of this plot, whereas transition states with more nucleophilic attack than leaving group departure are characterized as associative and exist in the upper-left quadrant. Reactions with extents of leaving group departure and nucleophilic attack give rise to synchronous transition states, which can be characterized as either early or late depending whether the transition state is relatively reactant-like or product-like.

Here, we recapitulate the previously observed KIEs for UpG cleavage under alkaline conditions using a remote label methodology and use that methodology to observe KIEs for the O2′ nucleophile, O5′ leaving group and non-bridging oxygens in HDV catalysis. Comparison to other phosphoryl transfer reactions including, but not limited to, that catalyzed by RNase A suggest that HDV facilitates cleavage through a reaction pathway with a very loose, metaphosphate-like transition state. These data hint at "shallow" energy landscape for ribozyme catalysis where the catalytic active site can shift the transition state significantly from the solution reaction.

3.2 Methods

RNA oligonucleotides and constructs

The HDV enzyme strand was prepared by T7 transcription under standard conditions from a double-stranded template, which was prepared as follows. A pUC19 plasmid containing the full 66-nt ribozyme, was transformed into competent DH5α Escherichia coli cells and amplified, and the sequence was confirmed with sequencing, which was performed by the University of Chicago Core Facility. The plasmid was digested by EarI (New England Biolabs) to generate a double stranded DNA template that contains the T7 promotor sequence and a blunt end at the 3′-end of the ribozyme sequence. Following transcription, transcripts were purified first by phenol-chloroform extraction then by 6% denaturing polyacrylamide gel electrophoresis (dPAGE). The transcripts were visualized under UV light, excised from the gel and eluted overnight in TEN buffer (10mM Tris pH = 8, 1mM EDTA, 300mM NaCl) then concentrated on centrifugal filter units for use. WT HDV ribozyme employed in herein contains the sequence: 5′-GGG CAU CUC CAC CUC CUC GCG GUC CGA CCU GGG CAU CCG AGC ACU CGG

AUG GCU AAG GGA GAG CCA. This ribozyme construct, which has been employed previously in our laboratory (Das and Piccirilli 2005, Koo et al. 2015), is derived from the natural self- cleaving antigenomic HDV motif and contains a shortened P4 stem and a discontinuous J1/2 region. The numbering, with discontinuity in the P4 stem, follows that established for the antigenomic ribozyme (Shih and Been 2002).

Single stranded RNA substrates were prepared in-house by solid-phase synthesis using 5'-O-DMT-2'-O-TBDMS- 3'-phosphoramidites. Synthesis of phosphoramidites enriched for ^{18}O at the 2′O, 5′O or non-bridging positions have been described previously(Dai et al. 2008) (see Appendix B for more details) and were analyzed by mass spectroscopy to determine the extent of heavy atom enrichment at the target atom – 2′O labeled amidites were 80% heavy atom labeled and 5′O-labeled substrates were 98% heavy atom labeled. The wild type substrate employed in these studied has the sequence 5′-UUU GGG UCG GC where the nucleotides on either side of the scissile phosphate are underlined. Substrate II (SII) employed in all KIE studies described herein has the sequence 5′-UUU GGG UCA AC where the mutation of two G residues (underlined) downstream of the cleavage site disrupt ribozyme binding. For alkaline hydrolysis reactions, an analogous DNA/RNA hybrid oligomer was employed with the sequence 5′- uuU ggg uca ac where lower case nucleotides lack a 2′O-hydroxyl. Following deprotection, all oligos were purified by dPAGE before use, and substrates were 5′-end radiolabeled with T4 polynucleotide kinase (New England Biolabs) before use in kinetic studies unless otherwise indicated following manufacturers protocol.

RNA kinetics and data analysis

Ribozyme kinetic experiments were executed a described previously (Lu et al. 2018). Briefly, ribozyme RNA was incubated in water at 70º for 2 minutes to denature and allowed to

renature at room temperature for 10 minutes in the presence of reaction buffer (50nM Tris pH = 8, 10mM $MgCl_2$). The reaction was then initiated by the addition of radiolabeled RNA substrate RNA. Unless otherwise noted, typical self-cleavage reactions contained a trace amount (<1nM) of radiolabeled substrate and final concentration of 1uM ribozyme, typically in 10-15μLtotal volume. Aliquots of the reaction mixture were taken at appropriate time points and quenched in stop solution (97% formamide, 15mM EDTA, 0.1% w/v bromophenol blue and xylene cyanol) and rapidly chilled on dry ice. Cleavage products were separated from uncleaved substrate on a denaturing 20% polyacrylamide / 7M urea gel and quantified using a PhosphorImager with ImageQuant software (Molecular Dynamics).

For alkaline hydrolysis reactions, 0.5 μL5prime-end radiolabeled substrate was added to19.5 μL reaction buffer at the appropriate pH and incubated at 25ºC. At pH values between 12.0 and 14.0, reaction buffer was made by mixing NaOH (1 M, pH = 14) and NaCl (1 M) solutions to achieve the desired pH. Reaction aliquots of 1 μL were removed at appropriate time-points, quenched by adding 6 μL 1 M Tris-HCl pH 7.5 (final pH's of quenched reaction aliquots are typically no higher than 8) with 7 μL stop solution, and rapidly chilled on dry ice. Hydrolysis products were separated from unhydrolyzed substrate on a denaturing 20% polyacrylamide / 7M urea gel and quantified using a PhosphorImager with ImageQuant software (Molecular Dynamics).

Data for cleavage reactions were fit in KaleidaGraph (Synergy Software) to equation 1 where *f* is the fraction cleaved, A is the amplitude or endpoint of the reaction (typically ~98% for HDV cleavage reactions), k_{obs} is the observed rate constant and *t* is the time.

$$f = A(1 - e^{-k_{obs}t}) \quad (1)$$

The pH rate profile observed for hydrolysis of the RNA/DNA hybrid substrate was fit to a model for single ionization in equation 2 where k_{max} is the maximal rate.

$$k_{obs} = \frac{k_{\max}}{1+10^{pK_a - pH}} \quad (2)$$

Pulse Chase reactions

Pulse Chase reactions were employed to infer the forward commitment to catalysis. The underlying principles of this approach are described in detail elsewhere (Shih and Been 2000), but briefly in the simple kinetic framework outline in scheme 3, the enzyme substrate complex (E•S) can either dissociate to form free enzyme and substrate or proceed through the chemical step to form products. The forward commitment to catalysis (C_f) represents the partition between

$$E + S \underset{k_{-1}}{\overset{k_1}{\rightleftharpoons}} E\bullet S \xrightarrow{k_2} E + P_{3'} + P_{5'} \quad (3)$$

reactants and products from the enzyme substrate complex (equation 4). Since the observed

$$C_f = \frac{k_2}{k_{-1}} \quad (4)$$

isotope effects report V_{max}/K_m, reactions with large forward commitments will mask the observed isotope effect according to equation 5 where KIE_o is the observed isotope effect and KIE_i is the intrinsic isotope effect.

$$KIE_o = \frac{KIE_i + C_f}{1+C_f} \quad (5)$$

In an effort to quantify C_f we conducted pulse-chase experiments where a typical HDV ribozyme kinetic reaction was initiated ("pulsed") under standard condition, but the reaction was "chased" by the addition of the massive excess of unlabeled substrate (final concentration >400uM). Only radiolabeled substrate already bound to the ribozyme at the time of the chase

will proceed to form observable products. Thus, the observation of product after the chase is an indication of a significant C_f. The forward commitment can be calculated from these experiments using equation 6 where k_{conrol} is simply the observed rate constant for the cleavage reaction pre-chase and k_{chase} the observed rate constant for the cleavage reaction after addition of chase mixture.

$$C_f = \frac{k_{control}}{k_{chase} - k_{control}} \quad (6)$$

Note that the k_{chase} is essentially $k_2 + k_{-1}$ from scheme 3, so it is expected to be somewhat larger than $k_{control}$. For pulse-chase reactions employing HDV substrate II (SII), k_{chase} was much too fast to measure, but extrapolation of the of the chased reaction back to the time of the chase reveals that essentially no additional substrate cleaved after the addition of the chase consistent with a low forward commitment to catalysis.

Measurement of Kinetic Isotope effects

Kinetic reactions were conducted as described above except rather than a single ^{32}P radiolabeled substrate, KIE kinetic experiments employed a mixture of ^{32}P and ^{33}P labeled heavy and light isotopologues. About half of the reaction mixture was quenched when the reaction was 20-40% reacted while the remainder was allowed to react to completion – at least 4 hours. Both time-points and endpoints were run on 20% dPAGE gel to separate cleaved from uncleaved substrate. Substrate and product bands were visualized using a Typhoon PhosphorImager with a thin plastic sheet between the gel and the screen to block ^{33}P emissions. The fraction of ^{32}P-labeled substrate reacted could then be determined with ImageQuant software (Molecular Dynamics). Each product band was then excised from the gel and eluted overnight at 50ºC in a 3mL solution containing 2:1 ddH_2O:Solvable™ (PerkinElmer). The elution solution was then

added to 10mL Optima Gold scintillation fluid (PerkinElmer) and counted on a Tri-Carb 2900TR liquid scintillation counter (PerkinElmer) to determine the ratio of ^{32}P to ^{33}P. Each sample was counted for 5 minutes (along with blanks for background subtraction) over three cycles. Since the time required to count an entire experiment was significant relative to the half-lives of the isotopes, the counts of ^{32}P and ^{33}P observed for a particular vial were corrected for the effects of radioactive decay.

Counts per minute were divided into two channels: 0-300 and 300-1750keV. All of the emission from ^{33}P are detected in the low energy channel, but emissions from ^{32}P are detected in both channels. The ratio of ^{32}P to ^{33}P labeled substrates in the sample was determined by equation 7 where A is the number of counts in the low energy channel, B is the number of counts in the high energy channel and *r* is the ratio of ^{32}P counts in the high to low energy channels. Measurement of ^{32}P standards over a range concentration revealed that *r* shows a subtle dependence on the concentration of ^{32}P.

$$\frac{^{33}P}{^{32}P} = \frac{A - Br}{B(1+r)} \tag{7}$$

The observed isotope effect was then determined from the ratio of the midpoints and endpoints of each reaction and the reaction following equation 8 where *f* is the fraction reacted at the timepoint collected, R_p is the ratio of ^{33}P to ^{32}P product fraction at the midpoint and R_o is the ratio of ^{33}P to ^{32}P product fraction at the endpoint.

$$KIE_o = \frac{\log(1-f)}{\log(1-f\frac{R_p}{R_o})} \tag{8}$$

Finally, the observed isotope effect was corrected for the forward commitment factor and incomplete isotopic enrichment following equation 9 where *e* is the isotopic enrichment at the atom under investigation and C_f is the forward commitment factor.

$$KIE_i = \left(1 + \frac{KIE_o}{1 - KIE_o(1-e)}\right)(1 + C_f) - C_f \quad (9)$$

The KIEs presented here are the harmonic means of multiple KIE experiments with associated standard error of the mean.

3.3 Results

Heavy-atom KIEs correspond to relatively small differences in rate, so they are typically measured using competitive methods with mixtures of substrates containing ^{18}O and ^{16}O at one of the reactive oxygens(Kohen and Limbach 2006). Differences in reaction rate constants between the two isotopologues are reflected in depletion of the faster reacting substrate from the unreacted substrate population and/or enrichment of the faster reacting substrate in the product population. Analysis of the $^{18}O/^{16}O$ ratio as a function of reaction progress allows calculation of the KIE. Typically, the ratio of isotopologues is analyzed directly through mass spectroscopy following HPLC separation of the reacted and unreacted substrates to determine reaction progress. Alternatively, the ratio of isotopologues can be tracked via remote labels. Here, we used two radioisotopes, ^{32}P and ^{33}P, attached to the 5′-end of the HDV substrates and performed scintillation counting to determine the relative abundance of the two substrates (Hiller et al. 2010). Since, the reactions observed did not progress to completion (but both substrates exhibited identical endpoints) we tracked enrichment in the product population as compared to

the ratio of substrates in the endpoint population to calculate observed isotope effects (see methods).

In an effort to gain confidence in our methodology, we first measured isotope effects for a UpG-like substrate under alkaline conditions to allow comparison with corresponding KIE measurements made previously using mass spectrometry. The substrate employed in this calibration was 11 nucleotides in length with same sequence as the RNA substrate employed in subsequent HDV KIE studies, but lacked 2´-hyroxyl groups at all positions except the cleavage site; therefore, the substrate gave rise to a single product when subjected to alkaline hydrolysis. Cleavage of this substrate at pH = 14 gave isotope effects of $^{18}k_{nuc}$ = 0.987 ± 0.004 (64) and $^{18}k_{lg}$ = 1.026 ± 0.002 (22) (KIEs provided are the harmonic mean of multiple trials, the number of trials is given in parentheses) in reasonably good agreement with the prior KIE measurements KIEs obtained for UpG hydrolysis with mass spectroscopy (Table 3.1, Figure 3.5). Moreover, the relative rate of the substrates was insensitive to the orientation of the radiolabels (Figure 3.6).

The KIEs obtained via competitive experiments report apparent ratios of V_{max}/K_m; therefore, contributions from pre-chemical steps can affect the observed effects. In ribozyme catalysis, partial forward commitment (C_f) to catalysis resulting from a rate of substrate dissociation on the order of the rate of chemistry is a particular concern. Through a pulse-chase experiment(Shih and Been 2000), we measured the commitment factor for a *trans*-antigenomic HDV ribozyme construct previously employed in our lab(Koo et al. 2015) and observed a significant forward commitment to catalysis (Figure 7). Since commitments to catalysis shift the observed isotope effects towards unity, partially obscuring the observed effect, we sought to design constructs with enhanced dissociation from the ribozyme by disrupting the base pairs at

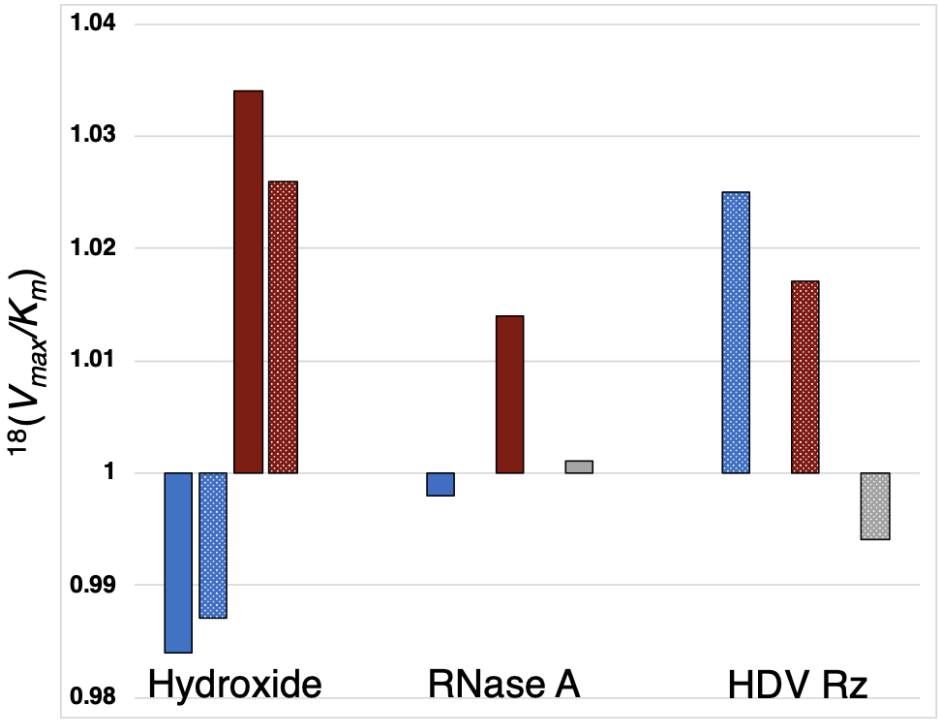

Figure 3.5. Kinetic isotope effects for hydroxide, RNase A and HDV catalyzed 2′O-transphosphorylation. Nucleophile isotope effects ($^{18}k_{nuc}$) are blue, leaving group effects ($^{18}k_{lg}$) are red and NBO effects ($^{18}k_{NBO}$) are grey. Isotope effects collected with mass spectroscopy are represented with solid bars and isotope effects measured with remote labels (this study) are represented with hatched bars.

	HDV Ribzoyme			Hydroxide	
	$^{18}k_{Nuc}$	$^{18}k_{LG}$	$^{18}k_{NBO}$	$^{18}k_{Nuc}$	$^{18}k_{LG}$
Measurments	93	26	27	57	19
KIE$_o$	1.019	1.016	0.994	0.993	1.018
Enrichment	0.80	0.98	0.98	0.80	0.98
C_f	0.02	0.02	0.02	0.00	0.00
KIE$_i$	1.024	1.017	0.994	0.991	1.019
SEM	0.001	0.003	0.004	0.002	0.003

Table 3.1 Parameters for calculation of isotope effects through remote label. KIE$_o$ refers to the observed isotope effect direct measurement. Enrichment $^{18}O/^{16}O$ fraction in the heavy labeled substrate. C_f is the forward commitment to catalysis: for HDV catalyzed reactions with was assumed to be 0.02, the upper-limit on our estimation of C_f. KIE$_i$ is the intrinsic isotope effect after correction for forward commitment and isotopic enrichment. SEM is the standard error of mean.

the 3′end of the substrate. The resulting substrate shows minimal forward commitment to catalysis (C_f < 0.0) (Figure 3.7).

Once confident in the fidelity of the remote label methodology and with a substrate with minimized forward commitment, we measured KIEs for the 2′O-nucleophile, 5′O-leaving group and non-bridging oxygens by the remote label competitive method. After correcting for commitment and isotopic enrichment we observed a large normal isotope effect for the 2′O-nucleophile, $^{18}k_{nuc}$ = 1.024 ± 0.001 (93), a modest normal effect on the 5′O-leaving group, $^{18}k_{lg}$ = 1.017 ± 0.003 (26), and a small inverse effect on the non-bridging oxygens, $^{18}k_{NBO}$ = 0.994 ± 0.004 (27) (Table 3.1, Figure 3.5). Since the ^{18}O NBO-labeled substrate carries a diastereomeric mixture of labeled oxygen at each position (pro-R_p and pro-S_p), the $^{18}k_{NBO}$ observed here essentially represents the average KIE at each position. Strikingly, these isotope effects together suggest a highly dissociative transition state where bond fission between the scissile phosphate and leaving group exceeds nucleophilic attack

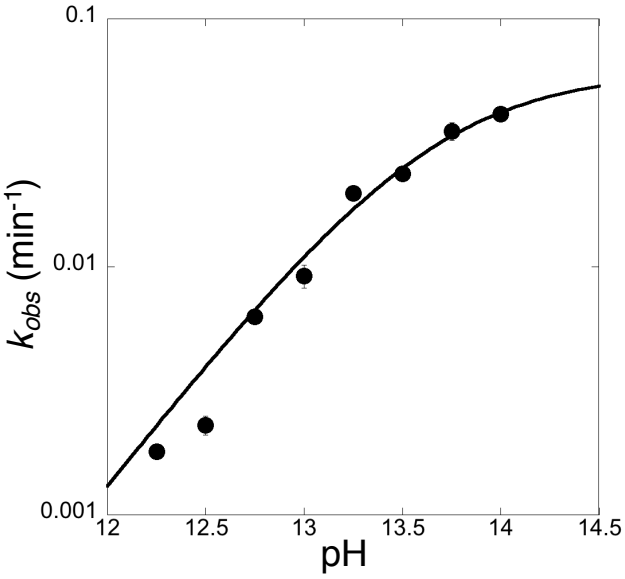

Figure 3.6 pH rate profile of UpG-like 11-mer substrate. Fitting to a model for a single ionization reveals a k_{cat} = 0.061±0.005 and a pK_a = 13.66±0.08 in good agreement with kinetic data for cleavage of UpG under similar conditions (Li and Breaker 1999, Harris et al. 2010).

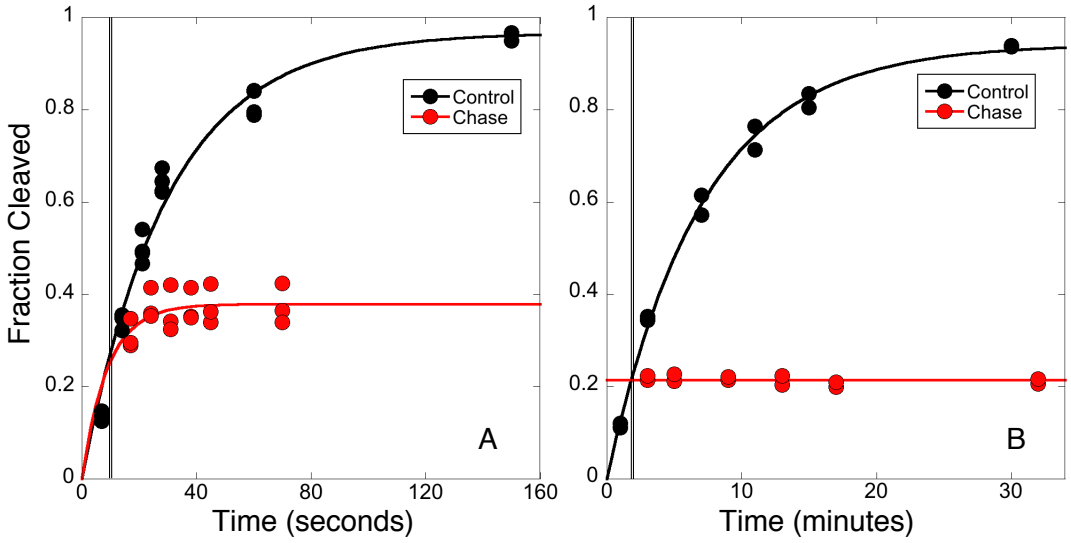

Figure 3.7 Pulse-Chase experiments for wild type (A) and SII (B) substrates. The time of the addition of the chase mixture is denoted with a double line (10 seconds for wild type and 2 minutes for SII). Curve fits of the chased reactions (red) show that essentially no substrate SII goes on to cleave after the addition of the chase mixture, while a substantial amount of wild type substrate goes on to cleave post-chase. These data reveal a forward commitment factor of 0.3 for the wild type substrate and ~0 for SII (C_f<0.02) (Shih and Been 2000).

3.4 Discussion

The moderate normal leaving group KIE suggests that the extent of leaving group departure is significant in the transition state. Fission of the (O5′)–P bond during phosphoryl transfer results in a loosening of the bonding environment around the leaving group, which makes a normal contribution to $^{18}k_{lg}$, so larger leaving group KIEs generally correspond to more dissociative transition states with significant (O5′)–P bond cleavage, whereas leaving group KIEs closer to unity indicate less leaving group departure. For instance, observation of $^{18}k_{lg}$ = 1.034 for UpG at pH = 14 has been interpreted as consistent with a very late transition state with almost complete fission of the (O5′)–P bond, and $^{18}k_{lg}$ = 1.006 for hydroxyl p-nitrophenyl phosphate (HpNPP) at pH = 10 corresponds to a transition state with minimal leaving group departure. Taken at face value, the intermediate $^{18}k_{lg}$ = 1.017 observed for HDV catalysis suggest an intermediate transition state.

However, proton inventories(Nakano, Chadalavada, and Bevilacqua 2000, Shih and Been 2001a) and Brønsted analysis(Perrotta, Wadkins, and Been 2006, Koo et al. 2015) of HDV ribozyme strongly suggest that proton transfer to the leaving group from C76 occurs in the chemical step. Therefore, the observed isotope effect likely includes an inverse contribution from the formation of the (O5′)–H bond. The observed $^{18}k_{lg}$, constitutes the product of contributions from (O5′)–P bond cleavage ($^{18}k_{lg,OP}$) and (O5′)–H bond formation ($^{18}k_{lg,OH}$) : ($^{18}k_{lg}$) = $^{18}k_{lg,OP}$• $^{18}k_{lg,OH.}$ Therefore, estimation of the amount of leaving group departure requires information regarding the extent of proton transfer and the magnitude of that contribution to the observed effect, which can be done making three very crude assumptions: 1) the equilibrium isotope effect (EIE) for protonation the 5′O-hydroxyl is about 0.976 (Gu et al. 2013a), 2) the contribution from protonation scales linearly with the extent of proton transfer and 3) the extent of proton transfer

in the HDV catalyzed transition state is 0.6 (Perrotta, Wadkins, and Been 2006, Koo et al. 2015) taken from Brønsted analysis. Making these three assumptions reveals that, accounting for the assumed contribution from proton transfer, the contribution to $^{18}k_{lg}$ from leaving group departure is *c.a.* 1.032, almost identical to the observed effect for the uncatalyzed reaction.

The large normal $^{18}k_{nuc}$ observed for HDV catalysis suggests a moderately dissociative transition state with respect to nucleophilic attack, but interpretation of this value is complicated by a number of factors. Since HDV ribozyme catalysis proceeds from a ground state with a protonated nucleophile(Lu et al. 2018), the apparent $^{18}k_{nuc}$ reports on contributions from bond formation between the nucleophile and scissile phosphate and deprotonation. The isotope effect from bond formation is itself constituted from two factors: the temperature-dependent factor (TDF) and temperature-independent factor (TIF) (Westaway et al. 1998). The TDF reflects changes to the bonding environment around the 2′O and should make an inverse contribution to the observed isotope effect formation of the (O2′)–P bond results in a stiffening of the bonding environment. The TIF, sometimes called the imaginary frequency ratio, reflects the extent to which the labeled atom participates in the reaction coordinate and always makes a normal contribution since the lighter isotope always has a larger imaginary frequency (Melander and Saunders 1987). Because the TDF and TIF make contributions in opposite directions and nucleophile isotope effects are the product of the TDF and TIF, the magnitude of the nucleophile KIE is largest for early transition states (where the normal contribution from the TIF dominates) and becomes more normal, or even inverse, for later transition states where bond formation increases the contribution from the TDF (Humphry et al. 2008). Therefore, assuming no contribution from deprotonation the large normal $^{18}k_{nuc}$ observed strongly suggests an early transition state with respect to (O2′)–P bond formation.

Deprotonation of the nucleophile also makes a normal contribution to the observed $^{18}k_{nuc}$ since loss of the (O2′)–H bond results in a loosening of the bonding environment. The EIE for hydroxyl p-nitrophenyl phosphate (HpNPP) was previous calculated PCM/ B3LYP/6-31+G(d,p) calculations(Humphry et al. 2008) to be 1.025, which provides a crude estimate for the contribution from complete deprotonation of a secondary alcohol. Assuming that the contribution from deprotonation for the HDV substrate is similar to the calculated EIE for HpNPP and that the proton transfer occurs in a pre-equilibrium step, the observed isotope effect can be corrected to report exclusively on contributions from bond formation revealing an effect near unity – $^{18}k_{nuc,bond} = 0.999$. This suggests offsetting contributions from a TIF and TDF approximately equal in magnitude and is comparable to $^{18}k_{nuc}$ near unity. Therefore, in a mechanism where proton transfer from the nucleophile occurs before the rate-limiting step, the observed $^{18}k_{nuc}$ corresponds to an early transition state with partial, but significant, formation of the (O2′)–P bond.

If the loss of the (O2′)–H bond and formation of the (O2′)–P bond are concerted, then the two aforementioned mechanistic interpretations serve as boundaries on a range of possible transition states consistent with the observed $^{18}k_{nuc}$. A concerted reaction with minimal proton transfer would have the highly dissociative transition state implied by the interpretation of $^{18}k_{nuc}$ that excludes proton transfer, and a concerted reaction with nearly complete proton transfer would have a transition state similar to the early transition state suggested by an interpretation of $^{18}k_{nuc}$ that assumes pre-equilibrium deprotonation. Two experiments help narrow this range: 1) proton inventories on HDV ribozyme under similar conditions(Nakano, Chadalavada, and Bevilacqua 2000, Shih and Been 2001a) show two protons in-flight suggesting that at least some deprotonation of the nucleophile has occurred by the rate-limiting step and 2) analysis of

fluorinated hydroxypropyl substrates with perturbed nucleophilicity suggest some development of negative charge on the nucleophile as it progresses from the ground state to the transition state(Weissman et al. 2015). Together these data suggest a significant contribution from proton loss, which makes a transition state with at least some (O2′)–P bond formation more likely.

Interpretation of the $^{18}k_{NBO}$ is complicated by the fact that the observed effect is an average of the intrinsic effect on each non-bridging oxygen. Therefore, the observed effect could result from a small inverse $^{18}k_{NBO}$ = 0.994 on each atom or from more inverse effect on one oxygen balanced by a more normal effect on the other. Although the non-bridging oxygens are not involved in any bond formation or fission events during phosphoryl transfer changes in isotope effects on these atoms can arise from an alteration of their bonding environment resulting from a change in hybridization, bond order or interactions with the active site. Inverse non-bridging isotope effects are generally consistent with a more dissociative transition states(Hengge 2002) and commonly observed for monoester transition states(Lassila, Zalatan, and Herschlag 2011).

The three isotope effects together argue for a dissociative, metaphosphate-like transition state. The normal isotope effect on the nucleophile is, in isolation, consistent with range of transition states. If the contribution from proton transfer is minimal, then the observed effect represents a very early transition state dominated by the TIF with minimal contributions from either (O2′)–P formation or (O2′)–H loss. However, if proton transfer makes a significant contribution to the observed effect (or is transferred in a pre-equilibrium step) then the observed effect likely corresponds to a more moderate transition state with partial (O2′)–P formation. The normal observed $^{18}k_{lg}$ combined with prior biochemical evidence indicating significant proton transfer to the leaving group suggest is late transition state with respect to leaving group

departure, and inverse effect observed on the non-bridging oxygens suggests a more dissociative reaction center. Together these data are consistent with a range of possible mechanisms, but argue for a transition state in which the extent of leaving group departure exceeds the extent of nucleophilic attack.

The uncatalyzed reaction is characterized by a large, inverse effect on the nucleophile ($^{18}k_{nuc}$ = 0.984) and a large normal effect on the leaving group ($^{18}k_{lg}$ = 1.034) consistent with a very late transition state with almost complete formation of the (O2′)–P and fission of the (O5′)–P. In striking contrast, our data suggest that the HDV catalyzed reaction progresses through a transition state that is both earlier and more dissociative. RNase A catalyzed cleavage of UpG shows a small inverse effect on the nucleophile ($^{18}k_{nuc}$ = 0.994) and a normal effect on the leaving group ($^{18}k_{lg}$ = 1.014) of comparable magnitude to HDV and an effect of unity on the non-bridging oxygens ($^{18}k_{NBO}$ = 1.001). These data were taken as evidence of a "late anionic" transition state with complete loss of (O2′)–H bond and advanced (O2′)–P bonding. The HDV reaction displays a more inverse effect on the non-bridging oxygens and a significantly more normal effect on the nucleophile suggestive of a transition state with much less advanced (O2′)–P bonding. Combined with the similarity of the effects observed on the leaving groups, comparison of the two reactions indicate that HDV progresses through a substantially earlier and more dissociative transition state than RNase A (Figure 3.8).

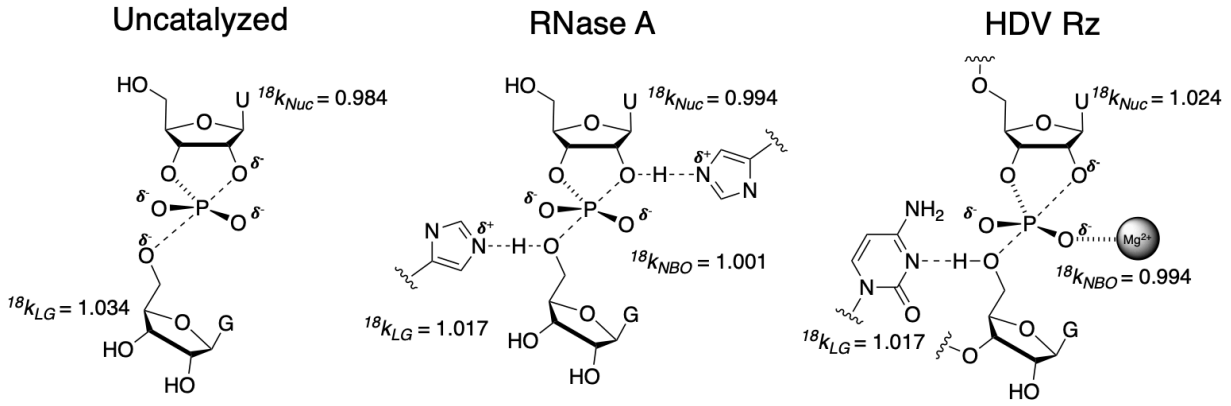

Figure 3.8. Comparison of transition states for 2′O-transphosphorylation. The uncatalyzed reaction is characterized by a large inverse $^{18}k_{nuc}$ and large normal $^{18}k_{lg}$ corresponding to a late transition state with significant (O2′)–P bond formation and (O5′)–P bond fission. The RNase A catalyzed reaction is characterized by a small inverse $^{18}k_{nuc}$, moderate normal $^{18}k_{lg}$ and a $^{18}k_{NBO}$ near unity also corresponding to a relatively late transition state. In contrast to the other two models, HDV A catalyzed reaction is characterized by a large normal $^{18}k_{nuc}$, moderate normal $^{18}k_{lg}$ and an inverse $^{18}k_{NBO}$ corresponding to an early transition state with significant (O5′)–P bond fission, but relatively little (O2′)–P bond formation.

At a fundamental level, enzymes enhance the rate of chemical reactions by selectively stabilizing chemical transition states, but when an energy landscape for a chemical reactions is characterized by large potential energy differences between relatively close – with respect to chemical structure – states, enzymes are unlikely to meaningfully alter reaction pathways and would be expected to evolutionarily converge toward active sites that support the transition states corresponding to energy minima. However, for reactions with "flat" energy landscapes characterized by relatively small potential energy differences between neighboring chemical states, enzyme catalysis can create new reaction pathways by stabilizing alternate chemical states. The observed differences in KIEs for RNase A, HDV, and uncatalyzed cleavage reactions argue for the latter possibility in phosphoryl transfer. The divergence of transition states suggested by KIE studies of these reactions suggests that phosphoryl transfer can proceed

through a range of viable transition states, and the conditions provided by enzyme active sites provide access to alternate reaction pathways compared to the uncatalyzed reaction. This insight argues against a view of ribozyme evolution framed by the notion that various classes of endonucleolytic ribozymes have converged towards an optimal mechanism of catalysis. Instead, the "flatness" of the phosphoryl transfer energy landscape makes formation of a useful ribozyme active site "easy" enabling formation of many classes of ribozymes from desperate evolutionary origins. Future studies that compare the transition states of various endonucleolytic ribozymes, particularly those that employ alternate catalytic strategies could help clarify this hypothesis.

Chapter 4: Conclusions

Phosphoryl transfer represents a ubiquitous reaction in nature (Westheimer 1987). Therefore, endonucleolytic ribozymes represent not only an interesting set of biochemical puzzles, but also powerful systems for the interrogation of a fundamental chemical transformation. Because of their tractable size and the relative ease with which RNA enzymes can be chemically manipulated relative to protein enzymes, ribozymes lend themselves as model systems for the study of 2′-transphosphorylation reactions. Additionally, the mechanistic enzymology of self-cleaving ribozymes can provide deeper insight into the general mechanisms by which RNA molecules act as catalysts in biology, which may aid the ongoing search for functional non-coding transcripts.

The mechanistic investigation of self-cleaving ribozymes presented in this thesis operates on two levels: 1) Investigation of the network of interactions that organize ribozyme active sites and contribute to catalysis and 2) Quantification of the extent to which catalytic interactions accelerate chemistry and characterization ribozyme transition states and reaction pathways. Most mechanistic investigations of endonucleolytic ribozymes focus on the first level of inquiry, since a foundational understanding of catalytic interactions is required for meaningful investigation of reaction pathways and transition states. However, as the field has matured over the past several decades, the time elapsed from the discovery of a novel ribozyme class to elucidation of its general catalytic mechanism has dramatically reduced. For instance, the discovery of the Twister ribozyme was first published in 2014 (Roth et al. 2014). The same year its crystal structure was solved and published (twice) (Eiler, Wang, and Steitz 2014, Liu et al. 2014), and the mechanism of Twister catalysis is largely settled only two years later(Wilson et al. 2016).

Therefore, deeper investigation into ribozyme mechanism requires inquiry of the second aforementioned level.

In this thesis, I present data that helps to bridge these two levels of inquiry. In chapter 2, I described the network of active site interactions that contribute to catalysis in VS ribozyme. That network includes a divalent metal ion previously unappreciated in the VS literature. Further, I presented Brønsted analysis for a series of purine analogs that clarified the roles for the catalytic nucleobases and quantified the extent of proton transfer in the reaction transition state. The interactions that organize the HDV ribozyme are relatively well-understood; however, significant ambiguity remains regarding the character of the reaction transition state. In chapter 3, I presented the first complete set of kinetic isotope effects for an endonucleolytic ribozyme, analysis of which provides information regarding the transition state structure.

A comparative schematic of the HDV and VS active sites is presented in Figures 2.11 and 3.2. In the HDV ribozyme active, a divalent metal ion, positioned by a critical G25:U20 wobble-pair, coordinates the *pro*R_p non-bridging oxygen of the scissile phosphate, which provides electrostatic stabilization to the negative charge developed on the phosphate throughout the reaction. A water or hydroxide bound to the catalytic metal ion activates the nucleophile through proton transfer, and C76 acts as a general acid stabilizing the leaving group through protonation. The exocyclic amine on the general acid, C76(N4), is important for catalysis (Das and Piccirilli 2005), but its function is not clearly defined. One possibility is that it interacts with a non-bridging oxygen on the scissile phosphate. Evidence for all of these interactions comes from prior work. In contrast, little was known about the network of interactions in the VS active site beyond the importance of the catalytic nucleobases A756 and G638. In this work, we provided evidence for the presence of a divalent metal ion coordinated by the *pro*S_p oxygen of the scissile

phosphate, the *proR*$_p$ oxygen of the downstream phosphate and G623(N7). Although the importance of G638 was well-appreciated, Brønsted analysis presented here directly implicates G638 in proton transfer to and mutation rescue suggests that its exocyclic amine interactions with the *proR*$_p$ oxygen of the scissile phosphate. Additionally, Brønsted analysis implicated A756 in proton transfer to the leaving group and mutational rescue suggests that A756(N6) interacts with the same non-bridging oxygen as G638(N2). Together, these data paint a picture of a well-ordered active site.

With respect to transition state structure, comparison of HDV and VS is problematic since data for VS comes from a combination of Brønsted analysis and computation whereas data for HDV comes from kinetic isotope effects; However, some meaningful conclusions can be drawn. Kinetic isotope effect analysis in HDV ribozyme argues for an early transition state with respect to (O2′)–P bond formation and a later transition state with respect to (O5′)–P bond cleavage. Together, these data imply a dissociative transition state for HDV ribozyme. At present, analogous data for VS catalysis do not exist, but careful examination of the extant Brønsted data provides clues about VS reaction pathway. Brønsted analysis indicates partial proton transfer to the leaving group advanced and proton transfer from the nucleophile in the transition state. The Brønsted coefficient obtained for a series of A analogs in VS ($\alpha \sim 0.2$) is low relative to the Brønsted coefficient obtained for a series of C analogs in HDV ($\alpha \sim 0.8$), suggesting that the extent of proton transfer to the leaving group is less advanced in VS than in HDV. If ribozymes minimize the developing negative charge on the leaving group through synchronous proton transfer and (O5′)–P bond cleavage then the low Brønsted coefficient observed for VS suggests an early transition state with respect to leaving group departure. The large Brønsted coefficient observed for a series of G analogs in VS ($\beta \sim 0.8$) suggests advanced

or even complete proton transfer from the nucleophile although it provides no information regarding the extent of (O2′)–P bond formation. The large normal isotope effect observed for the nucleophile in the HDV reactions is consistent with advanced proton transfer and an early transition state with respect to O2′)–P bond formation. Taken together, the data for VS and HDV suggest proton transfer is advanced for both.

As discussed in Chapter 3, the kinetic isotope effect analysis suggests that the transition state for the uncatalyzed reaction is much later, for both the nucleophile and leaving group, than for HDV catalyzed reaction. The low Brønsted coefficient for general acid analogs in VS ribozyme hints that VS also proceeds through a reaction pathway with an early transition state with respect to (O5′)–P bond cleavage although this conclusion is purely circumstantial since Brønsted analysis provides no direct information on (O5′)–P bond in the transition state. Together, these data are consistent with a model in which both HDV and VS catalysis proceeds through reaction pathways with transition states substantially earlier than uncatalyzed phosphoryl transfer, which suggests that ribozyme active sites can alter reaction pathways.

Currently, the most interesting space in the field of ribozymology focuses on the identification and characterization of novel functional RNAs. The biological function of these molecules remains poorly understood and the extent genealogical dispersion is unknown; however, bioinformatic methods can be useful in the identification of new functional transcripts. With respect to ribozyme mechanism, the relationship between transition states employed by various classes of endonucleolytic ribozyme is unclear. Full kinetic isotope effect analysis for each of the classes under similar conditions could provide an “apples to apples” comparison of transition states.

Kinetic isotope effects can also prove useful in deconvoluting catalytic and organizational active site interactions. Mutations that affect catalytic interactions should affect observed isotope effects, while mutations that only affect active site organization should not affect isotope effects. This is true because interactions that only contribute through organization effectively enhance rate by increasing the fraction of the ground state population in the activated form. Therefore, mutations that alter rate by reducing that fraction should have no effect on isotope effects. Conversely, kinetic isotope effects should be sensitive to mutations targeting catalytic interactions that affect the transition state, since they will alter the reaction pathway. Technical challenges have rendered isotope effect analysis impractical, but was methods improve in the coming years, this may prove to be a useful tool in mechanistic investigations.

Appendix A: Investigation of Nucleophile Activation in HDV Ribozyme

A.1 Introduction

The hepatitis delta virus (HDV) ribozyme serves as an outstanding model system for foundational studies of RNA catalysis due to its small size(Riccitelli and Luptak 2013), the availability of high-resolution crystal structures(Ke et al. 2004, Chen et al. 2010, Kapral et al. 2014) and wealth of biochemical and kinetic data(Shih and Been 2002). The RNA genome of the hepatitis delta virus encodes two forms of the HDV ribozyme, genomic and antigenomic, which mediate an essential step of viral replication by *cis*-cleavage(Sharmeen et al. 1988). Both forms of the ribozyme adopt similar overall structure, are likely to employ similar catalytic mechanisms and can be divided into *trans*-cleaving constructs though separation of 5′-terminus from the rest of the ribozyme. Like the other small endonucleolytic ribozymes, the HDV ribozyme facilitates cleavage by catalyzing the nucleophilic attack of the 2′ hydroxyl on the adjacent phosphate to form a 2′, 3′-cyclic phosphate and 5′-hydroxyl termini (Figure 1.1).

A significant body of functional(Nakano, Chadalavada, and Bevilacqua 2000, Nakano and Bevilacqua 2001, Das and Piccirilli 2005, Cerrone-Szakal et al. 2008), spectroscopic (Gong et al. 2007, Chen et al. 2009), and crystallographic(Ke et al. 2004, Chen et al. 2010, Kapral et al. 2014) data support the role of C76 in the antigenomic form as a general acid that stabilizes the leaving group through proton transfer. Perhaps the strongest evidence was generated through observation of C76 mutants with substrates containing a 5′-bridging phosphorothioate at the cleavage site(Das and Piccirilli 2005). In the 5′-phosphorothioate background, activation of the leaving group is not required for cleavage because of the highly labile thiolate leaving group,

therefore, the insensitivity of the phosphorothioate to C76 mutation provides evidence for the leaving group activation by the mutated group. Subsequently, similar experiments have been employed to interrogate leaving group activation in other ribozymes (Thomas and Perrin 2009, Wilson et al. 2010, Kath-Schorr et al. 2012). However, an analogous experimental approach to investigate nucleophile activation has remained elusive since no chemical system with a pre-activated nucleophile has been devised.

Consequently, nucleophilic activation arguably represents the least understood feature of ribozyme (and enzyme) catalysis (Anderson, Ruszczycky, and Harris 2006). Phosphoryl transfer to oxygen nucleophiles shows a strong dependence on the nucleophile pK_a (Oivanen, Kuusela, and Lonnberg 1998, Ye et al. 2007), which suggests that reactivity is highly sensitive to the protonation state of the nucleophile. Ground state interactions with metal ions, hydrogen bond donors, or solvent can also influence reactivity (Mikkola et al. 1999). In HDV ribozyme, the mechanism of nucleophile activation remains poorly understood. However, crystallographic(Chen et al. 2010) and biochemical(Chen et al. 2013, Thaplyal et al. 2013) data are consistent with a well-positioned magnesium ion with inner-sphere coordination to the pro-R_p oxygen of the scissile phosphate, which could play a role in nucleophile activation(Nakano, Chadalavada, and Bevilacqua 2000)

The features of nucleophile activation have profound significance for understanding catalysis, yet limited strategies exist to probe nucleophile function. Analogous to substrates with leaving group modifications, a series of substrates that perturb the nucleophilic 2′-hydroxyl group might provide a complementary strategy to investigate catalytic mechanism, e.g. identify charge development on the nucleophilic oxygen through the transition state, estimate the degree of bonding to the nucleophile in the transition state, and identify possible interaction partners

with the nucleophile. In particular, we aimed to develop substrates that differ in nucleophilicity and basicity from the hydroxyl group in the native ribozyme and uncover ribozyme modifications whose effects on catalysis are suppressed or enhanced in the presence of these mutant substrates. Optimally, these substrates should maintain the 2´-hydroxyl group, but modulate its basicity of that group via inductive effects.

A series of oligonucleotides containing modifications (R: CH_3, CH_2F, CHF_2, CF_3, and wild-type [H]) at the 2′-β-position of the ribose ring were developed previously in our laboratory to perturb the pK_a and nucleophilicity of the 2′-hydroxyl group (Ye et al. 2007); Brønsted analysis of these substrates in non-enzymatic, hydroxide-catalyzed cleavage reactions yield an apparent β_{nuc} value of -0.75, indicating a significant degree of bonding to the nucleophile in the transition state, consistent with recent results from kinetic isotope effect analysis(Harris et al. 2010). However, introduction of these modified nucleotides into HDV ribozyme substrates blocked cleavage, presumably because the ribozyme active site could not accommodate substituents at the 2′-β-position, thereby precluding efforts to understand similarities and differences in nucleophile bonding between solution and ribozyme-catalyzed reactions. Since the HDV ribozyme has no strict sequence requirements upstream of the cleavage site (Perrotta and Been 1990, Kellerman et al. 2015, Shih and Been 2001b), we anticipated that the ribozyme might catalyze cleavage of substrates lacking a nitrogenous base and/or the ribose ring at the cleavage site. Thus, we considered the use of pK_a-perturbing modifications in the context of substrates possessing greater flexibility and occupying less volume at the cleavage site relative to natural nucleotides. Specifically, we were inspired by 2-(hydroxylproyl)aryl phosphate model compounds (herein tethered to oligonucleotides to generate “tethered substrates”) initially developed over 50 years ago (Brown and Usher 1965). Here we report the incorporation of 1,2-

propanediol, 3-fluoro-1,2-propanediol and 3,3,3-trifluoro-1,2-propanediol into the 5′-terminus of DNA and RNA oligonucleotides and the analysis of their hydroxide-catalyzed and HDV-ribozyme catalyzed cleavage reactions, respectively.

A.2 Methods

*Synthesis of phosphoramidites (**4a-c**)*

All reactions were carried out in anhydrous solvents under a positive pressure of Argon. Commercially available reagents and anhydrous solvents were used without further purification. ^{1}H, ^{13}C, ^{19}F and ^{31}P NMR spectra were recorded on a Bruker 500 or Bruker 400 MHz NMR spectrometer. ^{1}H chemical shifts are reported in δ (ppm) relative to tetramethylsilane and ^{13}C chemical shifts δ (ppm) relative to the solvent used. High resolution mass spectra were obtained from the Department of Chemistry, University of California at Riverside.

1,2-Bis(tert-butyldimethylsiloxy)propane (2a). 1*H*-imidazole (1.97 g, 29.0 mmol) and *t*-$BuMe_2SiCl$ (4.22 g, 28.0 mmol) were added to a solution of **1a** (0.76 g, 10.0 mmol) in dry DMF (10 mL). The mixture was stirred overnight at room temperature, then evaporated to a syrup under vacuum. The residue was partitioned between CH_2Cl_2 and H_2O, the organic layer was washed with water followed by brine, and dried over anhydrous Na_2SO_4. The sodium sulfate removed by filtration and the solvent was subsequently removed under vacuum. The residue was purified by silica gel chromatography, eluting with 2% ethyl acetate in hexane, to give product **2a** as an oil: 2.90 g (95% yield). ^{1}H NMR ($CDCl_3$) ẟ 3.80 (m, 1H), 3.52 (m, 1H), 3.33 (m, 1H), 1.11 (d, 3H, J = 6.1 Hz), 0.90 (s, 9H), 0.89 (s, 9H), 0.07 (s, 3H), 0.06 (s, 3H), 0.05 (s, 3H), 0.04 (s, 3H); ^{13}C NMR ($CDCl_3$) ẟ 69.6, 69.2, 26.2, 26.1, 20.8, 18.6, 18.4, -4.4, -4.6, -5.1, -5.2. HRMS (FAB^+): m/z calc for $C_{15}H_{37}O_2Si_2$, $[M+H^+]$: 305.2332; found: 305.2325.

1,2-Bis(tert-butyldimethylsiloxy)-3-fluoropropane (2b). Compound **2b** was prepared from **1b** (1.00 g, 10.6 mmol), 1*H*-imidazole (2.95 g, 30.7 mmol), and *t*-$BuMe_2SiCl$ (4.48 g, 29.7 mmol) as described for **2a**. Silica gel chromatography (2% ethyl acetate in hexane) of the residue yielded 3.09 g (90% yield) of **2b** as an oil. ^1H NMR ($CDCl_3$) ϐ 4.18-4.46 (m, 2H), 3.79-3.88 (m, 1H), 3.44-3.53 (m, 1H), 0.82 (s, 9H), 0.81 (s, 9H), 0.02 (s, 3H), 0.01 (s, 3H), -0.02 (s, 6H); ^{13}C NMR ($CDCl_3$) ϐ 85.9, 84.2, 72.4, 72.2, 63.9, 63.8, 26.0, 25.9, 18.4, 18.3, -4.7, -5.30, -5.36, -5.4, ^{19}F NMR ($CDCl_3$) ϐ -109 (t). HRMS (FAB^+): m/z calc for $C_{15}H_{36}FO_2Si_2$, $[M+H^+]$: 323.2238; found: 323.2238.

*1,2-Bis(tert-butyldimethylsiloxy)-3,3,3-trifluoropropane (2c)***.** Compound **2c** was prepared from **1c** (1.00 g, 7.7 mmol), 1*H*-imidazole (1.52 g, 22.3 mmol), and *t*-$BuMe_2SiCl$ (3.25 g, 21.5 mmol) as described for **2a**. Silica gel chromatography (2% ethyl acetate in hexane) of the residue yielded 1.99 g (72% yield) of **2c** as an oil. ^1H NMR ($CDCl_3$) ϐ 3.97-4.03 (m, 1H), 3.81-3.84 (m, 1H), 3.63-3.66 (m, 1H), 0.91 (s, 9H), 0.90 (s, 9H), 0.12 (s, 3H), 0.11 (s, 3H), 0.072 (s, 3H), 0.071 (s, 3H); ^{13}C NMR ($CDCl_3$) ϐ 124.6.0 (q), 73.0 (q), 63.3, 26.0, 25.7, 18.5, 18.2, -4.6, -5.2, -5.4, -5.5, ^{19}F NMR ($CDCl_3$) ϐ -77.6 (d). HRMS (FAB^+): m/z calc for $C_{15}H_{34}F_3O_2Si_2$, $[M+H^+]$: 359.2049; found: 359.2044.

*2-tert-Butyldimethylsiloxy-1-propanol (3a)***.** HF·pyridine (890 μL, 6.84 mmol; Aldrich) was carefully diluted with pyridine (1.0 mL) and then added dropwise to a solution of **2a** (1.53 g, 5.02 mmol) in THF (10 mL). After overnight stirring at room temperature, thin-layer chromatography of the mixture showed that no remaining starting material. The mixture was partitioned between CH_2Cl_2 and H_2O; the organic layer was washed with 5% aq. $NaHCO_3$ followed by brine and dried over anhydrous Na_2SO_4. The sodium sulfate removed by filtration and the solvent was subsequently removed under vacuum. The residue was purified by silica gel

chromatography, eluting with 17% ethyl acetate in hexane, to give product **3a** as an oil: 516 mg (54% yield). ^{1}H NMR ($CDCl_3$) δ 3.91 (m, 1H), 3.49 (m, 1H), 3.37 (m, 1H), 2.02 (m, 1H), 1.12 (d, 3H, J = 6.2 Hz), 0.91 (s, 9H), 0.09 (s, 6H); ^{13}C NMR ($CDCl_3$) δ 69.2, 68.3, 25.9, 19.9, 18.2, -4.3, -4.7. HRMS (FAB^+): m/z calc for $C_9H_{23}O_2Si$, [$M+H^+$]: 191.1467; found: 191.1467.

2-tert-Butyldimethylsiloxy-3-fluoro-1-propanol (3b). Compound **3b** was prepared from **2b** (2.89 g, 8.96 mmol) and HF·pyridine (1.20 mL, 9.21 mmol) as described for **3a**. Silica gel chromatography (10% ethyl acetate in hexane) of the residue yielded 0.99 g (53% yield) of **3b** as an oil. ^{1}H NMR ($CDCl_3$) δ 4.28-4.47 (m, 2H), 3.95-4.00 (m, 1H), 3.56-3.67 (m, 1H), 0.92 (s, 9H), 0.11 (s, 6H); ^{13}C NMR ($CDCl_3$) δ 84.6, 83.3, 71.4, 71.3, 63.3, 63.2, 25.9, 18.2, -4.6, -4.8; ^{19}F NMR ($CDCl_3$) δ -106. HRMS (FAB^+): m/z calc for $C_9H_{22}FO_2Si$, [$M+H^+$]: 209.1373; found: 209.1367.

2-(tert-Butyldimethylsiloxy)propyl cyanoethyl N,N-diisopropylphosphoramidite (4a). To a solution of **3a** (441 mg, 2.16 mmol) in dry dichloromethane (5 mL) under argon were added *N*,*N*-diisopropylethylamine (1.85 mL, 10.75 mmol), 2-cyanoethyl *N*,*N*-diisopropylchlorophosphoramidite (1.00 g, 4.23 mmol), and 1-methylimidazole (173 μL, 0.136 mmol). After 1 hour stirring at room temperature, thin-layer chromatography of the mixture showed that no remaining starting material. The reaction mixture was then quenched with MeOH (1 mL) and stirred for an additional 5 minutes. After the solvent was removed under vacuum, the residue was purified by silica gel chromatography, eluting with 5% ethyl acetate in hexane containing 0.5% triethylamine, to give the corresponding phosphoramidite **4a** as an oil: 689 mg (82% yield): ^{31}P NMR (CD_3CN) δ 150.8, 150.3. HRMS (FAB^+): m/z calc for $C_{18}H_{40}N_2O_3SiP$, [$M+H^+$]: 391.2546; found: 391.2551.

2-tert-Butyldimethylsiloxy-3-fluoropropyl cyanoethyl N,N-diisopropylphosphoramidite (4b). Compound **4b** was prepared from **3b** (441 mg, 2.12 mmol), *N*,*N*-diisopropylethylamine (2.29 mL, 13.31 mmol), 2-cyanoethyl *N*,*N*-diisopropylchlorophosphoramidite (1.00 g, 4.23 mmol), and 1-methylimidazole (200 μL, 0.157 mmol) as described for **4a**. Silica gel chromatography (5% ethyl acetate in hexane containing 0.5% triethylamine) purification of the residue yielded 625 mg (72% yield) of **4b** as an oil. ^{31}P NMR (CD_3CN) δ 151.9, 151.4; ^{19}F NMR ($CDCl_3$) δ -107.7 (d), 108.5 (d). HRMS (FAB^+): m/z calc for $C_{18}H_{39}N_2O_3FSiP$, $[M+H^+]$: 409.2452; found: 409.2454.

2-tert-Butyldimethylsiloxy-3,3,3-trifluoropropyl cyanoethyl N,N-diisopropylphosphoramidite (4c). 2-*tert*-Butyldimethylsiloxy-3,3,3-trifluoro-1-propanol (**3c**) was prepared from **2c** (1.81 g, 5.04 mmol) and HF·pyridine (680 μL, 5.18 mmol) as described for **3a**. Silica gel chromatography (10% ethyl acetate in hexane) of the residue yielded 441 mg (36% yield) of **3c** as an oil. ^{1}H NMR ($CDCl_3$) 4.03-4.07 (m, 1H), 3.77-3.81 (m, 1H), 3.70-3.75 (m, 1H), 0.93 (s, 9H), 0.15 (s, 6H); ^{13}C NMR ($CDCl_3$) 124.4 (q), 71.8 (q), 61.9, 25.6, 18.2, -4.9, -5.2; ^{19}F NMR ($CDCl_3$) -77.4 (d). Compound **4c** was then prepared from **3c** (387 mg, 1.58 mmol), *N*,*N*-diisopropylethylamine (1.71 mL, 9.94 mmol), 2-cyanoethyl *N*,*N*-diisopropylchlorophosphoramidite (1.0 g, 4.23 mmol), and 1-methylimidazole (160 μL, 0.126 mmol) as described for **4a**. Silica gel chromatography (5% ethyl acetate in hexane containing 0.5% triethylamine) purification of the residue yielded 590 mg (84% yield) of **4c** as an oil. ^{31}P NMR (CD_3CN) δ 152.3, 151.5; ^{19}F NMR ($CDCl_3$) δ -77.6 (t). HRMS (FAB^+): m/z calc for $C_{18}H_{37}N_2O_3F_3SiP$, $[M+H^+]$: 445.2263; found: 445.2262.

Experiments with substrates that perturb the 2′-hydroxyl nucleophile pKa to study nucleophile activation by the HDV ribozyme

RNA substrates were 3′-end radiolabeled as follows: 10 pmol RNA was incubated with 10 pmol 5′-^{32}P-pCp (cytidine 3′,5′-bisphosphate), 6 μM ATP, 1x RNA ligase buffer, 3.3 mM DTT, 1 μL DMSO, and 20 U T4 RNA ligase in a 10 μL reaction volume at 4 °C overnight. The reaction was then quenched by the addition of 8 μL stop solution (95% formamide, 15mM EDTA, 0.01% w/v bromophenol blue and xylene cyanol), gel purified on a 20% denaturing polyacrylamide gel, eluted into 1 mL TE overnight, and finally ethanol precipitated with glycogen as a carrier.

DNA substrates were 3′-end radiolabeled as follows: 10 pmol DNA was incubated with 10 pmol α-^{32}P-ddATP (dideoxyadenosine triphosphate), 5 μg BSA, 1x TdT (terminal deoxytransferase) buffer, and 15 U TdT in a 10 μL reaction volume at 37 °C for 1 hr. The reaction was then quenched by the addition of 8 μL stop solution, gel purified on a 20% denaturing polyacrylamide gel, eluted into 1 mL TE overnight, and finally ethanol precipitated with glycogen as a carrier.

To measure the rate of base-catalyzed cleavage of DNA substrates, the following high-pH reaction conditions were employed: 19.5 μL reaction buffer at the appropriate pH was added to 0.5 uL 3′-end radiolabeled substrate and incubated at 25 °C. At pH values between 12.0 and 14.6, reaction buffer was made by mixing KOH (3.90 M, pH 14.59) and KCl (3.90 M) solutions to achieve the desired pH. Reaction aliquots of 1 μL were removed at appropriate time-points, quenched by adding 6 μL 1 M Tris-HCl pH 7.5 (final pH's of quenched reaction aliquots are typically no higher than 8) with 7 μL stop solution, and rapidly chilled on dry ice. Hydrolysis products were separated from unhydrolyzed substrate on a denaturing 20% polyacrylamide / 7M

urea gel and quantified using a PhosphorImager with ImageQuant software (Molecular Dynamics). Data for cleavage reactions was fit to the equation $y = 1 - y_o - Ae^{-k_{obs}t}$ using Origin 7.0 (OriginLab), where k_{obs} is the first-order rate constant for substrate cleavage, and A is the extent of substrate cleavage; for reactions that did not reach completion (>80% reacted) after more than 20 days (reaction rate < 3 x 10^{-5} min^{-1}), data were fit assuming A = 0.8 to obtain k_{obs}. The reaction pK_a was determined by fitting reaction rate data to the equation $k = \frac{k_{max}}{1+10^{pKa-pH}}$.

HDV ribozyme-catalyzed reactions were conducted as previously described (Das and Piccirilli 2005). Briefly, ribozyme (final concentration 1 μM) was preincubated with 10 mM $MgCl_2$ at 70 °C for 2 min, then 25 °C for 14 min; buffer was added, and reaction was initiated by the addition of trace radiolabeled substrate (10 μL reaction volume). Buffers used contained 25 mM acetic acid, 25 mM MES, and 50 mM Tris (pH 4.0-8.0), or 50 mM MES, 25 mM Tris, and 25 mM 2-amino-2-methyl-1-propanol (pH 7.5-10.0). Reaction aliquots were removed at appropriate times, quenched by addition 9uL stop solution, and rapidly chilled on dry ice. Cleavage products were separated from uncleaved substrate on a denaturing 20% polyacrylamide / 7M urea gel and quantified using a PhosphorImager with ImageQuant software (Molecular Dynamics). Data for cleavage reactions was fit to the equation $y = 1 - y_o - Ae^{-k_{obs}t}$ using Origin 7.0 (OriginLab), where k_{obs} is the first-order rate constant for substrate cleavage, and A is the extent of substrate cleavage. Reaction pK_a´s (pK_{a1}, pK_{a2}) were determined by fitting reaction rate data to the equation $k = \frac{k_{max}}{1+10^{pH-pKa1}+10^{pKa2-pH}+10^{pKa2-pKa1}}$.

A.3 Results and Discussion

*1. Synthesis and incorporation of phosphoramidites (**4a-c**) into RNA/DNA substrates*

Commercially available, racemic 1,2-propanediol (**1a**), 3-fluoro-1,2-propanediol (**1b**) and 3,3,3-trifluoro-1,2-propanediol (**1c**) were converted into the corresponding phosphoramidites (**4a-c**) in three steps, as shown in Figure A.1. Both primary and secondary hydroxyl groups of **1** were first protected as *tert*-butyldimethylsilyl (TBS) ethers in 72-95% yield. The primary TBS ethers were selectively cleaved using HF-Pyridine complex to give alcohols **3a-c** in 36-54% yield. Phosphitylation of **3a-c** with 2-cyanoethyl *N,N*-diisopropylchlorophosphoramidite gave phosphoramidites (**4a-c**) in good yields (72-84%). All phosphoramidites were prepared as racemic mixtures with the exception of the 1,2-propanediol derivative which was prepared as both a racemic mixture and a enantiopure *S* isomer. Ribozyme-catalyzed-cleavage assays showed that both enatiopure and racemic versions of the resulting oligonucleotides display identical kinetic behavior (data not shown). All subsequent assays were performed with oligomers derived from racemic phosphoramidites.

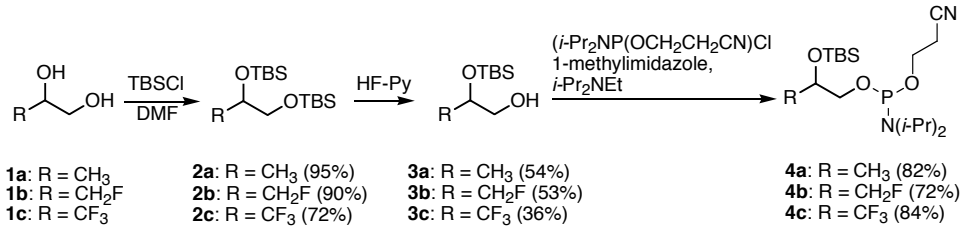

Figure A.1 Synthesis of propanediol phosphoramidites from corresponding diols.

To investigate non-enzymatic base-catalyzed cleavage of these modified linkages, we incorporated the phosphoramidites (**4a-c**) into DNA oligonucleotides (5′-**X**gg gtc ggc-3′). To investigate HDV ribozyme-catalyzed cleavage of these linkages, we incorporated **4a-c** into RNA

oligonucleotides (5′-**X**GG GUC GGC-3′). We used a modified 1-μmole RNA protocol with double coupling of the phosphoramidites (**4a-c)** (~75 mg) in anhydrous acetonitrile (0.75 mL). After the synthesis, the solid support was treated with a 3:1 (v/v) mixture of concentrated aqueous ammonium hydroxide and ethanol at 55 °C for 4 hours and then desilylated with triethylamine trifluoride complex at 65 °C for 25 min (Wincott et al. 1995). We purified the oligonucleotides on a denaturing polyacrylamide gel and confirmed their identities by MALDI-TOF MS (Table A.1).

	RNA Oligonucleotides			DNA Oligonucleotides		
	R: CF_3	R: CFH_2	R: CH_3	R: CF_3	R: CFH_2	CH_3
Calcd. Mass	2770.5	2734.5	2716.5	2656.4	2620.4	2602.4
MALDI Mass	2771.4[a]	2734.7 [a]	2716.1 [a]	2657.1[a]	2621.5[a]	2603.3[a]

Table A.1 Mass of propanediol substrates by mass spectroscopy. RNA oligonucleotides have the sequence 5′-XGGGUCGGC-3′and DNA oligonucleotides have the sequence 5′-Xgggtcggc-3′ where X is RCH(OH)CH2OPO(OH)O^-. a positive (M^+H^+)

Base-catalyzed cleavage of tethered DNA oligonucleotides

Under alkaline conditions, the 5′-propanediol phosphate tethers [5′-Xgg gtc ggc-3′; X: $RCH(OH)CH_2OPO(OH)O$-5′; R: CH_3, CH_2F, CF_3] release themselves from DNA via intramolecular transphosphorylation to the neighboring hydroxyl group, analogous to alkaline cleavage of RNA by 2′-*O*-transphosphorlyation (Figure A.1B). To assess the effect of increasing fluorine substitution on reactivity of the nucleophilic hydroxyl group, we observed the rate of tether release over a range of pH's (25 °C, KCl 3.90 M, pH 12.0 to 14.6; Table A.2, Figure A.2). Our expectation was that the inductive effects from fluorination would reduce both the nucleophilicity and the pK_a of the 2′ hydroxyl nucleophile, causing the fluorinated substrates to react more slowly at pH values above pK_a, when the substrates react from an oxyanionic ground

state, but react with a similar – or even enhanced – rate at pH values below the pK_a. For comparison, ethanol and trifluoroethanol, primary alcohols that have a $-CH_3$ or $-CF_3$ group geminal to the hydroxyl group, respectively, ionize with pK_a values of 15.2 and 13.2, respectively (Mock and Zhang 1990). Indeed, at the highest pH tested (pH 14.6), the methyl (R: CH_3) releases itself from the tether about 10-fold faster than the trifluoromethyl (R: CF_3) substrate. At pH 13, the two substrates react similar rates, and at low pH values the trifluoromethyl substrate reacts somewhat faster than its methyl counterpart; however, we emphasize that observations for reactions occurring below pH 13 should be interpreted with caution as they correspond to rates with half-lives on the order of weeks and are thus subject to more significant errors than faster reactions. Together, these observations suggest that the electron-withdrawing effect of fluorination reduces both the pK_a and the intrinsic rate of reaction. Fitting of these data to a single-ionization model suggests a $\Delta pK_a \sim 1$ from the methyl substrate ($pK_a = 14.5$) to the trifluoromethyl substrate ($pK_a = 13.5$). Given a $\Delta pK_a \sim 1$ between the two substrates, comparison of the maximal, observed rates offers a crude estimate of the Brønsted coefficient for charge development on the nucleophile ($\beta_{nuc} \sim 1$), consistent with the value of ~0.75 measured previously (Ye et al. 2007).

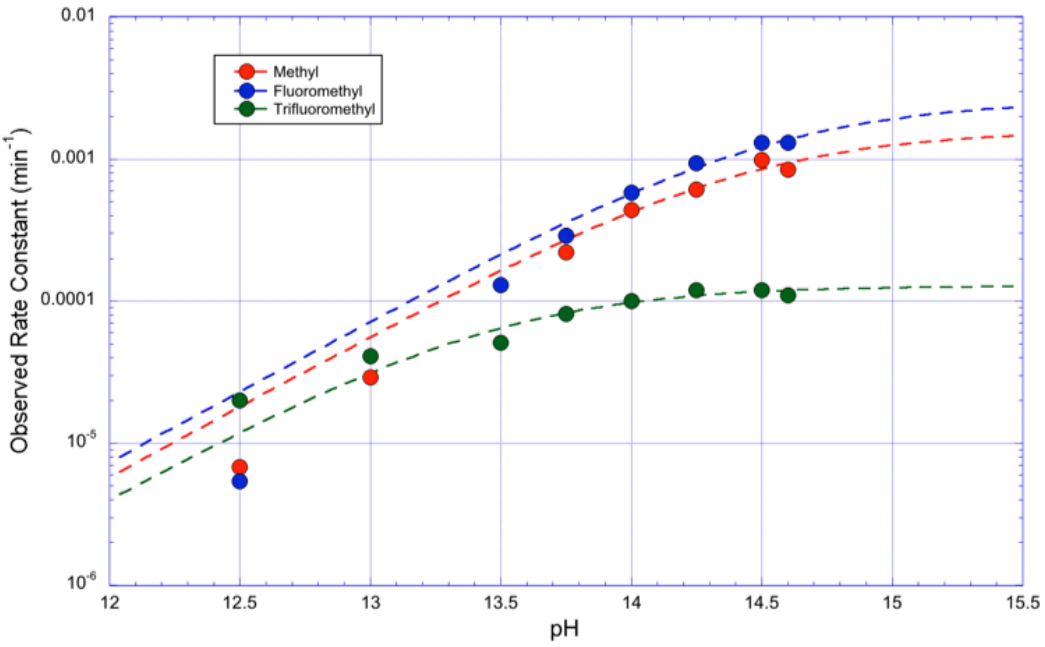

Figure A.2 pH-rate profile for base-catalyzed solution cleavage of DNA propanediol substrates. The reaction pK_a was determined by fitting reaction rate data to a model for single ionization (See methods). Fitting shows a $k_{max} = (1.7 \pm 0.4) \times 10^{-3}$ and $pK_a = 14.5 \pm 0.2$ for the R = CH_3 substrate, $k_{max} = (2.7 \pm 0.6) \times 10^{-3}$ and $pK_a = 14.6 \pm 0.1$ for the R = CH_2F substrate, and $k_{max} = (1.3 \pm 0.1) \times 10^{-4}$ and $pK_a = 13.5 \pm 0.1$ for the R = CF_3 substrate.

pH	R: CH_3	R: CF_3	
	rate (min^{-1})	rate (min^{-1})	k_{rel}
14.6	$(8.4 \pm 0.2) \times 10^{-4}$	$(1.1 \pm 0.4) \times 10^{-4}$	0.1
14.0	$(3.7 \pm 0.5) \times 10^{-4}$	$(1.0 \pm 0.2) \times 10^{-4}$	0.3
13.5	$(1.3 \pm 0.4) \times 10^{-4}$	$(5.0 \pm 0.3) \times 10^{-5}$	0.4
13.0	$(5.0 \pm 3.0) \times 10^{-5}$	$(4.0 \pm 2.0) \times 10^{-5}$	0.8

Table A.2 Rates for uncatalyzed tether release under basic conditions. Relative rates compared to the R: CH_3 substrate at the given pH

The monofluoromethyl substrate (R: CH_2F) reacted at rates and with apparent pK_a similar to the methyl substrate, suggesting minimal perturbation from the single fluorine substitution (Figure A.2). However, based upon our prior experience synthesizing an analogous β-branched ribonucleotide (Dai and Piccirilli 2003), the monofluoromethyl substrate may release itself through a more complex mechanism. Possibly, the oxyanion initially attacks the vicinal carbon to displace fluoride, generating the corresponding epoxide. Subsequent base-catalyzed opening of the epoxide would result in conversion to a glycerol tether which could undergo release to form product by attack at the phosphorous (Figure A.3). Formation of the glycerol tether could account for the modestly higher reactivity of the monofluoromethyl substrate relative to the methyl substrate at high pH values. Further work is necessary to determine whether this alternative pathway occurs; therefore, our subsequent analysis largely focuses on the methyl and trifluoromethyl substrates, which likely follow a simpler reaction path. We do not expect this alternative mechanism to be operative in the ribozyme catalyzed reaction where the pH is closer to neutrality.

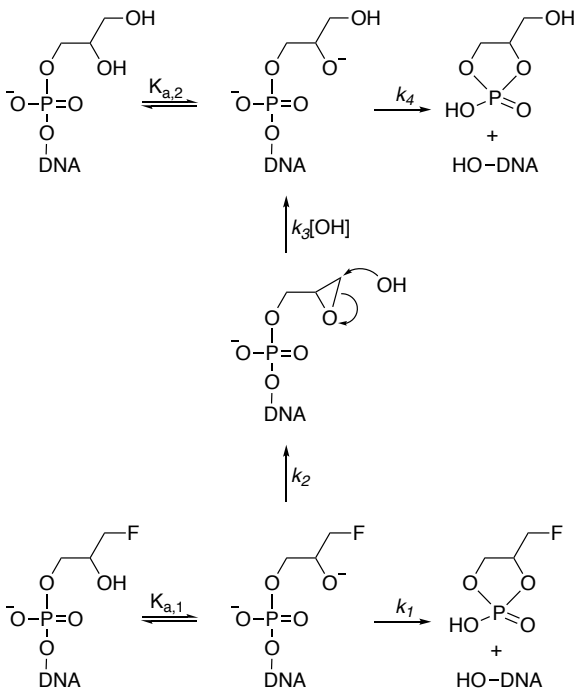

Figure A.3 Proposed mechanism of cleavage by monoflouromethylpropanediol tethered DNA oligonucleotide under alkaline conditions.

For comparison with the tethered substrates, we also determined the relationship between pH and rate for DNA oligonucleotides containing either a uridine or abasic residue upstream of the cleavage side under alkaline conditions. The 2′-hydroxyl of the uridine substrate ionized with pK_a ~13.5 and exhibited a maximum cleavage rate of 0.090 min^{-1}, consistent with previous observations(Li and Breaker 1999). The abasic ribose ionized with a higher pK_a, ~14.5 and maximal rate of 0.84 min^{-1} – about ten-fold faster than uridine – presumably reflecting the electron-withdrawing effect of uracil heterocycle versus a hydrogen atom at the 1′ position (Figure A.4). Compared to the cleavage rate of the abasic ribose under similar conditions, the methyl-tethered (R: CH_3) substrate, which should have a comparably nucleophilic 2′-hydroxyl, reacts about 500-fold slower (Table A.4), reflecting the structural preorganization imparted by the ribose ring. This comparison suggests that conformational restriction around the C2′-C3′

bond, which is freely rotatable in the tethered substrates but restricted in the ribofuranosyl context, imparts a rate enhancement of two to three orders of magnitude.

HDV ribozyme-catalyzed cleavage of RNA oligonucleotides

Next, we tested the tethered RNA oligonucleotides (5′-XGG GUC GGC-3′; X: $RCH(OH)CH_2OPO(OH)O5'$-; R: CH_3, CH_2F, CF_3) as substrates for HDV ribozyme-catalyzed cleavage at various pH values. To ensure that differences in reactivity between tethered and ribonucleotide substrates arose from differences in the cleavage step rather than substrate binding, we examined rate as a function of ribozyme concentration. The rate was insensitive to ribozyme concentration over the range of 50-2000 nM. . These data set an upper limit of 100 nM for K_m and suggest that at the ribozyme concentrations employed in our subsequent experiments (1000nM) the reaction proceeds exclusively from a bound ES complex ground-state for both substrates (Figure A.5).

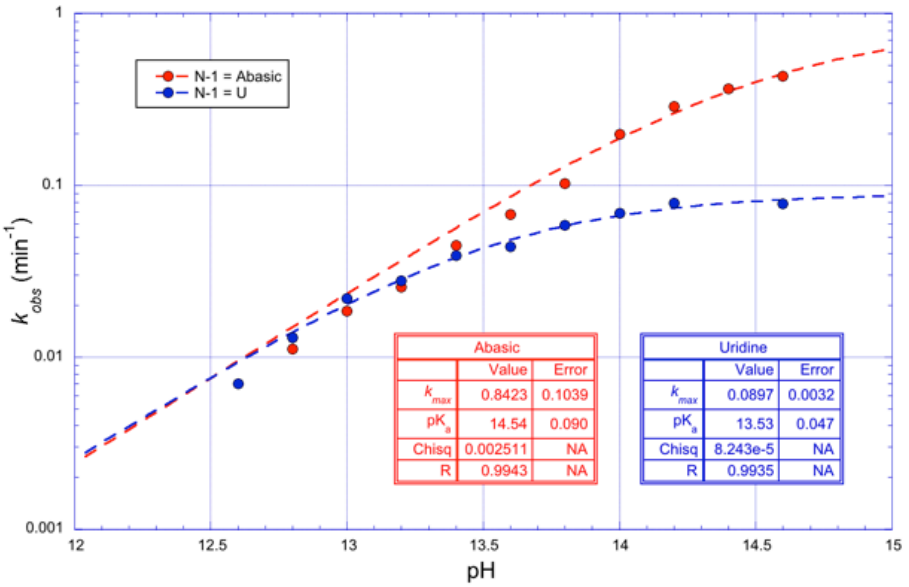

Figure A.4 pH-rate profile for base-catalyzed solution cleavage of DNA substrates. Both oligonucleotides had the sequence 5′-UUNGGUCGGC-3′ where N was either U or an abasic ribose (1′ hydrogen). Data were fit to a model for single ionization (see methods).

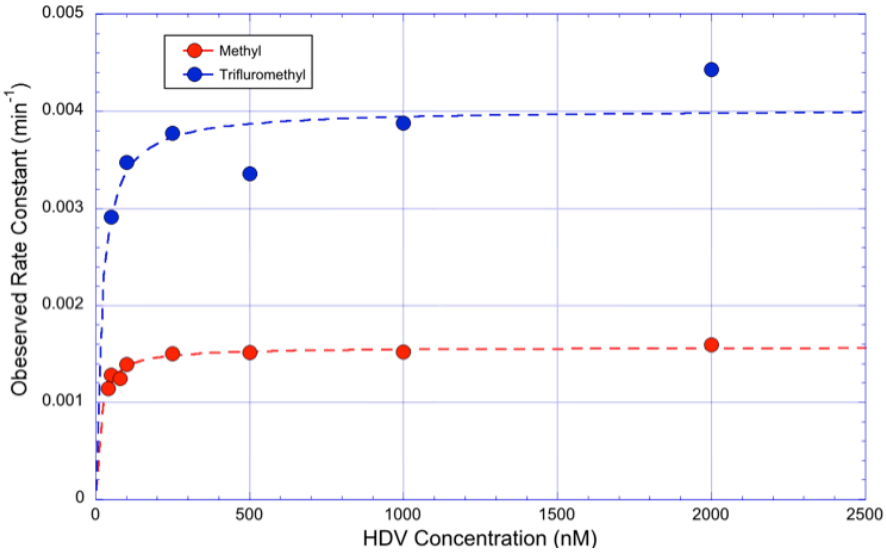

Figure A.5 Ribozyme catalyzed cleavage of propanediol (red) and trifluoromethylpropanediol (blue) substrates at different ribozyme concentrations. The data set an upper limit of ~50 nM for K_m for both substrates. Data fitting reveals apparent K_m's of ribozyme-substrate complex formation of 14 nM and 28 nM for the propanediol and trifluoromethylpropanediol substrates, respectively.

Qualitatively, the tethered substrates reacted from the ES complex with a pH-dependence similar to that of the wild-type substrate, showing a log-linear increase with pH in the acidic limb of the profile that transitions to a pH-independent regime and finally to an inverse dependence at pH values greater than 9.0 (Figure A.6, Table A.3). The log-linear increase with pH reflects a rate-stimulating deprotonation. The identity of the titrating group remains uncertain but has been attributed to deprotonation of a water molecule coordinated to an active site metal ion to generate the catalytic base(Thaplyal et al. 2015). The transition to the pH independent regime reflects the onset of deprotonation of the general acid(Perrotta, Wadkins, and Been 2006). In the log-linear region of pH, the ES complexes for the tethered substrates react about two orders of magnitude slower than the wild type, ribonucleotide substrate, consistent with the importance of the conformational constraint imposed by the ribose ring. (Table A.4).

The tethered substrates react more slowly than the ribose-containing substrates in both the presence and absence of ribozyme. However, the difference in reactivity between the two sets of substrates is reduced in the presence of the ribozyme, presumably due to conformation restriction imposed by the ribozyme active site on the tethered substrates. Comparison between substrate pairs with similar observed solution pK_a's (R: CH_3/wild type and R: CF_3/abasic) allows for evaluation of the energetic contribution from conformational restriction while controlling for differences in nucleophilicity. For each pair of substrates, there is a ~5-fold difference between the ratio of rates in the solution reaction compared to the ribozyme reaction (Table A.4).

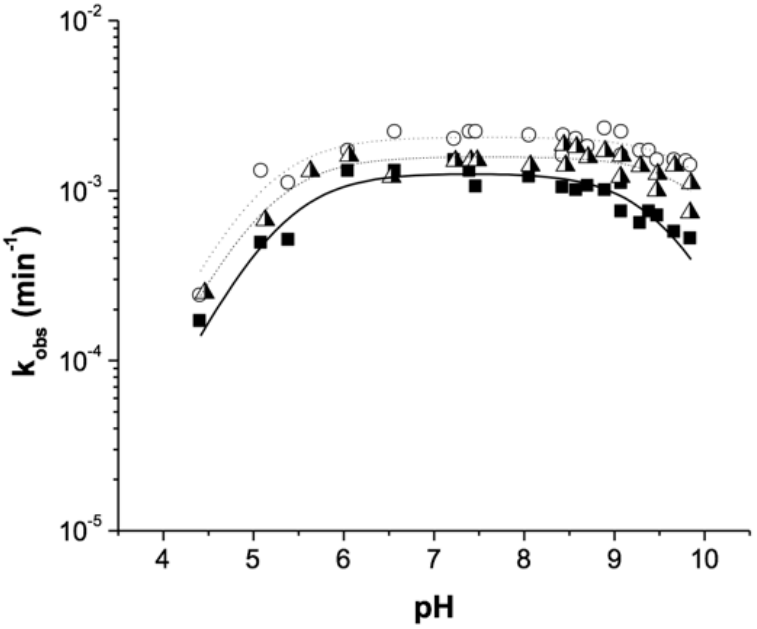

Figure A.6 Ribozyme-catalyzed cleavage of modified substrates that perturb the nucleophile pK_a. pH-rate profile for HDV ribozyme-catalyzed cleavage of RNA substrates. Filled squares and solid line correspond to R = CH_3; half-filled triangles and dashed line correspond to R = CH_2F; open circles and dotted line correspond to R = CF_3. Data were fit to a double ionization model (see methods).

	k_{max} (min^{-1})	pKa_1	pKa_2
R: CH_3	(1.27 ± 0.06) x 10^{-3}	9.5 ± 0.1	5.3 ± 0.1
R: CH_2F	(1.59 ± 0.07) x 10^{-3}	10.1 ± 0.1	5.2 ± 0.2
R: CF_3	(2.07 ± 0.07) x 10^{-3}	10.1 ± 0.1	5.1 ± 0.1

Table A.3 Summary of fits to pH-titration curves for HDV ribozyme-catalyzed cleavage of tethered substrates (Figure A.6).

While it remains possible that a non-chemical step masks the true rate of the ribofuranosyl substrates, a more compelling explanation is that the constrained environment of the ribozyme active site modestly accelerates the tethered substrates by reducing their conformational entropy. This is consistent with the hypothesis that ribozyme docking confers some restriction around the C2′-C3′ bond, but not as much as the ribose ring. Moreover, this result provides a plausible explanation for our prior observation that 2′-β-substituted ribonucleotide substrates were inactive. The same features within the active site that restrict rotation around the C2′-C3′ bond, conferring a rate enhancement on the tethered substrates, might clash sterically with a substituent in the 2′-β-position preventing catalysis.

The reactivity of the methyl-tethered substrate relative to trifluoromethyl-tethered substrate provides insight into the protonation state of the nucleophilic hydroxyl group in the starting ground state of the ES complex. In the non-enzymatic reactions, when the reaction starts from an oxyanionic ground state ($pH > pK_a$), the electron-withdrawing effect of $–CF_3$ manifests in the nucleophilic attack step, resulting in lower maximal rate. However, when the reaction starts from the protonated ground state ($pH < pK_a$), the electron-withdrawing effect on the pK_a increases the fraction of oxyanion present, offsetting the reduced nucleophilicity. In the HDV reaction, the trifluoromethyl substrate reacts moderately faster than the methyl substrate (1.6 fold) and the monofluoromethyl substrate reacts with an intermediate rate. This effect from fluorine substitution more closely resembles the effect observed for non-enzymatic reactions at low pH rather than at high pH, consistent with the ES complex starting from the protonated ground state rather than the deprotonated oxyanion ground state. Moreover, the faster reaction with increasing electron-withdrawing power suggests that the effective charge on the 2′-oxygen increases as the reaction progresses towards the transition state, implying that the extent of O–H

bond cleavage exceeds the extent of O–P bond formation. The pathway to achieve this condition could involve a concerted process, in which deprotonation and nucleophilic attack occur simultaneously, or a stepwise process involving pre-equilibrium deprotonation of the 2′-OH to form the corresponding oxyanion followed by O–P bond formation to an extent that a significant degree of the effective charge on the 2′-oxyanion is lost in the transition state.

	pK_a	Base-Catalyzed[a]	Ribozyme-catalyzed
Ribonucleotide - WT	13.5 ± 0.1[b]	6.9×10^{-2}	1.7×10^{-1}
Ribonucleotide -Abasic	14.5 ± 0.1	2.0×10^{-1}	4.4×10^{-2}
R: CF_3	13.5 ± 0.1	3.7×10^{-4}	1.3×10^{-3}
R: CH_3	14.5 ± 0.2	1.1×10^{-4}	4.9×10^{-4}
Abasic/CH_3[c]		540	90
WT/CF_3[c]		627	133

Table A.4 Comparison of the cleavage rates of the modified DNA/RNA ribonucleotide and tethered substrates in the presence of ribozyme (pH 5) or absence of ribozyme (pH 14). [a]Rates extrapolated from best-fit curve to pH 5. [b]Base-catalyzed reactions measured with N_{-1} = U and ribozyme catalyzed reaction observed with N_{-1} = C. Previous investigation suggests that nucleophile pK_a is insensitive to the identity of the N_{-1} nucleobase31. [c]Ratios of rates given for sterically distinct substrates with similar nucleophile pK_a's.

Comparison between HDV-catalyzed reactions of the abasic and wild type ribonucleotide substrates reinforces the trend observed for the tethered substrates that the substrate bearing the higher pK_a nucleophile reacts more slowly. The abasic substrate reacts ~4-fold slower than the wild type substrate (Table A.4), consistent with prior observations(Shih and Been 2001b). Given that HDV is known to be largely insensitive to the identity of the sequence upstream of its cleavage site, it seems plausible that increase in pK_a upon removal of the electron-withdrawing nucleobase could explain some, if not all, of the difference in reactivity between the abasic and wild-type substrates.

Several alternative explanations could account for the rate stimulation from fluorine substitution observed in the ribozyme reaction: (I) The transition state for the HDV-ribozyme reaction has relatively little bonding between the nucleophilic oxygen and the phosphorous atom, so perturbation of the geminal hydroxyl's nucleophilicity by fluoride substitution has a negligible impact on reactivity. However, the non-enzymatic reaction occurs with a large effective charge change on the nucleophile (Ye et al. 2007). Moreover, the established importance of general acid catalysis in the HDV ribozyme implicates significant bond breaking to the leaving group in the transition state(Das and Piccirilli 2005), which, in the case of phosphodiesters, accompanies significant bond formation to the nucleophile(Gu et al. 2013b). (II) Differential ground state interactions such as solvation of the nucleophile could attenuate the relative reactivity of the methyl-tethered substrate relative to the trifluoromethyl-tethered substrate. Stronger solvation of the former substrate in the ground state could engender a greater energetic penalty for nucleophile desolvation en route to the chemical transition state. It is important to note, however, that the tethered substrates react with nearly identical K_m values in kinetic experiments, suggesting that the substrates bind similarly in the ground state. Lastly, we cannot rule out the possibility that a non-chemical step limits the reaction rates of the tethered substrate and masks the true chemical effect of fluorine substitution. However, the significantly lower reactivity of the tethered substrates compared to the wild-type substrate argues against this possibility.

A.4 Discussion

In an effort to obtain substrates that subtly perturb the basicity of the 2′-hydroxyl nucleophile in the HDV ribozyme reaction, we prepared the phosphoramidite derivatives of 1,2-propanediol, 3-fluoro-1,2-propanediol and 3,3,3-trifluoro-1,2-propanediol and successfully

incorporated them into the 5′-terminus of RNA and DNA oligonucleotides. These oligonucleotides undergo hydroxide and HDV ribozyme-catalyzed transphosphorylation to release the tethers. Comparisons of hydroxide and RNA-catalyzed reactions of these substrates suggest that that (I) the ribozyme´s catalytic apparatus engages without the cleavage site nucleobase or the conformational constraints imposed by the ribofuranose ring, (II) the nucleophilic hydroxyl group predominantly populates the neutral form in the starting ground state for the enzyme-substrate complex, and (III) in the transition state, the 2′ hydroxyl bears some negative charge consistent with a transition state in which extent of proton loss from the 2′-OH exceeds the extent of nucleophilic attack.

The tethered substrates described here provide a simple and accessible context in which to test structure activity relationships for both solution and ribozyme-catalyzed transphosphorylation. Insights gleaned from these substrates could help to interpret additional biochemical data gathered on ribozyme transition states including linear free-energy relationships for general acid-base catalysis and kinetic isotope effects. Specifically, the qualitative information derived here regarding the protonation of the ribozyme substrate ground state, could inform future heavy atom kinetic isotope measurements for the 2´-O nucleophile(Humphry et al. 2008).

References

Anderson, V. E., M. W. Ruszczycky, and M. E. Harris. 2006. "Activation of oxygen nucleophiles in enzyme catalysis." *Chem Rev* 106 (8):3236-51. doi: 10.1021/cr050281z.

Anslyn, Eric V., and Dennis A. Dougherty. 2006. *Modern physical organic chemistry*. Sausalito, Calif.: University Science.

Beattie, T. L., and R. A. Collins. 1997. "Identification of functional domains in the self-cleaving Neurospora VS ribozyme using damage selection." *Journal of Molecular Biology* 267 (4):830-840. doi: DOI 10.1006/jmbi.1997.0921.

Bevilacqua, P. C. 2003. "Mechanistic considerations for general acid-base catalysis by RNA: Revisiting the mechanism of the hairpin ribozyme." *Biochemistry* 42 (8):2259-2265. doi: 10.1021/bi027273m.

Bingaman, J. L., S. X. Zhang, D. R. Stevens, N. H. Yennawar, S. Hammes-Schiffer, and P. C. Bevilacqua. 2017. "The GlcN6P cofactor plays multiple catalytic roles in the glmS ribozyme." *Nature Chemical Biology* 13 (4):439-+.

Bonneau, E., and P. Legault. 2014a. "NMR Localization of Divalent Cations at the Active Site of the Neurospora VS Ribozyme Provides Insights into RNA-Metal-Ion Interactions." *Biochemistry* 53 (3):579-590. doi: 10.1021/bi401484a.

Bonneau, E., and P. Legault. 2014b. "Nuclear Magnetic Resonance Structure of the III-IV-V Three-Way Junction from the Varkud Satellite Ribozyme and Identification of Magnesium-Binding Sites Using Paramagnetic Relaxation Enhancement." *Biochemistry* 53 (39):6264-6275. doi: 10.1021/bi500826n.

Brown, D. M., and D. A. Usher. 1965. "Hydrolysis of Hydroxyalkyl Phosphate Esters - Effect of Changing Ester Group." *Journal of the Chemical Society* (Nov):6558-&.

Campbell, D. O., P. Bouchard, G. Desjardins, and P. Legault. 2006. "NMR structure of Varkud satellite ribozyme stem-loop V in the presence of magnesium ions and localization of metal-binding sites." *Biochemistry* 45 (35):10591-10605. doi: 10.1021/bi0607150.

Campbell, D. O., and P. Legault. 2005. "Nuclear magnetic resonance structure of the varkud satellite ribozyme stem-loop V RNA and magnesium-ion binding from chemical-shift mapping." *Biochemistry* 44 (11):4157-4170. doi: DOI 10.1021/bi047963l.

Cerrone-Szakal, A. L., D. M. Chadalavada, B. L. Golden, and P. C. Bevilacqua. 2008. "Mechanistic characterization of the HDV genomic ribozyme: the cleavage site base pair

plays a structural role in facilitating catalysis." *RNA* 14 (9):1746-60. doi: 10.1261/rna.1140308.

Cerrone-Szakal, A. L., N. A. Siegfried, and P. C. Bevilacqua. 2008. "Mechanistic characterization of the HDV genomic ribozyme: solvent isotope effects and proton inventories in the absence of divalent metal ions support C75 as the general acid." *J Am Chem Soc* 130 (44):14504-20. doi: 10.1021/ja801816k.

Chen, J., A. Ganguly, Z. Miswan, S. Hammes-Schiffer, P. C. Bevilacqua, and B. L. Golden. 2013. "Identification of the catalytic Mg(2)(+) ion in the hepatitis delta virus ribozyme." *Biochemistry* 52 (3):557-67. doi: 10.1021/bi3013092.

Chen, J. H., B. Gong, P. C. Bevilacqua, P. R. Carey, and B. L. Golden. 2009. "A catalytic metal ion interacts with the cleavage Site G.U wobble in the HDV ribozyme." *Biochemistry* 48 (7):1498-507. doi: 10.1021/bi8020108.

Chen, J. H., R. Yajima, D. M. Chadalavada, E. Chase, P. C. Bevilacqua, and B. L. Golden. 2010. "A 1.9 A crystal structure of the HDV ribozyme precleavage suggests both Lewis acid and general acid mechanisms contribute to phosphodiester cleavage." *Biochemistry* 49 (31):6508-18. doi: 10.1021/bi100670p.

Cleland, W. W., and A. C. Hengge. 1995. "Mechanisms of phosphoryl and acyl transfer." *FASEB J* 9 (15):1585-94.

Cleland, W. W., and A. C. Hengge. 2006. "Enzymatic mechanisms of phosphate and sulfate transfer." *Chem Rev* 106 (8):3252-78. doi: 10.1021/cr050287o.

Cochrane, J. C., S. V. Lipchock, K. D. Smith, and S. A. Strobel. 2009. "Structural and chemical basis for glucosamine 6-phosphate binding and activation of the glmS ribozyme." *Biochemistry* 48 (15):3239-46. doi: 10.1021/bi802069p.

Cochrane, J. C., and S. A. Strobel. 2008. "Catalytic strategies of self-cleaving ribozymes." *Accounts of Chemical Research* 41 (8):1027-1035. doi: 10.1021/ar800050c.

Collins, R. A., D. M. DeAbreu, and T. L. Beattie. 1997. "Tertiary folding of the neurospora VS ribozyme." *Faseb Journal* 11 (9):A1285-A1285.

Dagenais, P., N. Girard, E. Bonneau, and P. Legault. 2017. "Insights into RNA structure and dynamics from recent NMR and X-ray studies of the Neurospora Varkud satellite ribozyme." *Wiley Interdisciplinary Reviews-Rna* 8 (5). doi: ARTN e1421

10.1002/wrna.1421.

Dai, Q., J. K. Frederiksen, V. E. Anderson, M. E. Harris, and J. A. Piccirilli. 2008. "Efficient synthesis of [2 '-O-18]uridine and its incorporation into oligonucleotides: A new tool for mechanistic study of nucleotidyl transfer reactions by isotope effect analysis." *Journal of Organic Chemistry* 73 (1):309-311. doi: 10.1021/jo701727h.

Dai, Q., and J. A. Piccirilli. 2003. "Synthesis of 2 '-C-beta-fluoromethyluridine." *Organic Letters* 5 (6):807-810.

Das, S. R., and J. A. Piccirilli. 2005. "General acid catalysis by the hepatitis delta virus ribozyme." *Nat Chem Biol* 1 (1):45-52. doi: 10.1038/nchembio703.

DasGupta, S., N. B. Suslov, and J. A. Piccirilli. 2017. "Structural Basis for Substrate Helix Remodeling and Cleavage Loop Activation in the Varkud Satellite Ribozyme." *Journal of the American Chemical Society* 139 (28):9591-9597. doi: 10.1021/jacs.7b03655.

Eiler, D., J. Wang, and T. A. Steitz. 2014. "Structural basis for the fast self-cleavage reaction catalyzed by the twister ribozyme." *Proc Natl Acad Sci U S A* 111 (36):13028-33. doi: 10.1073/pnas.1414571111.

Ganguly, A., P. Thaplyal, E. Rosta, P. C. Bevilacqua, and S. Hammes-Schiffer. 2014. "Quantum mechanical/molecular mechanical free energy simulations of the self-cleavage reaction in the hepatitis delta virus ribozyme." *J Am Chem Soc* 136 (4):1483-96. doi: 10.1021/ja4104217.

Georgiadis, M. M., I. Singh, W. F. Kellett, S. Hoshika, S. A. Benner, and N. G. Richards. 2015. "Structural basis for a six nucleotide genetic alphabet." *J Am Chem Soc* 137 (21):6947-55. doi: 10.1021/jacs.5b03482.

Gong, B., J. H. Chen, E. Chase, D. M. Chadalavada, R. Yajima, B. L. Golden, P. C. Bevilacqua, and P. R. Carey. 2007. "Direct measurement of a pK(a) near neutrality for the catalytic cytosine in the genomic HDV ribozyme using Raman crystallography." *J Am Chem Soc* 129 (43):13335-42. doi: 10.1021/ja0743893.

Gu, H., S. M. Zhang, K. Y. Wong, B. K. Radak, T. Dissanayake, D. L. Kellerman, Q. Dai, M. Miyagi, V. E. Anderson, D. M. York, J. A. Piccirilli, and M. E. Harris. 2013a. "Experimental and computational analysis of the transition state for ribonuclease A-catalyzed RNA 2 '-O-transphosphorylation." *Proceedings of the National Academy of Sciences of the United States of America* 110 (32):13002-13007. doi: 10.1073/pnas.1215086110.

Gu, H., S. Zhang, K. Y. Wong, B. K. Radak, T. Dissanayake, D. L. Kellerman, Q. Dai, M. Miyagi, V. E. Anderson, D. M. York, J. A. Piccirilli, and M. E. Harris. 2013b. "Experimental and computational analysis of the transition state for ribonuclease A-

catalyzed RNA 2'-O-transphosphorylation." *Proc Natl Acad Sci U S A* 110 (32):13002-7. doi: 10.1073/pnas.1215086110.

Harris, M. E., Q. Dai, H. Gu, D. L. Kellerman, J. A. Piccirilli, and V. E. Anderson. 2010. "Kinetic Isotope Effects for RNA Cleavage by 2 '-O-Transphosphorylation: Nucleophilic Activation by Specific Base." *Journal of the American Chemical Society* 132 (33):11613-11621. doi: 10.1021/ja103550e.

Harris, M. E., D. M. York, J. A. Piccirilli, and V. E. Anderson. 2017. "Kinetic Isotope Effect Analysis of RNA 2'-O-Transphosphorylation." *Methods Enzymol* 596:433-457. doi: 10.1016/bs.mie.2017.07.017.

Hengge, A. C. 2002. "Isotope effects in the study of phosphoryl and sulfuryl transfer reactions." *Accounts of Chemical Research* 35 (2):105-112. doi: 10.1021/ar000143q.

Hiller, D. A., V. Singh, M. H. Zhong, and S. A. Strobel. 2011. "A two-step chemical mechanism for ribosome-catalysed peptide bond formation." *Nature* 476 (7359):236-U143. doi: 10.1038/nature10248.

Hiller, D. A., M. Zhong, V. Singh, and S. A. Strobel. 2010. "Transition states of uncatalyzed hydrolysis and aminolysis reactions of a ribosomal P-site substrate determined by kinetic isotope effects." *Biochemistry* 49 (18):3868-78. doi: 10.1021/bi901458x.

Humphry, T., S. Iyer, O. Iranzo, J. R. Morrow, J. P. Richard, P. Paneth, and A. C. Hengge. 2008. "Altered Transition State for the Reaction of an RNA Model Catalyzed by a Dinuclear Zinc(II) Catalyst." *Journal of the American Chemical Society* 130 (52):17858-17866. doi: 10.1021/ja8059864.

Jaikaran, D., M. D. Smith, R. Mehdizadeh, J. Olive, and R. A. Collins. 2008. "An important role of G638 in the cis-cleavage reaction of the Neurospora VS ribozyme revealed by a novel nucleotide analog incorporation method." *Rna-a Publication of the Rna Society* 14 (5):938-949. doi: 10.1261/rna.936508.

Jimenez, R. M., J. A. Polanco, and A. Luptak. 2015. "Chemistry and Biology of Self-Cleaving Ribozymes." *Trends in Biochemical Sciences* 40 (11):648-661. doi: 10.1016/j.tibs.2015.09.001.

Jones, F. D., S. P. Ryder, and S. A. Strobel. 2001. "An efficient ligation reaction promoted by a Varkud Satellite ribozyme with extended 5 ' and 3 '-termini." *Nucleic Acids Research* 29 (24):5115-5120. doi: DOI 10.1093/nar/29.24.5115.

Kapral, G. J., S. Jain, J. Noeske, J. A. Doudna, D. C. Richardson, and J. S. Richardson. 2014. "New tools provide a second look at HDV ribozyme structure, dynamics and cleavage." *Nucleic Acids Res* 42 (20):12833-46. doi: 10.1093/nar/gku992.

Kath-Schorr, S., T. J. Wilson, N. S. Li, J. Lu, J. A. Piccirilli, and D. M. Lilley. 2012. "General acid-base catalysis mediated by nucleobases in the hairpin ribozyme." *J Am Chem Soc* 134 (40):16717-24. doi: 10.1021/ja3067429.

Ke, A., K. Zhou, F. Ding, J. H. Cate, and J. A. Doudna. 2004. "A conformational switch controls hepatitis delta virus ribozyme catalysis." *Nature* 429 (6988):201-5. doi: 10.1038/nature02522.

Kellerman, D. L., K. S. Simmons, M. Pedraza, J. A. Piccirilli, D. M. York, and M. E. Harris. 2015. "Determination of hepatitis delta virus ribozyme N(-1) nucleobase and functional group specificity using internal competition kinetics." *Analytical Biochemistry* 483:12-20.

Kennell, J. C., B. J. Saville, S. Mohr, M. T. R. Kuiper, J. R. Sabourin, R. A. Collins, and A. M. Lambowitz. 1995. "The Vs Catalytic Rna Replicates by Reverse Transcription as a Satellite of a Retroplasmid." *Genes & Development* 9 (3):294-303. doi: DOI 10.1101/gad.9.3.294.

Kim, S. H., D. G. Bartholomew, L. B. Allen, R. K. Robins, and G. R. Revankar. 1978. "Imidazo[1,2-a]-s-triazine nucleosides. Synthesis and antiviral activity of the N-bridgehead guanine, guanosine, and guanosine monophosphate analogues of imidazo[1,2-a]-s-triazine." *J Med Chem* 21 (9):883-9.

Knowles, J. R. 1980. "Enzyme-catalyzed phosphoryl transfer reactions." *Annu Rev Biochem* 49:877-919. doi: 10.1146/annurev.bi.49.070180.004305.

Kohen, Amnon, and Hans-Heinrich Limbach. 2006. *Isotope effects in chemistry and biology*. Boca Raton: Taylor & Francis.

Koo, S. C., J. Lu, N. S. Li, E. Leung, S. R. Das, M. E. Harris, and J. A. Piccirilli. 2015. "Transition State Features in the Hepatitis Delta Virus Ribozyme Reaction Revealed by Atomic Perturbations." *J Am Chem Soc* 137 (28):8973-82. doi: 10.1021/jacs.5b01189.

Kovacheva, Y. S., S. B. Tzokov, I. A. Murray, and J. A. Grasby. 2004. "The role of phosphate groups in the VS ribozyme-substrate interaction." *Nucleic Acids Research* 32 (21):6240-6250. doi: 10.1093/nar/gkh957.

Krauch, T., U. Vonkrosigk, L. J. Macpherson, S. E. Moroney, J. A. Piccirilli, J. B. Sweeney, C. Y. Switzer, and S. A. Benner. 1988. "New Base-Pairs for DNA and Rna." *Abstracts of Papers of the American Chemical Society* 196:234-Orgn.

Krishnamurthy, R. 2012. "Role of pK(a) of Nucleobases in the Origins of Chemical Evolution." *Accounts of Chemical Research* 45 (12):2035-2044. doi: 10.1021/ar200262x.

Lafontaine, D. A., T. J. Wilson, D. G. Norman, and D. M. J. Lilley. 2001. "The A730 loop is an important component of the active site of the VS ribozyme." *Journal of Molecular Biology* 312 (4):663-674. doi: DOI 10.1006/jmbi.2001.4996.

Lafontaine, D. A., T. J. Wilson, Z. Y. Zhao, and D. M. J. Lilley. 2002. "Functional group requirements in the probable active site of the VS ribozyme." *Journal of Molecular Biology* 323 (1):23-34. doi: 10.1016/S0022-2836(02)00910-5.

Lassila, J. K., J. G. Zalatan, and D. Herschlag. 2011. "Biological Phosphoryl-Transfer Reactions: Understanding Mechanism and Catalysis." *Annual Review of Biochemistry, Vol 80* 80:669-702. doi: 10.1146/annurev-biochem-060409-092741.

Li, Y. F., and R. R. Breaker. 1999. "Kinetics of RNA degradation by specific base catalysis of transesterification involving the 2 '-hydroxyl group." *Journal of the American Chemical Society* 121 (23):5364-5372. doi: DOI 10.1021/ja990592p.

Lilley, D. M. J. 2004. "The Varkud satellite ribozyme." *Rna-a Publication of the Rna Society* 10 (2):151-158. doi: 10.1261/rna.5217104.

Liu, Y., T. J. Wilson, S. A. McPhee, and D. M. Lilley. 2014. "Crystal structure and mechanistic investigation of the twister ribozyme." *Nat Chem Biol* 10 (9):739-44. doi: 10.1038/nchembio.1587.

Lu, J., S. C. Koo, B. P. Weissman, M. E. Harris, N. S. Li, and J. A. Piccirilli. 2018. "Evidence That Nucleophile Deprotonation Exceeds Bond Formation in the HDV Ribozyme Transition State." *Biochemistry* 57 (25):3465-3472. doi: 10.1021/acs.biochem.8b00031.

Maguire, J. L., and R. A. Collins. 2001. "Effects of cobalt hexammine on folding and self-cleavage of the Neurospora VS ribozyme." *Journal of Molecular Biology* 309 (1):45-56. doi: DOI 10.1006/jmbi.2001.4625.

Melander, Lars C. S., and William Hundley Saunders. 1987. *Reaction rates of isotopic molecules*. Malabar, Fla.: R.E. Krieger Pub. Co.

Mikkola, S., E. Stenman, K. Nurmi, E. Yousefi-Salakdeh, R. Stromberg, and H. Lonnberg. 1999. "The mechanism of the metal ion promoted cleavage of RNA phosphodiester bonds

involves a general acid catalysis by the metal aquo ion on the departure of the leaving group." *Journal of the Chemical Society-Perkin Transactions 2* (8):1619-1625.

Mock, W. L., and J. Z. Zhang. 1990. "Concerning the Relative Acidities of Simple Alcohols." *Tetrahedron Letters* 31 (40):5687-5688.

Murray, J. B., A. A. Seyhan, N. G. Walter, J. M. Burke, and W. G. Scott. 1998. "The hammerhead, hairpin and VS ribozymes are catalytically proficient in monovalent cations alone." *Chemistry & Biology* 5 (10):587-595. doi: Doi 10.1016/S1074-5521(98)90116-8.

Nakano, S., and P. C. Bevilacqua. 2001. "Proton inventory of the genomic HDV ribozyme in Mg2+-containing solutions." *Journal of the American Chemical Society* 123 (45):11333-11334. doi: DOI 10.1021/ja0166850.

Nakano, S., D. M. Chadalavada, and P. C. Bevilacqua. 2000. "General acid-base catalysis in the mechanism of a hepatitis delta virus ribozyme." *Science* 287 (5457):1493-7.

Nam, K., Q. Cui, J. Gao, and D. M. York. 2007. "Specific Reaction Parametrization of the AM1/d Hamiltonian for Phosphoryl Transfer Reactions: H, O, and P Atoms." *J Chem Theory Comput* 3 (2):486-504. doi: 10.1021/ct6002466.

Neuner, S., C. Falschlunger, E. Fuchs, M. Himmelstoss, A. M. Ren, D. J. Patel, and R. Micura. 2017. "Atom-Specific Mutagenesis Reveals Structural and Catalytic Roles for an Active-Site Adenosine and Hydrated Mg2+ in Pistol Ribozymes." *Angewandte Chemie-International Edition* 56 (50):15954-15958. doi: 10.1002/anie.201708679.

Oivanen, M., S. Kuusela, and H. Lonnberg. 1998. "Kinetics and Mechanisms for the Cleavage and Isomerization of the Phosphodiester Bonds of RNA by Bronsted Acids and Bases." *Chem Rev* 98 (3):961-990.

Ouellet, J., M. Byrne, and D. M. J. Lilley. 2009. "Formation of an active site in trans by interaction of two complete Varkud Satellite ribozymes." *Rna-a Publication of the Rna Society* 15 (10):1822-1826. doi: 10.1261/rna.1759009.

Pecoraro, V. L., J. D. Hermes, and W. W. Cleland. 1984. "Stability-Constants of Mg-2+ and Cd-2+ Complexes of Adenine-Nucleotides and Thionucleotides and Rate Constants for Formation and Dissociation of Mgatp and Mgadp." *Biochemistry* 23 (22):5262-5271. doi: DOI 10.1021/bi00317a026.

Perrotta, A. T., and M. D. Been. 1990. "The Self-Cleaving Domain from the Genomic Rna of Hepatitis Delta-Virus - Sequence Requirements and the Effects of Denaturant." *Nucleic Acids Research* 18 (23):6821-6827.

Perrotta, A. T., and M. D. Been. 2006. "HDV ribozyme activity in monovalent cations." *Biochemistry* 45 (38):11357-11365. doi: 10.1021/bi061215+.

Perrotta, A. T., T. S. Wadkins, and M. D. Been. 2006. "Chemical rescue, multiple ionizable groups, and general acid-base catalysis in the HDV genomic ribozyme." *RNA* 12 (7):1282-91. doi: 10.1261/rna.14106.

Prody, G. A., J. T. Bakos, J. M. Buzayan, I. R. Schneider, and G. Bruening. 1986. "Autolytic processing of dimeric plant virus satellite RNA." *Science* 231 (4745):1577-80. doi: 10.1126/science.231.4745.1577.

Rastogi, T., T. L. Beattie, J. E. Olive, and R. A. Collins. 1996. "A long-range pseudoknot is required for activity of the Neurospora VS ribozyme." *Embo Journal* 15 (11):2820-2825.

Ren, A. M., N. Vusurovic, J. Gebetsberger, P. Gao, M. Juen, C. Kreutz, R. Micura, and D. J. Patel. 2016. "Pistol ribozyme adopts a pseudoknot fold facilitating site-specific in-line cleavage." *Nature Chemical Biology* 12 (9):702-+. doi: 10.1038/nchembio.2125.

Riccitelli, N., and A. Luptak. 2013. "HDV family of self-cleaving ribozymes." *Prog Mol Biol Transl Sci* 120:123-71. doi: 10.1016/B978-0-12-381286-5.00004-4.

Rosta, E., M. Nowotny, W. Yang, and G. Hummer. 2011. "Catalytic mechanism of RNA backbone cleavage by ribonuclease H from quantum mechanics/molecular mechanics simulations." *J Am Chem Soc* 133 (23):8934-41. doi: 10.1021/ja200173a.

Roth, A., Z. Weinberg, A. G. Y. Chen, P. B. Kim, T. D. Ames, and R. R. Breaker. 2014. "A widespread self-cleaving ribozyme class is revealed by bioinformatics." *Nature Chemical Biology* 10 (1):56-U92. doi: 10.1038/Nchembio.1386.

Saville, B. J., and R. A. Collins. 1990. "A Site-Specific Self-Cleavage Reaction Performed by a Novel Rna in Neurospora Mitochondria." *Cell* 61 (4):685-696. doi: Doi 10.1016/0092-8674(90)90480-3.

Schramm, V. L. 2003. "Enzymatic transition state poise and transition state analogues." *Acc Chem Res* 36 (8):588-96. doi: 10.1021/ar0200495.

Schramm, V. L. 2011. "Enzymatic transition states, transition-state analogs, dynamics, thermodynamics, and lifetimes." *Annu Rev Biochem* 80:703-32. doi: 10.1146/annurev-biochem-061809-100742.

Seith, D. D., J. L. Bingaman, A. J. Veenis, A. C. Button, and P. C. Bevilacqua. 2018. "Elucidation of Catalytic Strategies of Small Nucleolytic Ribozymes from Comparative Analysis of Active Sites." *Acs Catalysis* 8 (1):314-327. doi: 10.1021/acscatal.7b02976.

Sharmeen, L., M. Y. Kuo, G. Dinter-Gottlieb, and J. Taylor. 1988. "Antigenomic RNA of human hepatitis delta virus can undergo self-cleavage." *J Virol* 62 (8):2674-9.

Shih, I., and M. D. Been. 2000. "Kinetic scheme for intermolecular RNA cleavage by a ribozyme derived from hepatitis delta virus RNA." *Biochemistry* 39 (31):9055-66.

Shih, I., and M. D. Been. 2001a. "Involvement of a cytosine side chain in proton transfer in the rate-determining step of ribozyme self-cleavage." *Proceedings of the National Academy of Sciences of the United States of America* 98 (4):1489-1494. doi: DOI 10.1073/pnas.98.4.1489.

Shih, I. H., and M. D. Been. 2002. "Catalytic strategies of the hepatitis delta virus ribozymes." *Annual Review of Biochemistry* 71:887-917. doi: 10.1146/annurev.biochem.71.110601.135349.

Shih, Ih, and M. D. Been. 2001b. "Energetic contribution of non-essential 5' sequence to catalysis in a hepatitis delta virus ribozyme." *EMBO J* 20 (17):4884-91. doi: 10.1093/emboj/20.17.4884.

Smith, M. D., and R. A. Collins. 2007. "Evidence for proton transfer in the rate-limiting step of a fast-cleaving Varkud satellite ribozyme." *Proceedings of the National Academy of Sciences of the United States of America* 104 (14):5818-5823. doi: 10.1073/pnas.0608864104.

Sood, V. D., T. L. Beattie, and R. A. Collins. 1998. "Identification of phosphate groups involved in metal binding and tertiary interactions in the core of the Neurospora VS ribozyme." *Journal of Molecular Biology* 282 (4):741-750. doi: DOI 10.1006/jmbi.1998.2049.

Sowa, G. A., A. C. Hengge, and W. W. Cleland. 1997. "O-18 isotope effects support a concerted mechanism for ribonuclease A." *Journal of the American Chemical Society* 119 (9):2319-2320. doi: DOI 10.1021/ja963974t.

Suslov, N. B., S. DasGupta, H. Huang, J. R. Fuller, D. M. J. Lilley, P. A. Rice, and J. A. Piccirilli. 2015. "Crystal structure of the Varkud satellite ribozyme." *Nature Chemical Biology* 11 (11):840-U51. doi: 10.1038/nchembio.1929.

Thaplyal, P., A. Ganguly, B. L. Golden, S. Hammes-Schiffer, and P. C. Bevilacqua. 2013. "Thio effects and an unconventional metal ion rescue in the genomic hepatitis delta virus ribozyme." *Biochemistry* 52 (37):6499-514. doi: 10.1021/bi4000673.

Thaplyal, P., A. Ganguly, S. Hammes-Schiffer, and P. C. Bevilacqua. 2015. "Inverse thio effects in the hepatitis delta virus ribozyme reveal that the reaction pathway is controlled by

metal ion charge density." *Biochemistry* 54 (12):2160-75. doi: 10.1021/acs.biochem.5b00190.

Thomas, J. M., and D. M. Perrin. 2008. "Probing General Base Catalysis in the Hammerhead Ribozyme." *Journal of the American Chemical Society* 130 (46):15467-15475. doi: 10.1021/ja804496z.

Thomas, J. M., and D. M. Perrin. 2009. "Probing General Acid Catalysis in the Hammerhead Ribozyme." *Journal of the American Chemical Society* 131 (3):1135-1143. doi: 10.1021/ja807790e.

Tzokov, S. B., I. A. Murray, and J. A. Grasby. 2002. "The role of magnesium ions and 2 '-hydroxyl groups in the VS ribozyme-substrate interaction." *Journal of Molecular Biology* 324 (2):215-226. doi: 10.1016/S0022-2836(02)01063-X.

Unrau, P. J., and D. P. Bartel. 2003. "An oxocarbenium-ion intermediate of a ribozyme reaction indicated by kinetic isotope effects." *Proceedings of the National Academy of Sciences of the United States of America* 100 (26):15393-15397. doi: 10.1073/pnas.2433147100.

Van Holde, K. E., W. Curtis Johnson, and Pui Shing Ho. 2006. *Principles of physical biochemistry*. 2nd ed. Upper Saddle River, N.J.: Pearson/Prentice Hall.

Viladoms, J., and M. J. Fedor. 2012. "The glmS Ribozyme Cofactor is a General Acid-Base Catalyst." *Journal of the American Chemical Society* 134 (46):19043-19049. doi: 10.1021/ja307021f.

Weinberg, Z., P. B. Kim, T. H. Chen, S. S. Li, K. A. Harris, C. E. Lunse, and R. R. Breaker. 2015. "New classes of self-cleaving ribozymes revealed by comparative genomics analysis." *Nature Chemical Biology* 11 (8):606-U111. doi: 10.1038/Nchembio.1846.

Weissman, B. P., N. S. Li, D. York, M. Harris, and J. A. Piccirilli. 2015. "Heavy atom labeled nucleotides for measurement of kinetic isotope effects." *Biochim Biophys Acta* 1854 (11):1737-45. doi: 10.1016/j.bbapap.2015.03.007.

Westaway, K. C., Y. R. Fang, J. Persson, and O. Matsson. 1998. "Using C-11/C-14 incoming group and secondary alpha-deuterium KIEs to determine how a change in leaving group alters the structure of the transition state of the S(N)2 reactions between m-chlorobenzyl para-substituted benzenesulfonates and cyanide ion." *Journal of the American Chemical Society* 120 (14):3340-3344. doi: DOI 10.1021/ja972981u.

Westheimer, F. H. 1987. "Why nature chose phosphates." *Science* 235 (4793):1173-8.

Wilson, T. J., N. S. Li, J. Lu, J. K. Frederiksen, J. A. Piccirilli, and D. M. J. Lilley. 2010. "Nucleobase-mediated general acid-base catalysis in the Varkud satellite ribozyme." *Proceedings of the National Academy of Sciences of the United States of America* 107 (26):11751-11756. doi: 10.1073/pnas.1004255107.

Wilson, T. J., Y. Liu, C. Domnick, S. Kath-Schorr, and D. M. Lilley. 2016. "The Novel Chemical Mechanism of the Twister Ribozyme." *J Am Chem Soc* 138 (19):6151-62. doi: 10.1021/jacs.5b11791.

Wilson, T. J., A. C. McLeod, and D. M. J. Lilley. 2007. "A guanine nucleobase important for catalysis by the VS ribozyme." *Embo Journal* 26 (10):2489-2500. doi: 10.1038/sj.emboj.7601698.

Wincott, F., A. Direnzo, C. Shaffer, S. Grimm, D. Tracz, C. Workman, D. Sweedler, C. Gonzalez, S. Scaringe, and N. Usman. 1995. "Synthesis, Deprotection, Analysis and Purification of Rna and Ribozymes." *Nucleic Acids Research* 23 (14):2677-2684.

Winkler, W. C., A. Nahvi, A. Roth, J. A. Collins, and R. R. Breaker. 2004. "Control of gene expression by a natural metabolite-responsive ribozyme." *Nature* 428 (6980):281-6. doi: 10.1038/nature02362.

Ye, J. D., N. S. Li, Q. Dai, and J. A. Piccirilli. 2007. "The mechanism of RNA strand scission: an experimental measure of the Bronsted coefficient, beta nuc." *Angew Chem Int Ed Engl* 46 (20):3714-7. doi: 10.1002/anie.200605124.

Zamel, R., and R. A. Collins. 2002. "Rearrangement of substrate secondary structure facilitates binding to the Neurospora VS ribozyme." *Journal of Molecular Biology* 324 (5):903-915. doi: 10.1016/S0022-2836(02)01151-8.

Zamel, R., A. Poon, D. Jaikaran, A. Andersen, J. Olive, D. De Abreu, and R. A. Collins. 2004. "Exceptionally fast self-cleavage by a Neurospora Varkud satellite ribozyme." *Proceedings of the National Academy of Sciences of the United States of America* 101 (6):1467-1472. doi: 10.1073/pnas.0305753101.